Grand unified neutrino spectrum at Earth: Sources and spectral components

Edoardo Vitagliano

Max-Planck-Institut für Physik (Werner-Heisenberg-Institut), Föhringer Ring 6, 80805 München, Germany and Department of Physics and Astronomy, University of California, Los Angeles, California 90095-1547, USA

Irene Tamborra

Niels Bohr International Academy and DARK, Niels Bohr Institute, Blegdamsvej 17, 2100 Copenhagen, Denmark

Georg Raffelt

Max-Planck-Institut für Physik (Werner-Heisenberg-Institut), Föhringer Ring 6, 80805 München, Germany

(published 9 December 2020)

The dominant neutrino fluxes at Earth from different sources are reviewed and the *grand unified neutrino spectrum* ranging from meV to PeV energies is presented. For each energy band and source, both theoretical expectations and experimental data are discussed. This compact review serves as a reference to those interested in neutrino astronomy, fundamental particle physics, dark-matter detection, high-energy astrophysics, geophysics, and other related topics.

DOI: 10.1103/RevModPhys.92.045006

CONTENTS

I. Introduction 2
II. Cosmic Neutrino Background 4
A. Standard properties of the CNB 4
B. Neutrinos as hot dark matter 5
C. Spectrum at Earth 5
D. Detection perspectives 6
III. Neutrinos from Big-Bang Nucleosynthesis 7
A. Primordial nucleosynthesis 7
B. Neutrinos from decaying light isotopes 7
C. Neutrinos with mass 8
IV. Solar Neutrinos from Nuclear Reactions 9
A. The Sun as a neutrino source 10
B. Production processes and spectra 10
C. Standard solar models 12
D. Antineutrinos 13
E. Flavor conversion 14
F. Observations and detection perspectives 14
V. Thermal Neutrinos from the Sun 15
A. Emission processes 15
B. Solar flux at Earth 16
C. Extremely low energies 17
VI. Geoneutrinos 17
A. Production mechanisms 17
B. Earth modeling 18
C. Detection opportunities 19
VII. Reactor Neutrinos 20
A. Production and detection of reactor neutrinos 20
B. Measurements 22
VIII. Supernova Neutrinos 23
A. Generic features of supernova neutrinos 23
B. Reference neutrino signal 23
C. Electron-capture supernovae 25
D. Failed explosions 25
E. Broken spherical symmetry in the stellar explosion 26
F. Flavor conversion 26
G. Detection perspectives 26
IX. Diffuse Supernova Neutrinos 26
A. Basic estimate 26
B. Redshift integral 27
C. Cosmic core-collapse rate 27
D. Average emission spectrum 29
E. Flavor Conversion 31
F. Detection perspectives 31
X. Atmospheric Neutrinos 32
A. Cosmic rays 32
B. Conventional neutrinos 32
C. Prompt neutrinos 33
D. Predictions and observations 34
E. Experimental facilities 34
F. Solar atmospheric neutrinos 35
XI. Extraterrestrial High-Energy Neutrinos 35
A. Production mechanisms and detection prospects 35
B. Multimessenger connections 36
C. Star-forming galaxies 37
D. Gamma-ray bursts 38
E. Blazars 38
F. Cosmogenic neutrinos 39
G. Future detection prospects 40
XII. Discussion and Outlook 40
Acknowledgments 41
Appendix A: Units and Dimensions 41
Appendix B: Neutrino Mass Matrix 42

Appendix C: Neutrino Mixing in Matter 43
Appendix D: Constructing the GUNS Plot 45
References 46

I. INTRODUCTION

In our epoch of multimessenger astronomy, the Universe is no longer explored with electromagnetic radiation alone, but in addition to cosmic rays, neutrinos and gravitational waves are becoming crucial astrophysical probes. While the age of gravitational-wave detection has only begun (Abbott *et al.*, 2016), neutrino astronomy has evolved from modest beginnings in the late 1960s with the first detections of atmospheric (Achar *et al.*, 1965; Reines *et al.*, 1965) and solar neutrinos (Davis, Harmer, and Hoffman, 1968) to a mainstream effort. Today, a vast array of experiments observe the neutrino sky over a large range of energies (Koshiba, 1992; Cribier, Spiro, and Vignaud, 1995; Becker, 2008; Spiering, 2012; Gaisser and Karle, 2017).

When observing distant sources, inevitably one also probes the intervening space and the propagation properties of the radiation, providing tests of fundamental physics. Examples include time-of-flight limits on the masses of photons (Goldhaber and Nieto, 2010; Tanabashi *et al.*, 2018; Wei and Wu, 2018), gravitons (Goldhaber and Nieto, 2010; de Rham *et al.*, 2017) and neutrinos (Loredo and Lamb, 1989, 2002; Beacom, Boyd, and Mezzacappa, 2000; Nardi and Zuluaga, 2004; Ellis *et al.*, 2012; Lu *et al.*, 2015; Tanabashi *et al.*, 2018), photon or graviton mixing with axionlike particles (Raffelt and Stodolsky, 1988; Meyer, Horns, and Raue, 2013; Meyer *et al.*, 2017; Conlon *et al.*, 2018; Galanti and Roncadelli, 2018; Liang *et al.*, 2019), the relative propagation speed of different types of radiation (Longo, 1987; Stodolsky, 1988; Ellis *et al.*, 2019; Laha, 2019), tests of Lorentz invariance violation (Liberati and Maccione, 2009; Liberati, 2013; Guedes Lang, Martínez-Huerta, and de Souza, 2018; Tanabashi *et al.*, 2018; Ellis *et al.*, 2019; Laha, 2019), or the Shapiro time delay in gravitational potentials (Krauss and Tremaine, 1988; Longo, 1988; Pakvasa, Simmons, and Weiler, 1989; Wang, Liu, and Wang, 2016; Wei *et al.*, 2017; Desai and Kahya, 2018; Shoemaker and Murase, 2018; Boran, Desai, and Kahya, 2019).

Neutrinos are special in this regard because questions about their internal properties were on the table immediately after the first observation of solar neutrinos. The daring interpretation of the observed deficit in terms of flavor oscillations (Gribov and Pontecorvo, 1969), supported by atmospheric neutrino measurements (Fukuda *et al.*, 1998), eventually proved correct (Aharmim *et al.*, 2010; Esteban *et al.*, 2017; Capozzi *et al.*, 2018; de Salas *et al.*, 2018). Today this effect is a standard ingredient to interpret neutrino measurements from practically any source. While some parameters of the neutrino mixing matrix remain to be settled (the mass ordering and the *CP*-violating phase), it is probably fair to say that in neutrino astronomy today the focus is more on the sources and less on properties of the radiation. However, there is always room for surprises and new discoveries.

One major exception to this development is the cosmic neutrino background (CNB), which has never been directly detected and where the question of the absolute neutrino mass scale, and the Dirac versus Majorana question, is the main unresolved issue. Here neutrinos are a hybrid between radiation and dark matter. If neutrinos were massless, the CNB today would be blackbody radiation with $T_\nu = 1.95\,\mathrm{K} = 0.168\,\mathrm{meV}$, whereas the minimal neutrino mass spectrum implied by flavor oscillations is $m_1 = 0$, $m_2 = 8.6$, and $m_3 = 50$ meV, but all masses could be larger in the form of a degenerate spectrum and the ordering could be inverted in the form $m_3 < m_1 < m_2$. One may actually question whether future CNB measurements would be part of traditional neutrino astronomy or the first case of dark-matter astronomy.

The large range of energies and the different types of sources and detectors makes it difficult to stay abreast of the developments in the entire field of neutrino astronomy. One first entry to the subject is afforded by a graphical representation and explanation of what we call the *grand unified neutrino spectrum*[1] (GUNS), a single plot of the neutrino and antineutrino background at Earth from the CNB in the meV range to the highest-energy cosmic neutrinos at PeV (10^{15} eV) energies (Koshiba, 1992; Cribier, Spiro, and Vignaud, 1995; Haxton and Lin, 2000; Becker, 2008; Spiering, 2012; Gaisser and Karle, 2017). As our main result we produce here an updated version of the GUNS plots shown in Fig. 1. The top panel shows the neutrino flux ϕ as a function of energy, while the energy flux $E \times \phi$ is shown in the bottom panel.

Our initial motivation for this task came from the low-energy part that traditionally shows a gap between solar neutrinos and the CNB, the latter usually depicted as blackbody radiation. However, the seemingly simple task of showing a new component, the keV thermal neutrino flux from the Sun and the neutrinos from β decays of primordial elements, in the context of the full GUNS quickly turned into a much bigger project because one is forced to think about all components.

While our review can be minimally thought of as an updated and annotated version of the traditional GUNS plot, ideally it serves as a compact resource for students and researchers to get a first sense, in particular, of those parts of the spectrum where they are no immediate experts. One model for our work could be the format of the minireviews provided by Tanabashi *et al.* (2018). In addition, we provide the input of what exactly went on the plot in the form of tables or analytic formulas; see Appendix D.

Astrophysical and terrestrial neutrino fluxes can be modified by any number of nonstandard effects, including mixing with hypothetical sterile neutrinos (Davidson *et al.*, 2003; Mention *et al.*, 2011; Abazajian *et al.*, 2012), large nonstandard interactions (Antusch, Baumann, and Fernández-Martínez, 2009; Biggio, Blennow, and Fernández-Martínez, 2009; Ohlsson, 2013), spin-flavor oscillations by large nonstandard magnetic dipole moments (Raffelt, 1990; Haft,

[1]We borrow this terminology from Ressell and Turner (1990).

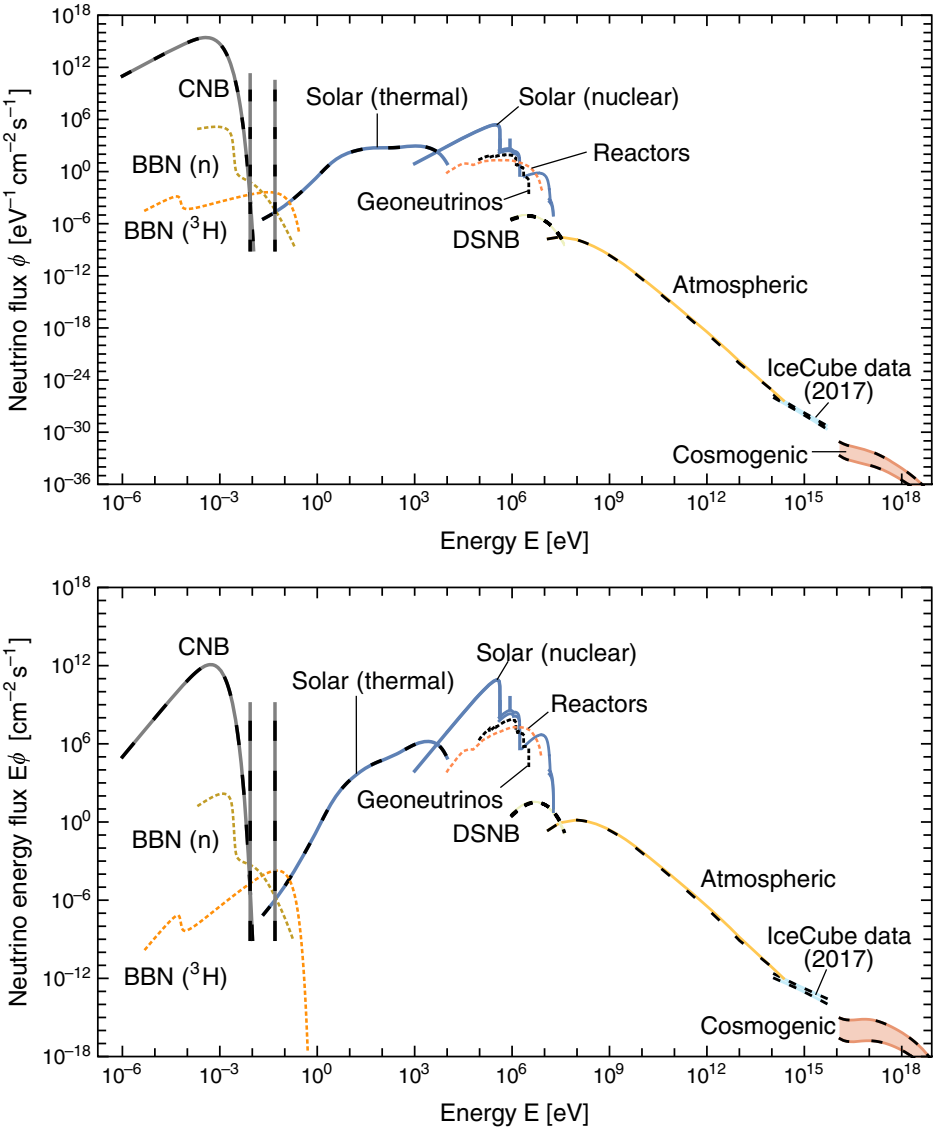

FIG. 1. Grand unified neutrino spectrum (GUNS) at Earth, integrated over directions and summed over flavors. Therefore, flavor conversion between source and detector does not affect this plot. Solid lines are displayed for neutrinos, dashed or dotted lines are displayed for antineutrinos, and superimposed dashed and solid lines are displayed for sources of both ν and $\bar{\nu}$. The fluxes from BBN, Earth, and reactors encompass only antineutrinos and the Sun emits only neutrinos, whereas all other components include both. The CNB is shown for a minimal mass spectrum of $m_1 = 0$, $m_2 = 8.6$, and $m_3 = 50$ meV, producing a blackbody spectrum plus two monochromatic lines of nonrelativistic neutrinos with energies corresponding to m_2 and m_3. See Appendix D for an exact description of the individual curves. Top panel: neutrino flux ϕ as a function of energy. Line sources are in units of cm^{-2} s^{-1}. Bottom panel: neutrino energy flux $E \times \phi$ as a function of energy. Line sources are in units of eV cm^{-2} s^{-1}.

Raffelt, and Weiss, 1994; Giunti and Studenikin, 2015), decay and annihilation into Majoron-like bosons (Schechter and Valle, 1982; Gelmini and Valle, 1984; Beacom and Bell, 2002; Beacom *et al.*, 2003; Pakvasa, Joshipura, and Mohanty, 2013; Pagliaroli *et al.*, 2015; Bustamante, Beacom, and Murase, 2017; Denton and Tamborra, 2018b; Funcke, Raffelt, and Vitagliano, 2020), for the CNB large primordial asymmetries and other novel early-Universe phenomena (Pastor, Pinto, and Raffelt, 2009; Arteaga *et al.*, 2017), or entirely new sources such as dark-matter decay (Barger *et al.*, 2002; Halzen and Klein, 2010; Esmaili and Serpico, 2013; Fan and Reece, 2013; Feldstein *et al.*, 2013; Agashe *et al.*, 2014; Bhattacharya, Reno, and Sarcevic, 2014; Higaki, Kitano, and Sato, 2014; Boucenna *et al.*, 2015; Fong *et al.*, 2015; Kopp, Liu, and Wang, 2015; Murase *et al.*, 2015; Rott, Kohri, and Park, 2015; Chianese *et al.*, 2016; Cohen *et al.*, 2017; Chianese *et al.*, 2019) and annihilation in the Sun or Earth (Silk, Olive, and Srednicki, 1985; Srednicki, Olive, and Silk, 1987; Ritz and Seckel, 1988; Kamionkowski, 1991; Cirelli *et al.*, 2005). In this review we do not explore such topics and instead stay in a minimal framework, which includes normal flavor conversion.

In this review we discuss the GUNS plots of Fig. 1 and review the different components in approximately increasing order of energy. In Sec. II we begin with the CNB, discussing primarily the impact of neutrino masses. In Fig. 1 we show a minimal example where the smallest neutrino mass vanishes, providing the traditional blackbody radiation, and two mass components that are nonrelativistic today.

In Sec. III we turn to neutrinos from the big-bang nucleosynthesis (BBN) epoch that form a small but dominant contribution at energies just above the CNB. This recently recognized flux derives from neutron and triton decays $n \to p + e^- + \bar{\nu}_e$ and ${}^3\mathrm{H} \to {}^3\mathrm{He} + e^- + \bar{\nu}_e$ that are left over from BBN.

In Sec. IV we turn to the Sun, which is especially bright in neutrinos because of its proximity, beginning with the traditional MeV-range neutrinos from nuclear reactions that produce only ν_e. We continue in Sec. V with a new contribution in the keV range of thermally produced fluxes that are equal for ν and $\bar{\nu}$. In both cases, what exactly arrives at Earth depends on flavor conversion, and for MeV energies also whether the Sun is observed from Earth or directly (day-night effect).

Nuclear fusion in the Sun produces only ν_e, implying that the MeV-range $\bar{\nu}_e$ fluxes, also modified by oscillations, are of terrestrial origin from nuclear fission. In Sec. VI we consider geoneutrinos that predominantly come from natural radioactive decays of potassium, uranium, and thorium. In Sec. VII we turn to nuclear power reactors. Both fluxes strongly depend on location, so their contributions to the GUNS are not universal.

In Sec. VIII we turn to the 1–100 MeV range where neutrinos from the next nearby stellar collapse, which could be an exploding or failed supernova, one of the most exciting albeit rare targets. However, some of the most interesting information is in the detailed time profile of these few-second bursts. Moreover, the range of expected distances is large and the signal depends on the viewing angle of these asymmetric events. Therefore, such sources fit poorly on the GUNS and are not shown in Fig. 1. On the other hand, the diffuse supernova neutrino background (DSNB) from all past collapsing stellar cores in the Universe dominates in the 10–50 MeV range (Sec. IX). If the CNB is all hot dark matter, the DSNB is actually the largest neutrino radiation component in the Universe. It may soon be detected by the upcoming JUNO and gadolinium-enhanced Super-Kamiokande experiments, thereby opening a new frontier.

Beyond the DSNB begins the realm of high-energy neutrinos. Up to about 10^{14} eV atmospheric neutrinos dominate (Sec. X). Historically they were the first "natural" neutrinos to be observed in the 1960s as mentioned earlier, and the observed up-down asymmetry by the Super-Kamiokande detector led to the first incontrovertible evidence for flavor conversion in 1998. Today, atmospheric neutrinos are still being used for oscillation physics. Otherwise they are mainly a background to astrophysical sources in this energy range.

In Sec. XI we turn to the range beyond atmospheric neutrinos. Since 2013, the IceCube observatory at the South Pole has reported detections of more than 100 high-energy cosmic neutrinos with energies 10^{14}–10^{16} eV, an achievement that marks the beginning of galactic and extragalactic neutrino astronomy. The sources of this apparently diffuse flux remain uncertain. At yet larger energies, a diffuse "cosmogenic neutrino flux" may exist as a result of possible cosmic-ray interactions at extremely high energies.

We conclude in Sec. XII with a summary and discussion of our results. We also speculate about possible developments in the foreseeable future.

II. COSMIC NEUTRINO BACKGROUND

The CNB, a relic from the early Universe when it was about 1 s old, consists today of about 112 cm^{-3} neutrinos plus antineutrinos per flavor. It is the largest neutrino density at Earth, yet it has never been measured. If neutrinos were massless, the CNB would be blackbody radiation at $T_\nu = 1.945\ \mathrm{K} = 0.168\ \mathrm{meV}$. However, the mass differences implied by flavor-oscillation data show that at least two mass eigenstates must be nonrelativistic today, providing a dark-matter component instead of radiation. The CNB and its possible detection is a topic tightly interwoven with the question of the absolute scale of neutrino masses and their Dirac versus Majorana nature.

A. Standard properties of the CNB

Cosmic neutrinos (Dolgov, 2002; Hannestad, 2006; Lesgourgues *et al.*, 2013; Lesgourgues and Verde, 2018) are a thermal relic from the hot early Universe, in analogy with the cosmic microwave background (CMB). At cosmic temperature T above a few MeV, photons, leptons, and nucleons are in thermal equilibrium, so neutrinos follow a Fermi-Dirac distribution. If the lepton-number asymmetry in neutrinos is comparable to that in charged leptons or to the primordial baryon asymmetry, i.e., of the order of 10^{-9}, their chemical potentials are negligibly small.

The true origin of primordial particle asymmetries remains unknown, but one particularly attractive scenario is leptogenesis, which is directly connected to the origin of neutrino masses (Fukugita and Yanagida, 1986; Buchmüller, Peccei, and Yanagida, 2005; Davidson, Nardi, and Nir, 2008). There exist many variations of leptogenesis, but its generic structure suggests sub-eV neutrino Majorana masses. In this sense, everything that exists in the Universe today may trace its fundamental origin to neutrino Majorana masses.

Much later in the cosmic evolution, at $T \sim 1$ MeV, neutrinos freeze out in that their interaction rates become slow compared to the Hubble expansion, but they continue to follow a Fermi-Dirac distribution at a common T because, for essentially massless neutrinos, the distribution is kinematically cooled by cosmic expansion. Around $T \sim 0.1$ MeV, electrons and positrons disappear, heating photons relative to neutrinos. In the adiabatic limit, one finds that afterward $T_\nu = (4/11)^{1/3} T_\gamma$. Based on the present-day value $T_{\mathrm{CMB}} = 2.725$ K one finds that $T_\nu = 1.945$ K today.

The radiation density after e^+e^- disappearance is provided by photons and neutrinos and, before the latter become nonrelativistic, is usually expressed as

$$\rho_{\rm rad} = [1 + N_{\rm eff}\tfrac{7}{8}(\tfrac{4}{11})^{4/3}]\rho_\gamma, \tag{1}$$

where the effective number of thermally excited neutrino degrees of freedom $N_{\rm eff}$ is a way to parametrize $\rho_{\rm rad}$. The standard value is $N_{\rm eff} = 3.045$ (de Salas and Pastor, 2016), where the deviation from 3 arises from residual neutrino heating by e^+e^- annihilation and other small corrections. Both big-bang nucleosynthesis and cosmological data, notably of the CMB angular power spectrum measured by Planck, confirm $N_{\rm eff}$ within ∼10% errors (Ade *et al.*, 2016; Cyburt *et al.*, 2016; Lesgourgues and Verde, 2018; Aghanim *et al.*, 2020).

While leptogenesis in the early Universe is directly connected to the origin of neutrino masses, they play no role in the subsequent cosmic evolution. In particular, sub-eV masses are too small for helicity-changing collisions to have any practical effect. If neutrino masses are of Majorana type and thus violate lepton number, any primordial asymmetry remains conserved, i.e., helicity plays the role of lepton number and allows for a chemical potential. In the Dirac case, the same reasoning implies that the sterile partners will not be thermally excited. Therefore, the standard CNB will be the same for both types of neutrino masses (Long, Lunardini, and Sabancilar, 2014; Balantekin and Kayser, 2018).

Leptogenesis is not proven and one may speculate about large primordial neutrino-antineutrino asymmetries in one or all flavors. In this case flavor oscillations essentially equilibrate the neutrino distributions before or around thermal freeze-out at $T \sim 1$ MeV so that, in particular, the ν_e chemical potential is representative of that for any flavor (Dolgov *et al.*, 2002; Castorina *et al.*, 2012). It is strongly constrained by big-bang nucleosynthesis and its impact on β equilibrium through reactions of the type $p + e^- \leftrightarrow n + \nu_e$. Moreover, a large neutrino asymmetry enhances $N_{\rm eff}$. Overall, a neutrino chemical potential, common to all flavors, is constrained by $|\mu_\nu/T| \lesssim 0.1$ (Castorina *et al.*, 2012; Oldengott and Schwarz, 2017), allowing at most for a modest modification of the radiation density in the CNB.

B. Neutrinos as hot dark matter

Flavor-oscillation data reveal the squared-mass differences discussed in Appendix B. They imply a minimal neutrino mass spectrum

$$m_1 = 0, \qquad m_2 = 8.6\ \text{meV}, \qquad m_3 = 50\ \text{meV} \tag{2}$$

that we will use as our reference case for plotting the GUNS. While normal mass ordering is favored by global fits, it could also be inverted ($m_3 < m_1 < m_2$) and there could be a common offset from zero. The value of the smallest neutrino mass remains a key open question.

In view of $T_\nu = 0.168$ meV for massless neutrinos, at least two mass eigenstates are dark matter today. Indeed, cosmological data provide restrictive limits on the hot dark-matter fraction, implying 95% C.L. limits on $\sum m_\nu$ in the range 0.11–0.68 eV, depending on the used datasets and cosmological model (Ade *et al.*, 2016; Lesgourgues and Verde, 2018; Aghanim *et al.*, 2020). Near-future surveys should be sensitive enough to actually provide a lower limit (Lesgourgues and Verde, 2018; Brinckmann *et al.*, 2019), i.e., a neutrino-mass detection perhaps even on the level of the minimal mass spectrum of Eq. (2).

Ongoing laboratory searches for neutrino masses include, in particular, the KATRIN experiment (Arenz *et al.*, 2018; Aker *et al.*, 2019) to measure the electron end-point spectrum in tritium β decay. The neutrino-mass sensitivity reaches about 0.2 eV for the common mass scale, i.e., a detection implies a significant tension with cosmological limits and thus points to a nonstandard CNB or other issues with standard cosmology. In the future, Project 8, an experiment based on cyclotron radiation emission spectroscopy, could reach a sensitivity down to 40 meV (Ashtari Esfahani *et al.*, 2017).

C. Spectrum at Earth

Which neutrino spectrum would be expected at Earth and should be shown on the GUNS plot? For neutrinos with mass, not the energy but the momentum is redshifted by cosmic expansion, so the phase-space occupation at redshift z for free-streaming neutrinos is

$$f_\nu(p) = \frac{1}{e^{p/T_z} + 1}, \tag{3}$$

where $T_z = T_\nu(1+z)$ and $T_\nu = 1.945$ K is today's temperature of hypothetical massless neutrinos. The present-day number density for one species of ν or $\bar\nu$, differential relative to momentum, is therefore

$$\frac{dn_\nu}{dp} = \frac{1}{2\pi^2}\frac{p^2}{e^{p/T_\nu} + 1}. \tag{4}$$

Integration provides $n_\nu = 56\ \text{cm}^{-3}$, as mentioned earlier.

Expressed as an isotropic flux, perhaps for a detection experiment, requires the velocity p/E with $E = \sqrt{p^2 + m_i^2}$, where m_i is one of the mass eigenstates $i = 1, 2$, or 3. Thus the isotropic differential flux today is

$$\frac{d\Phi_\nu}{dp} = \frac{p}{E}\frac{dn_\nu}{dp} = \frac{1}{2\pi^2}\frac{p^3}{\sqrt{p^2 + m_i^2}}\frac{1}{e^{p/T_\nu} + 1}. \tag{5}$$

In Fig. 2 we show this flux for our reference mass spectrum given in Eq. (2).

On the other hand, for plotting the GUNS the spectrum in terms of energy is more useful. In this case we need to include a Jacobian $dp/dE = E/p$ that cancels the velocity factor so that

$$\frac{d\Phi_\nu}{dE} = \frac{p}{E}\frac{dn_\nu}{dE} = \frac{1}{2\pi^2}\frac{E^2 - m_i^2}{e^{\sqrt{E^2 - m_i^2}/T_\nu} + 1}. \tag{6}$$

The maximum of this function does not depend on m_i and is $2.70 \times 10^{12}\ \text{cm}^{-2}\,\text{s}^{-1}\,\text{meV}^{-1}$. We show the energy spectrum for our reference neutrino masses in Fig. 3 and notice that for larger masses it is tightly concentrated at $E \gtrsim m_i$. Traditional GUNS plots (Becker, 2008; Spiering, 2012) apply only to massless neutrinos.

These results ignore that Earth is located in the gravitational potential of the Milky Way. Beginning with the momentum

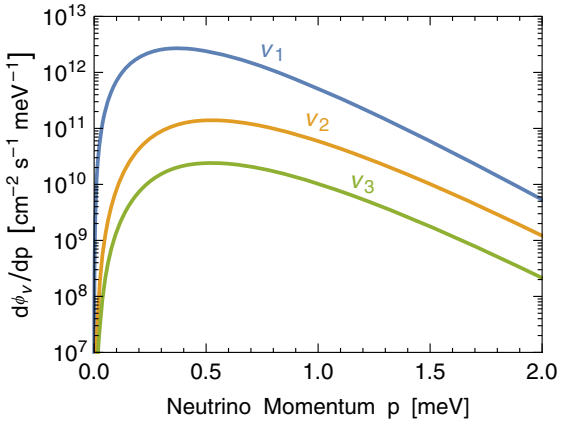

FIG. 2. Isotropic ν or $\bar{\nu}$ differential flux today ($d\Phi_\nu/dp$) for neutrinos with mass as given in Eq. (5). The different curves correspond to our reference mass spectrum of Eq. (2).

distribution of Eq. (4) we find the following for the average of the velocity $v = p/E$:

$$\langle v\rangle = \frac{2700\zeta_5}{7\pi^4}\frac{T}{m} + \mathcal{O}\left(\frac{T}{m}\right)^3 \approx 4.106\frac{T}{m}. \tag{7}$$

For $T = 0.168$ meV and $m = 50$ meV this is $\langle v\rangle = 1.38\times10^{-2}$, which is significantly larger than the galactic virial velocity of about 10^{-3}. Therefore, gravitational clustering is a small effect (Ringwald and Wong, 2004; de Salas *et al.*, 2017) and our momentum and energy distributions remain approximately valid if neutrino masses are as small as we have assumed.

One CNB mass eigenstate of ν_i plus $\bar{\nu}_i$ contributes at Earth a number and energy density of

$$n_{\nu\bar{\nu}} = 112\ \text{cm}^{-3}, \tag{8}$$

$$\rho_{\nu\bar{\nu}} = \begin{cases} 59.2\ \text{meV cm}^{-3} & \text{for } m_\nu \ll T_\nu, \\ 112\ \text{meV cm}^{-3}\,\frac{m_\nu}{\text{meV}} & \text{for } m_\nu \gg T_\nu, \end{cases} \tag{9}$$

ignoring small clustering effects in the Galaxy. Here $T_\nu = 1.95\ \text{K} = 0.168$ meV, as explained earlier.

The CNB consists essentially of an equal mixture of all flavors, so the probability of finding a random CNB ν or $\bar{\nu}$ in any of the mass eigenstates is equal to $1/3$. Put another way, if the neutrino distribution is uniform among flavors and thus their flavor matrix is proportional to the unit matrix, this is true in any basis.

D. Detection perspectives

Directly measuring the CNB remains extremely challenging (Ringwald, 2009; Vogel, 2015; Li, 2017). Those ideas based on the electroweak potential on electrons caused by the cosmic neutrino sea (Stodolsky, 1975), an $\mathcal{O}(G_\text{F})$ effect, depend on the net lepton number in neutrinos, which today we know cannot be large, as explained earlier, and also would be washed out in the limit of nonrelativistic neutrinos. Early proposals based on the use of the neutrino wind (Opher, 1974; Lewis, 1980) were found to be not viable, as there is no net acceleration (Cabibbo and Maiani, 1982).

At $\mathcal{O}(G_\text{F}^2)$ one can also consider mechanical forces on macroscopic bodies by neutrino scattering and the annual modulation caused by Earth's motion in the neutrino wind (Hagmann, 1999; Duda, Gelmini, and Nussinov, 2001), but the experimental realization of such ideas seems implausible with the available Cavendish-like balance technology. The results are also not encouraging for similar concepts based on interferometers (Domcke and Spinrath, 2017).

Another idea for the distant future is radiative atomic emission of a neutrino pair (Yoshimura, Sasao, and Tanaka, 2015). The CNB affects this process by Pauli phase-space blocking.

Extremely high-energy neutrinos, produced as cosmic-ray secondaries or from ultraheavy particle decay or cosmic strings, would be absorbed by the CNB, a resonant process if the CM energy matches the Z^0 mass (Weiler, 1982). For now there is no evidence for neutrinos in the required energy range beyond 10^{20} eV so that absorption dips cannot yet be looked for (Ringwald, 2009).

Perhaps the most realistic approach uses inverse β decay (Weinberg, 1962; Cocco, Mangano, and Messina, 2007; Lisanti, Safdi, and Tully, 2014; Long, Lunardini, and Sabancilar, 2014; Arteaga *et al.*, 2017; Akhmedov, 2019), notably on tritium $\nu_e + \text{H}^3 \to \text{He}^3 + e^-$, which was actually pursued by the PTOLEMY project (Betts *et al.*, 2013; Baracchini *et al.*, 2018). However, our reference scenario with the mass spectrum given in Eq. (2) is particularly difficult because ν_3 has the smallest ν_e admixture of all mass

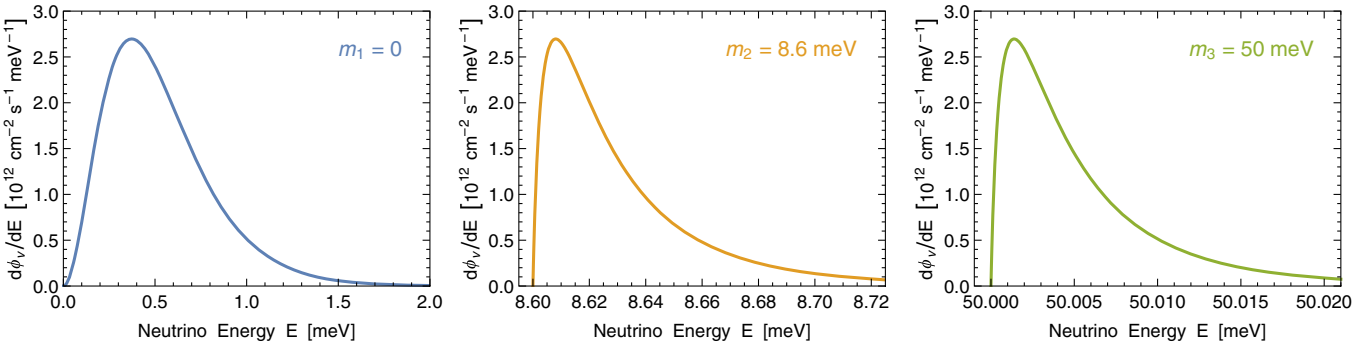

FIG. 3. Neutrino differential flux $d\Phi_\nu/dE$ according to Eq. (6) for our reference mass spectrum of Eq. (2). The maximum flux does not depend on m_ν and is 2.70×10^{12} cm^{-2} s^{-1} meV^{-1}.

eigenstates. On the other hand, if the mass spectrum is inverted and/or quasidegenerate, the detection opportunities may be more realistic. Such an experiment may also be able to distinguish Dirac from Majorana neutrinos (Long, Lunardini, and Sabancilar, 2014) and place constraints on nonstandard neutrino couplings (Arteaga *et al.*, 2017). Moreover, polarization of the target might achieve directionality (Lisanti, Safdi, and Tully, 2014).

The properties of the CNB, the search for the neutrino-mass scale, and the Dirac versus Majorana question remain at the frontier of particle cosmology and neutrino physics. Moreover, while neutrinos are but a small dark-matter component, detecting the CNB would be a first step in the future field of dark-matter astronomy.

III. NEUTRINOS FROM BIG-BANG NUCLEOSYNTHESIS

During its first few minutes, the Universe produces the observed light elements. Subsequent decays of neutrons ($n \to p + e + \bar{\nu}_e$) and tritons ($^3\mathrm{H} \to {}^3\mathrm{He} + e + \bar{\nu}_e$) produce an extremely small $\bar{\nu}_e$ flux, which, however, dominates the GUNS in the gap between the CNB and thermal solar neutrinos roughly for $E_\nu = 10$–100 meV. While a detection is currently out of the question, it would provide a direct observational window to primordial nucleosynthesis.

A. Primordial nucleosynthesis

Big-bang nucleosynthesis of the light elements is one of the pillars of cosmology (Alpher, Bethe, and Gamow, 1948; Alpher and Herman, 1950; Steigman, 2007; Iocco *et al.*, 2009; Cyburt *et al.*, 2016) and historically has led to a prediction of the CMB long before it was actually detected (Gamow, 1946; Alpher and Herman, 1948; Alpher and Herman, 1988). In the early Universe, protons and neutrons are in β equilibrium, so their relative abundance is $n/p = \exp(-\Delta m/T)$ with $\Delta m = 1.293$ MeV their mass difference. Weak interactions freeze out about 1 s after the big bang when $T \approx 1$ MeV, leaving $n/p \approx 1/6$. Nuclei form only 5 min later, when T falls below 60 keV and the large number of thermal photons no longer keeps nuclei dissociated. Neutrons decay, but their lifetime of 880 s leaves about $n/p \approx 1/7$ at that point. Subsequently most neutrons end up in ^{4}He, leaving the famous primordial helium mass fraction of 25%.

In detail, one has to solve a nuclear reaction network in the expanding Universe and finds the evolution of light isotopes as shown in Fig. 4,[2] where neutrons and the unstable isotopes are shown in color. Besides the nuclear-physics input, the result depends on the cosmic baryon fraction $\eta = n_B/n_\gamma$. With $\eta = 6.23 \times 10^{-10}$, which was chosen in Fig. 4, and the density $n_\gamma = 411\ \mathrm{cm}^{-3}$ of CMB photons, the baryon density is $n_B = 2.56 \times 10^{-7}\ \mathrm{cm}^{-3}$. The 95% C.L. range for n_B is 2.4–2.7 in these units (Tanabashi *et al.*, 2018). Of particular interest are the unstable but long-lived isotopes tritium (T) and ^{7}Be for which Fig. 4 shows final mass fractions 1.4×10^{-7} and 3.1×10^{-9}, corresponding to

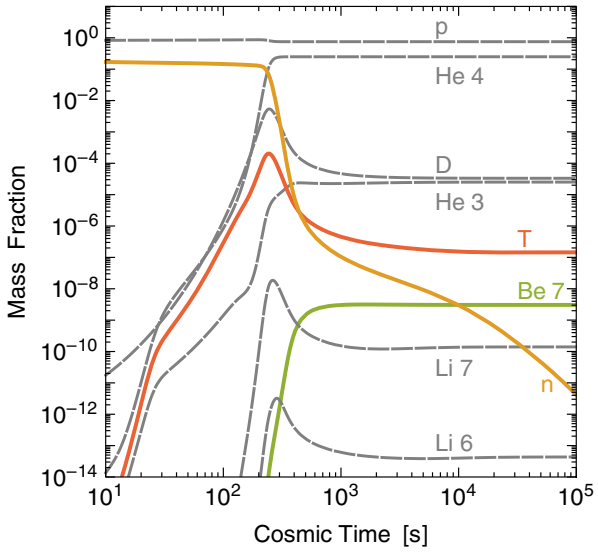

FIG. 4. Evolution of light-element abundances in the early Universe as indicated by the lines. Colored (solid) lines are neutrons (n) and the unstable isotopes tritium (T) and beryllium (^{7}Be) that produce $\bar{\nu}_e$ and that have not survived until today. Adapted from the Cococubed website, where $\eta = 6.23 \times 10^{-10}$ and $H_0 = 70.5\ \mathrm{km\,s^{-1}\,Mpc^{-1}}$ were used.

$$n_{\mathrm{T}} = 1.2 \times 10^{-14}\ \mathrm{cm}^{-3}, \tag{10a}$$

$$n_{^7\mathrm{Be}} = 1.1 \times 10^{-16}\ \mathrm{cm}^{-3} \tag{10b}$$

in terms of a present-day number density.

B. Neutrinos from decaying light isotopes

The isotopes shown in color in Fig. 4 are β unstable and thus produce a small cosmic $\bar{\nu}_e$ or ν_e density that is much smaller than the CNB density given in Eq. (8), but shows up at larger energies because of less redshifting due to late decays (Khatri and Sunyaev, 2011; Ivanchik and Yurchenko, 2018; Yurchenko and Ivanchik, 2019). Ignoring for now the question of neutrino masses and flavor conversion, the resulting present-day number densities are shown in Fig. 5 in comparison with the CNB (Sec. II) and the low-energy tail of thermal solar neutrinos (Sec. V). These two sources produce $\nu\bar{\nu}$ pairs of all flavors, so their number density is equal for ν and $\bar{\nu}$. In Fig. 5 we show the all-flavor ν density of these sources, equal to that for $\bar{\nu}$, to compare with either the ν or $\bar{\nu}$ density of BBN neutrinos. The low-energy tail of traditional solar ν_e from nuclear reactions (Sec. IV) and of the $\bar{\nu}_e$ geoneutrino (Sec. VI) and reactor fluxes (Sec. VII) are all much smaller than the solar thermal ν or $\bar{\nu}$ flux. One concludes that the BBN neutrinos ($\bar{\nu}_e$) from later neutron (n) and tritium decays produce the dominant density in the valley between the CNB and thermal solar neutrinos around neutrino energies of 10–200 meV. A detection of this flux is not possible with present-day technology.

Beryllium recombination.—Considering the individual sources in more detail, we begin with ^{7}Be, which emerges with a much larger abundance than ^{7}Li. Eventually it decays to ^{7}Li by electron capture, producing ν_e of 861.8 (89.6%) or

[2]See http://cococubed.asu.edu/code_pages/net_bigbang.shtml.

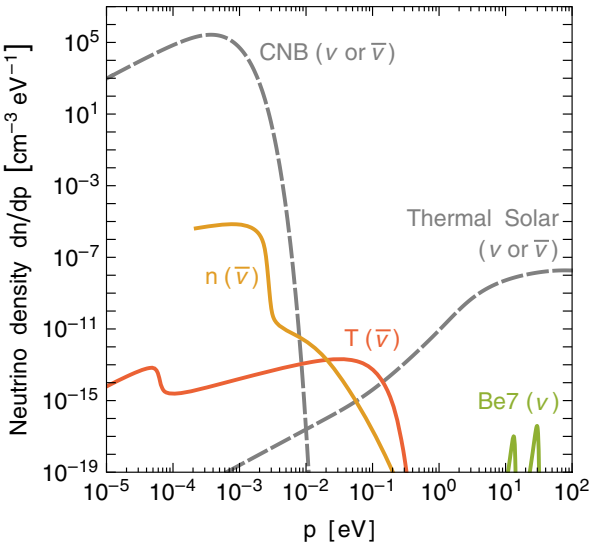

FIG. 5. Density of low-energy neutrinos, taken to be massless ($p = E$). The CNB and thermal solar neutrinos include all flavors, but the lines are only for either ν or $\bar{\nu}$. Colored (solid) lines are BBN neutrinos: $\bar{\nu}_e$ from n and tritium decay and ν_e from ^{7}Be electron capture.

384.2 keV (10.4%), which is analogous to the solar ^{7}Be flux (Sec. IV). However, the electrons captured in the Sun are free, so their average energy increases by a thermal amount of a few keV (Table I). In the dilute plasma of the early Universe, electrons are captured from bound states, which happens only at around 900 yr (cosmic redshift $z_{\rm rec} \approx 29,200$) when ^{7}Be atoms form. The kinetics of ^{7}Be recombination and decay was solved by Khatri and Sunyaev (2011), who found $z_{\rm rec}$ to be larger by about 5000 than implied by the Saha equation. The present-day energies of the lines are $13.1\ {\rm eV} = 384.2\ {\rm keV}/(z_{\rm rec}+1)$ and $29.5\ {\rm eV} = 861.8\ {\rm keV}/(z_{\rm rec}+1)$, each with a full width at half maximum of 7.8%, given by the redshift profile of ^{7}Be recombination, i.e., 1.0 and 2.3 eV.

The ^{7}Be lines in Fig. 5 were extracted from Fig. 5 of Khatri and Sunyaev (2011) with two modifications. The integrated number densities in the lines should be 10.4: 89.6 according to the branching ratio of the ^{7}Be decay, whereas in Khatri and Sunyaev (2011) the strength of the lower-energy line is reduced by an additional factor $(384.2/861.8)^2$ that we have undone.[3] Moreover, we have multiplied both lines by a factor 5.6 to arrive at the number density $n_{\rm Be7}$ of Eq. (10). Notice that Khatri and Sunyaev (2011) cited a relative ^{7}Be number density at the end of BBN of around 10^{-10}, whereas their cited literature and also Fig. 4 show about 5 to 6 times more.

Tritium decay.—BBN produces a tritium (T or ^{3}H) abundance given in Eq. (10) that later decays with a lifetime of 17.8 yr by $^3{\rm H} \to {}^3{\rm He} + e + \bar{\nu}_e$, producing the same number density of $\bar{\nu}_e$ with a spectral shape given by Eq. (17), with $E_{\rm max} = 18.6$ keV. During radiation domination, a cosmic age of 17.8 yr corresponds to a redshift of 2×10^5, so an energy of 18.6 keV is today 90 meV, explaining the $\bar{\nu}_e$ range shown in Fig. 5.

This spectrum is from Fig. 2 of Ivanchik and Yurchenko (2018). Preasymptotic tritium (i.e., the population existing at the onset of BBN, identified by the spike in Fig. 4) was also included, producing the low-energy steplike feature. The isotropic flux shown by Ivanchik and Yurchenko (2018) was multiplied by a factor $2/c$ to obtain our number density.[4] Our integrated $\bar{\nu}_e$ density then corresponds well to the tritium density in Eq. (10).

Neutron decay.—After weak-interaction freeze-out near 1 s, neutrons decay with a lifetime of 880 s, producing $\bar{\nu}_e$ with a spectrum given by Eq. (17) with $E_{\rm max} = 782$ keV. The short lifetime implies that there is no asymptotic value around the end of BBN. Notice also that the late n evolution shown in Fig. 5 is not explained by decay alone, which implies a much faster decline; i.e., residual nuclear reactions provide a late source of neutrons. The $\bar{\nu}_e$ number density shown in Fig. 5 was obtained from Ivanchik and Yurchenko (2018) with the same prescription that we used for tritium.

C. Neutrinos with mass

The crossover region between CNB, BBN, and the solar neutrinos shown in Fig. 5 is at energies where sub-eV neutrino masses become important. For illustration we use the minimal masses in normal ordering of Eq. (2) with 0, 8.6, and 50 meV. Neutrinos reaching Earth will have decohered into mass eigenstates, so one needs to determine the three corresponding spectra.

The CNB consists essentially of an equal mixture of all flavors, so the probability for finding a random CNB neutrino or antineutrino in any of the mass eigenstates is

$$P_i^{\rm CNB} = \tfrac{1}{3} \quad \text{for } i = 1,2,3. \tag{11}$$

The flavor density matrix is essentially proportional to the unit matrix from the beginning and thus is the same in any basis. Flavor conversion has no effect.

On the other hand, the BBN neutrinos are produced in the e flavor, so their flavor content changes over time. Flavor evolution in the early Universe can involve many complications in that the matter effect at $T \gtrsim 1$ MeV is dominated by a thermal term (Nötzold and Raffelt, 1988). Moreover, neutrinos themselves are an important background medium, leading to collective flavor evolution (Kostelecky, Pantaleone, and Samuel, 1993; Duan, Fuller, and Qian, 2010).

However, the BBN neutrinos are largely produced after BBN is complete at $T \lesssim 60$ MeV. Scaling the present-day baryon density of 2.5×10^{-7} cm^{-3} to the post-BBN epoch provides a matter density of the order of 10^{-5} g cm^{-3}, much

[3]We thank Rishi Khatri for confirming this issue, which was caused at the level of plotting by a multiplication by 384.2/861.8 instead of 861.8/384.2 to convert the high-energy line to the low-energy one. The formula for the redshifted lines given in their Sec. IV is correct.

[4]We thank Ivanchik and Yurchenko (2018) for providing a data file for this curve and for explaining the required factor. They defined the flux of an isotropic gas by the number of particles passing through a 1 cm^2 disk per second according to their Eq. (7) and the following text, providing a factor $c/4$. Then they applied a factor of 2 to account for neutrinos passing from both sides. See Appendix A for our definition of an isotropic flux.

smaller than the density of Sun or Earth, so the matter or neutrino backgrounds are no longer important. For the purpose of flavor evolution of MeV-range neutrinos we are in vacuum and the mass content of the original states does not evolve. Thus we may use the best-fit probabilities P_{ei} of finding a ν_e or $\bar{\nu}_e$ in any of the mass eigenstates given in the top row of Eq. (B3),

$$P_1^{\rm BBN} = 0.681, \qquad P_2^{\rm BBN} = 0.297, \qquad P_3^{\rm BBN} = 0.022. \tag{12}$$

Notice that here we have forced the numbers to add up to unity to correct for rounding errors.

Thermal solar neutrinos emerge in all flavors, but not with equal probabilities (Vitagliano, Redondo, and Raffelt, 2017). For extremely low energies, the mass-eigenstate probabilities are [see the text following Eq. (25)]

$$P_1^{\rm Sun} = 0.432, \qquad P_2^{\rm Sun} = 0.323, \qquad P_3^{\rm Sun} = 0.245. \tag{13}$$

For higher energies, these probabilities are plotted in the bottom panel of Fig. 12.

The CNB and BBN neutrinos are produced with high energies and later their momenta are redshifted by cosmic expansion. Therefore, their comoving differential number spectrum dn/dp as a function of p remains unchanged. If we interpret the horizontal axis of Fig. 5 as p instead of E and the vertical axis as dn/dp instead of dn/dE, the CNB and BBN curves do not change, except that we get three curves, one for each mass eigenstate, with the relative amplitudes of Eqs. (11) and (12).

For thermal solar neutrinos, the same argument applies to bremsstrahlung, which dominates at low energies, because the spectrum is essentially determined by phase space alone (Sec. V.C). At higher energies, where our assumed small masses are not important, the mass also enters into the matrix element and one needs an appropriate evaluation of plasmon decay.

For experimental searches, the flux may be a more appropriate quantity. Multiplying the number density spectra of Fig. 5 for each p by the velocity $v_i = p/\sqrt{p^2 + m_i^2}$ provides the mass-eigenstate flux spectra $d\Phi/dp$ shown in Fig. 6 (top panel), which is in analogy with Fig. 2.

For experiments considering the absorption of neutrinos, e.g., inverse β decay on tritium, the energy E is a more appropriate variable than the momentum p, so we show $d\Phi/dE$ as a function of E in Fig. 6 (bottom panel). Notice that the velocity factor v_i is undone by a Jacobian E/p, so, for example, the maxima of the mass-eigenstate curves are the same for every m_i, as discussed in Sec. II.C and illustrated in Fig. 2. Relative to the massless case of Fig. 5, the vertical axis is simply scaled with a factor c, whereas the curves are compressed in the horizontal direction by $p \to E = \sqrt{p^2 + m_i^2}$. Effectively one obtains narrow lines at the nonvanishing neutrino masses that are vastly dominated by the CNB. The integrated fluxes of the three mass eigenstates in either ν or $\bar{\nu}$ are

$$\Phi_1 = 1.68 \times 10^{12}\ {\rm cm}^{-2}\,{\rm s}^{-1}, \tag{14a}$$

$$\Phi_2 = 1.35 \times 10^{11}\ {\rm cm}^{-2}\,{\rm s}^{-1}, \tag{14b}$$

$$\Phi_3 = 2.32 \times 10^{10}\ {\rm cm}^{-2}\,{\rm s}^{-1}, \tag{14c}$$

where we use Eqs. (7) and (8) of Sec. II.

Note that we assume $m_1 = 0$ in this section; a degenerate mass spectrum (i.e., $m_1 \gg T_\nu = 0.168$ meV) would make the flux densities of all mass eigenstates similar to each other, they would all have a spikelike behavior, and they would be shifted to larger energies. In this case there is no neutrino radiation in the Universe today, only neutrino hot dark matter.

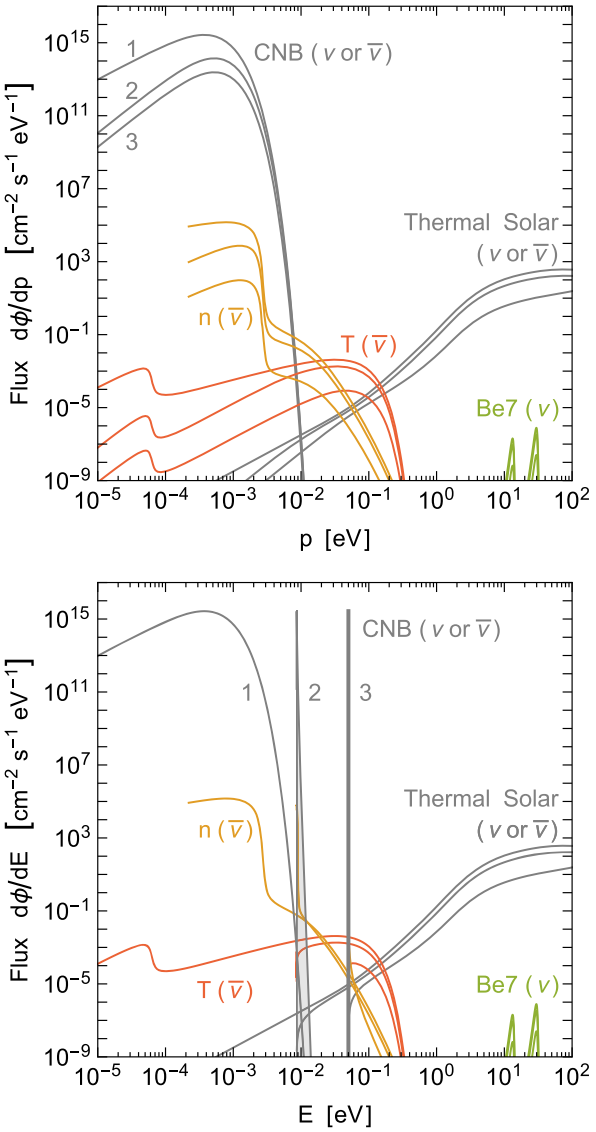

FIG. 6. Flux densities of mass-eigenstate neutrinos for $m_i = 0$, 8.6, and 50 meV as indicated at the curves, using the probabilities of Eqs. (11)–(13) and the spectra of Fig. 5. Top panel: $d\Phi/dp$, which includes a velocity factor $v_i = p/E_i$ for each mass state. Bottom panel: $d\Phi/dE$ showing sharp lines at $E = m_{2,3}$.

IV. SOLAR NEUTRINOS FROM NUCLEAR REACTIONS

The Sun emits 2.3% of its nuclear energy production in the form of MeV-range electron neutrinos. They arise from the

TABLE I. Neutrino fluxes at Earth from different nuclear reactions in the Sun. Theoretical predictions from Vinyoles *et al.* (2017) for models with GS98 (Grevesse and Sauval, 1998) and AGSS09 (Asplund *et al.*, 2009) abundances. The predicted electron-capture (EC) fluxes from the CNO cycle were obtained by scaling the β^+-decay fluxes (Stonehill, Formaggio, and Robertson, 2004). The neutrino end-point energy $E_{\max}$ and average $E_{\rm av}$ includes thermal energy of a few keV (Bahcall, 1997) except for the CNO-EC lines, where the given $E_{\rm av}$ is $E_{\max}+2m_e$ of the corresponding β^+ process. Observed fluxes with 1σ errors from the global analysis of Bergström *et al.* (2016).

					Flux at Earth			
Channel	Flux	Reaction	$E_{\max}$ (MeV)	$E_{\max}$ (MeV)	GS98	AGSS09	Observed	Units
pp chains (β^+)	Φ_{pp}	$p+p\to d+e^++\nu_e$	0.267	0.423	$5.98\pm0.6\%$	$6.03\pm0.5\%$	$5.971^{+0.62\%}_{-0.55\%}$	10^{10} cm^{-2} s^{-1}
	$\Phi_{\rm B}$	$^8{\rm B}\to{}^8{\rm Be}^*+e^++\nu_e$	6.735 ± 0.036	∼15	$5.46\pm12\%$	$4.50\pm12\%$	$5.16^{+2.5\%}_{-1.7\%}$	10^6 cm^{-2} s^{-1}
	$\Phi_{\rm hep}$	$^3{\rm He}+p\to{}^4{\rm He}+e^++\nu_e$	9.628	18.778	$0.80\pm30\%$	$0.83\pm30\%$	$1.9^{+63\%}_{-47\%}$	10^4 cm^{-2} s^{-1}
pp chains (EC)	$\Phi_{\rm Be}$	$e^-+{}^7{\rm Be}\to{}^7{\rm Li}+\nu_e$	0.863 (89.7%)		$4.93\pm6\%$	$4.50\pm6\%$	$4.80^{+5.9\%}_{-4.6\%}$	10^9 cm^{-2} s^{-1}
		$e^-+{}^7{\rm Be}\to{}^7{\rm Li}^*+\nu_e$	0.386 (10.3%)					
	$\Phi_{\rm pep}$	$p+e^-+p\to d+\nu_e$	1.445		$1.44\pm1\%$	$1.46\pm0.9\%$	$1.448^{+0.90\%}_{-0.90\%}$	10^8 cm^{-2} s^{-1}
CNO cycle (β^+)	$\Phi_{\rm N}$	$^{13}{\rm N}\to{}^{13}{\rm C}+e^++\nu_e$	0.706	1.198	$2.78\pm15\%$	$2.04\pm14\%$	<13.7	10^8 cm^{-2} s^{-1}
	$\Phi_{\rm O}$	$^{15}{\rm O}\to{}^{15}{\rm N}+e^++\nu_e$	0.996	1.732	$2.05\pm17\%$	$1.44\pm16\%$	<2.8	10^8 cm^{-2} s^{-1}
	$\Phi_{\rm F}$	$^{17}{\rm F}\to{}^{17}{\rm O}+e^++\nu_e$	0.998	1.736	$5.29\pm20\%$	$3.26\pm18\%$	<8.5	10^6 cm^{-2} s^{-1}
CNO Cycle (EC)	$\Phi_{\rm eN}$	$^{13}{\rm N}+e^-\to{}^{13}{\rm C}+\nu_e$	2.220		$2.20\pm15\%$	$1.61\pm14\%$	⋯	10^5 cm^{-2} s^{-1}
	$\Phi_{\rm eO}$	$^{15}{\rm O}+e^-\to{}^{15}{\rm N}+\nu_e$	2.754		$0.81\pm17\%$	$0.57\pm16\%$	⋯	10^5 cm^{-2} s^{-1}
	$\Phi_{\rm eF}$	$^{17}{\rm F}+e^-\to{}^{17}{\rm O}+\nu_e$	2.758		$3.11\pm20\%$	$1.91\pm18\%$	⋯	10^3 cm^{-2} s^{-1}

effective fusion reaction $4p+2e^-\to{}^4{\rm He}+2\nu_e+26.73$ MeV, which proceeds through several reaction chains and cycles. The history of solar neutrino measurements is tightly connected with the discovery of flavor conversion and the matter effect on neutrino dispersion. There is also a close connection to precision modeling of the Sun, leading to a new problem in the form of discrepant sound-speed profiles relative to helioseismology. This issue may well be related to the photon opacities and thus to the detailed chemical abundances in the solar core, a prime target of future neutrino precision experiments. Meanwhile, solar neutrinos are becoming a background to weakly interacting massive particle (WIMP) dark-matter searches. In fact, dark-matter detectors in the future may double as solar neutrino observatories.

A. The Sun as a neutrino source

The Sun produces nuclear energy by hydrogen fusion to helium that proceeds through the *pp* chains (exceeding 99% for solar conditions) and the rest through the CNO cycle (Clayton, 1983; Bahcall and Ulrich, 1988; Bahcall, 1989; Kippenhahn, Weigert, and Weiss, 2012; Haxton, Robertson, and Serenelli, 2013; Serenelli, 2016). For every produced ^{4}He nucleus, two protons need to convert to neutrons by what amounts to $p+e^-\to n+\nu_e$; i.e., two electrons disappear in the Sun and emerge as ν_e. The individual ν_e-producing reactions are listed in Table I (more details are provided later) and the expected flux spectra at Earth are shown in Fig. 7.

All *pp* chains begin with $p+p\to d+e^++\nu_e$, the *pp* reaction, which on average releases 0.267 MeV as ν_e. Including other processes (GS98 predictions of Table I) implies that $\langle E_{\nu_e}\rangle=0.312$ MeV. The solar luminosity without neutrinos is $L_\odot=3.828\times10^{33}$ erg s$^{-1}=2.39\times10^{39}$ MeV s^{-1}, implying a solar ν_e production of

$$L_{\nu_e}=2\times\frac{L_\odot}{26.73\ {\rm MeV}-2\langle E_{\nu_e}\rangle}=1.83\times10^{38}\ {\rm s}^{-1},\quad(15)$$

where 26.73 MeV is the energy released per He fusion and 2 is the number of neutrinos per fusion. The average distance of 1.496×10^{13} cm thus implies a flux, number density, and energy density at Earth of

$$\Phi_\nu=6.51\times10^{10}\ {\rm cm}^{-2}\,{\rm s}^{-1},\quad(16a)$$

$$n_\nu=2.17\ {\rm cm}^{-3},\quad(16b)$$

$$\rho_\nu=0.685\ {\rm MeV\,cm}^{-3}.\quad(16c)$$

These numbers change by ±3.4% in the course of the year due to the ellipticity of Earth's orbit, a variation confirmed by the Super-Kamiokande detector (Fukuda *et al.*, 2001).

While this overall picture is robust, the flux spectra of those reactions with larger E_{ν_e} are particularly important for detection and flavor-oscillation physics but are side issues for overall solar physics. Therefore, details of the production processes and of solar modeling are crucial for predicting the solar neutrino spectrum.

B. Production processes and spectra

The proton-neutron conversion required for hydrogen burning proceeds either as β^+ decay of the effective form $p\to n+e^++\nu_e$, producing a continuous spectrum, or as electron capture (EC) $e^-+p\to n+\nu_e$, producing a line spectrum. The nuclear MeV energies imply a much larger final-state β^+ phase space than the initial-state phase space occupied by electrons with keV thermal energies, so the continuum fluxes tend to dominate (Bahcall, 1990).

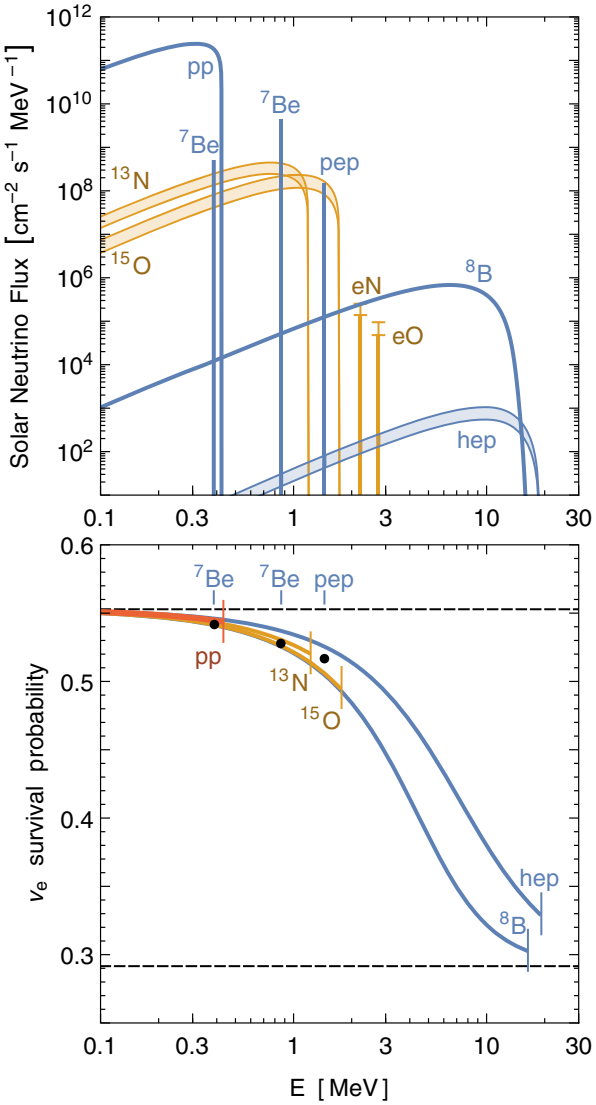

FIG. 7. Solar neutrinos from different source reactions. In blue (dark gray) pp-chain neutrinos (pp, ^{7}Be, pep, ^{8}B, hep), in orange (light gray) CNO neutrinos (^{13}N, ^{15}O, and the electron-capture lines eN and eO). Top panel: differential fluxes, where line sources are in units of cm^{-2} s^{-1}. pp-chain fluxes (except for hep) according to the measurements shown in Table I, where the uncertainties are too small to show. For the CNO and hep fluxes the range is bracketed by the lowest AGSS09 and highest GS98 predictions. ^{17}F is a small correction to the ^{15}O flux and thus not shown. Bottom panel: adiabatic ν_e survival probability due to flavor conversion (see Sec. IV.E), which depends on the radial distributions of the different production processes. For the eN and eO lines, these distributions have not been published. The black dots show the survival probabilities of the three pp-chain lines from ^{7}Be and pep. The horizontal dashed lines show the survival probability for vanishing and infinite neutrino energy.

Line energies are larger $+2m_e$ relative to the continuum end point and lines produce a distinct detection signature (Bellini *et al.*, 2014; Agostini *et al.*, 2019). The ^{7}Be line is particularly important because the nuclear energy is too small for β^+ decay. (In 10% of all cases it proceeds through an excited state of ^{7}Li, so there are two lines that together form the ^{7}Be flux.)

We neglect $^{3}\mathrm{He} + e^- + p \to {}^{4}\mathrm{He} + \nu_e$, the hep flux (Bahcall, 1990). On the other hand, we include the often neglected lines from EC in CNO reactions, also called ecCNO processes (Stonehill, Formaggio, and Robertson, 2004; Villante, 2015). Our flux predictions come from scaling the continuum fluxes (Vinyoles *et al.*, 2017) with the ratios provided by Stonehill, Formaggio, and Robertson (2004), although these are based on a different solar model. This inconsistency is small compared with the overall uncertainty of the CNO fluxes.

The end point $E_{\max}$ of a continuum spectrum is given in vacuum by the nuclear transition energy. However, for the reactions taking place in the Sun one needs to include thermal kinetic energy of a few keV. The end-point and average energies listed in Table I include this effect according to Bahcall (1997). For the same reason the EC lines are slightly shifted and have a thermal width of a few keV (Bahcall, 1993), which is irrelevant in practice for present-day experiments. The energies of the ecCNO lines were obtained from the listed continuum end points by adding $2m_e$, which agrees with Stonehill, Formaggio, and Robertson (2004) except for ^{17}F, where they show 2.761 instead of 2.758 MeV.

Except for ^{8}B, the continuum spectra follow from an allowed nuclear β decay, dominated by the phase space of the final-state e^+ and ν_e. In vacuum and ignoring e^+ final-state interactions it is

$$\frac{dN}{dE} \propto E^2(Q-E)\sqrt{(Q-E)^2 - m_e^2}, \tag{17}$$

where $Q = E_{\max} + m_e$. In Fig. 8 (dashed lines) we show these spectra in normalized form for the pp and hep fluxes as well as ^{15}O, representative of the CNO fluxes. We also show the spectra (solid lines), where final-state corrections and thermal initial-state distributions are included according to Bahcall (1997). Notice that the spectra provided on Bahcall's home page are not always exactly identical to those in Bahcall (1997).

The ^{8}B flux is the dominant contribution in many solar neutrino experiments because it reaches to large energies and

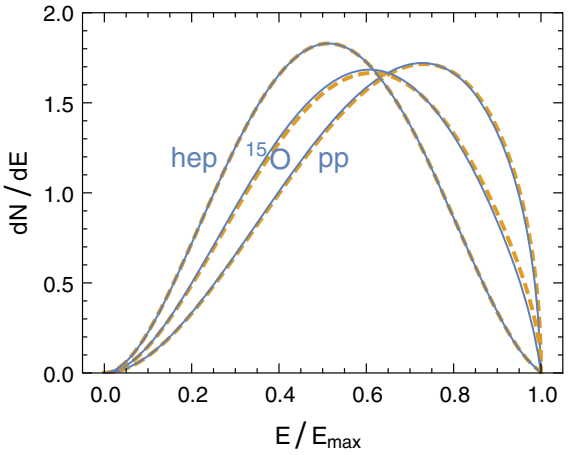

FIG. 8. Spectra of pp, ^{15}O, and hep neutrinos. The other CNO spectra are similar to ^{15}O. Solid lines: tabulated spectra are from Bahcall (1997). Dashed lines: allowed nuclear decay spectra according to Eq. (17).

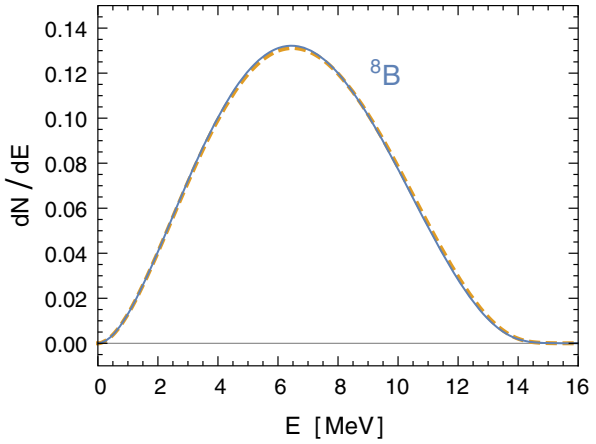

FIG. 9. Spectrum of ^{8}B neutrinos. Solid line: from Bahcall *et al.* (1996). Dashed line: from Winter *et al.* (2006).

the detection cross section typically scales with E^2, yet it is the one with the least simple spectrum. The decay $^8\mathrm{B} \to {}^8\mathrm{Be} + e^+ + \nu_e$ has no sharp cutoff because the final-state ^{8}Be is unstable against 2α decay. The ν_e spectrum can be inferred from the measured α and β^+ spectra. The ν_e spectrum provided by Bahcall *et al.* (1996) is shown in Fig. 9 as a solid line. As a dashed line we show the determination of Winter *et al.* (2006), based on a new measurement of the α spectrum.

For comparison with keV thermal neutrinos (Sec. V) it is useful to consider an explicit expression for the solar flux at low energies where the pp flux strongly dominates. Using the observed total pp flux from Table I, we find that an excellent approximation for the flux at Earth is

$$\frac{d\Phi_{pp}}{dE} = \frac{832.7\times10^{10}}{\mathrm{cm^2\,s\,MeV}}\left(\frac{E}{\mathrm{MeV}}\right)^2\left(1-2.5\frac{E}{\mathrm{MeV}}\right). \qquad (18)$$

To achieve subpercent precision, the purely quadratic term can be used for E up to a few keV. With the next correction, the expression can be used up to 100 keV.

C. Standard solar models

The neutrino flux predictions, such as those in Table I, depend on a detailed solar model that provides the variation of temperature, density, and chemical composition with radius. While the neutrino flux from the dominant pp reaction is largely determined by the overall luminosity, the small but experimentally dominant higher-energy fluxes depend on the branching between different terminations of the pp chains and the relative importance of the CNO cycle, all of which depends sensitively on chemical composition and temperature. For example, the ^{8}B flux scales approximately as T_c^{24} with solar-core temperature (Bahcall and Ulmer, 1996): the neutrino fluxes are sensitive solar thermometers.

The flux predictions are usually based on a standard solar model (SSM) (Serenelli, 2016), although the acronym might be more appropriately interpreted as simplified solar model. One assumes spherical symmetry and hydrostatic equilibrium, neglecting dynamical effects, rotation, and magnetic fields. The zero-age model is taken to be chemically homogeneous without further mass loss or gain. Energy is transported by radiation (photons) and convection. The latter is relevant only in the outer region (2% by mass or 30% by radius) and is treated phenomenologically with the adjustable parameter α_{MLT} to express the mixing length in terms of the pressure scale height.

Further adjustable parameters are the initial mass fractions of hydrogen X_{ini}, helium Y_{ini}, and "metals" (denoting anything heavier than helium) Z_{ini}, with the constraint $X_{\mathrm{ini}} + Y_{\mathrm{ini}} + Z_{\mathrm{ini}} = 1$. These parameters must be adjusted such that the evolution to the present age of $\tau_\odot = 4.57\times10^9$ yr reproduces the measured luminosity $L_\odot = 3.8418\times10^{33}$ erg s^{-1}, the radius $R_\odot = 6.9598\times10^{10}$ cm, and the spectroscopically observed metal abundance at the surface Z_{S} relative to that of hydrogen X_{S}. These surface abundances differ from the initial ones because of gravitational settling of heavier elements relative to lighter ones. As an example we show in Fig. 10 the radial variation of several solar parameters for a SMM of the Barcelona group (Vinyoles *et al.*, 2017).

The relative surface abundances of different elements are determined by spectroscopic measurements that agree well for nonvolatile elements with those found in meteorites. The older standard abundances (GS98) of Grevesse and Sauval (1998) were superseded in 2009 by the AGSS09 composition of Asplund, Grevesse, Sauval, and Scott and updated in 2015 (Asplund *et al.*, 2009; Grevesse *et al.*, 2015; Scott, Asplund *et al.*, 2015; Scott, Grevesse *et al.*, 2015). The AGSS09 composition shows significantly smaller abundances of volatile elements. According to Vinyoles *et al.* (2017), the surface abundances are $Z_{\mathrm{S}} = 0.0170 \pm 0.0012$ (GS98) and 0.0134 ± 0.0008 (AGSS09), with the difference almost entirely due to CNO elements.

The CNO abundances not only affect CNO neutrino fluxes directly but also determine the solar model through the photon opacities that regulate radiative energy transfer. Theoretical opacity calculations include OPAL (Iglesias and Rogers, 1996), the Opacity Project (Badnell *et al.*, 2005), OPAS (Blancard, Cossé, and Faussurier, 2012; Mondet *et al.*, 2015), STAR (Krief, Feigel, and Gazit, 2016), and OPLIB (Colgan *et al.*, 2016), which for solar conditions agree within 5% but strongly depend on input abundances.

A given SSM can be tested with helioseismology that determines the sound-speed profile, the depth of the convective zone R_{CZ}, and the surface helium abundance Y_{S}. The new spectroscopic surface abundances immediately caused a problem in that these parameters deviate significantly from the solar values, whereas the old GS98 abundances provide much better agreement (Grevesse and Sauval, 1998; Asplund *et al.*, 2009; Vinyoles *et al.*, 2017). (See Table II for a comparison using recent Barcelona models.)

Thus while SSMs with the old GS98 abundances provide good agreement with helioseismology, they disagree with the modern surface abundances, whereas for the AGSS09 class of models it is the other way around. There is no satisfactory solution to this conundrum, which is termed the "solar abundance problem," although it is not clear whether something is wrong with the abundances, the opacity calculations, other input physics, or any of the assumptions entering the SSM framework.

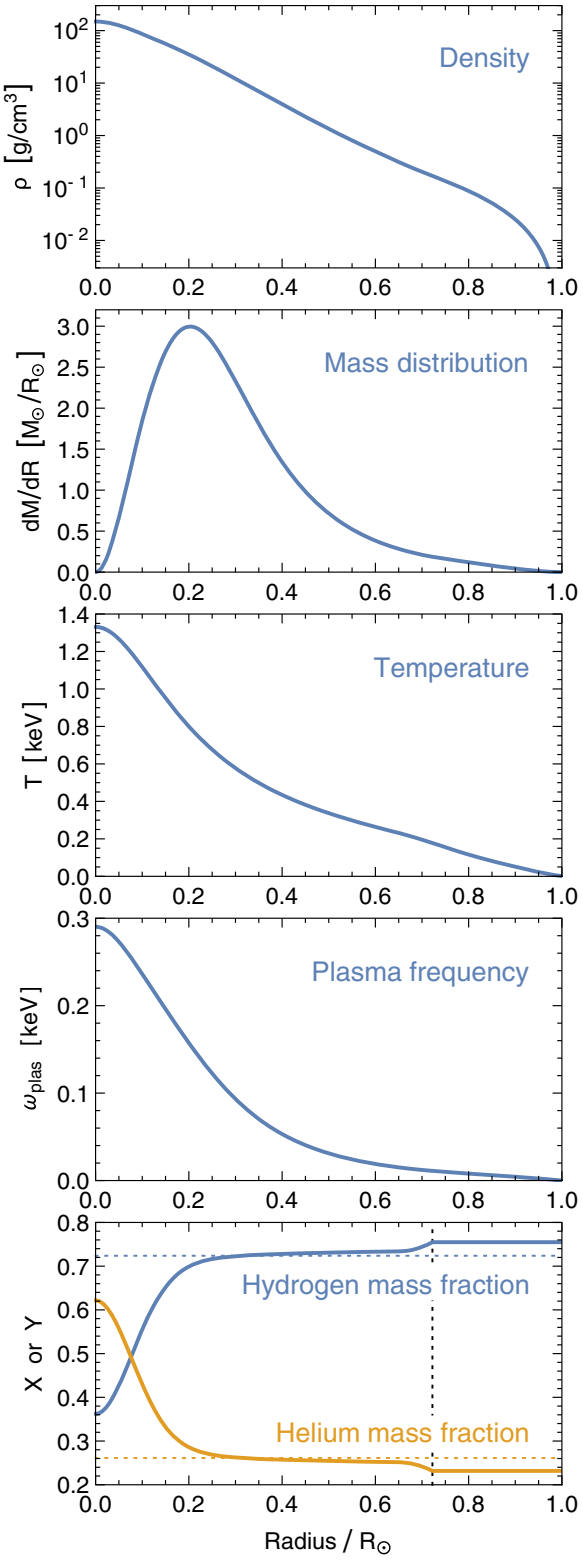

FIG. 10. Standard solar model of the Barcelona group (Vinyoles *et al.*, 2017) with AGSS09 composition. Bottom panel: the vertical dotted line shows the depth of the convection zone R_{CZ}, whereas the horizontal lines show the initial H and He mass fractions.

The pp-chain neutrino fluxes predicted by these two classes of models bracket the measurements (Table I), which, however, do not clearly distinguish between them. A future measurement of the CNO fluxes might determine the solar-core CNO abundances and thus help to solve the "abundance problem." While it is not assured that the two classes of models actually bracket the true case, one may speculate that the CNO fluxes might lie between the lowest AGSS09 and the largest GS98 predictions. Therefore, this range is taken to define the flux prediction shown in Fig. 7.

TABLE II. Main characteristics of two Barcelona SSMs of Vinyoles *et al.* (2017) with GS98 and AGSS09 abundances. R_{CZ} is the depth of the convection zone and $\langle \delta c/c \rangle$ is the average deviation of the sound-speed profile relative to helioseismic measurements.

Quantity	B16-GS98	B16-AGSS09	Solar[a]
Y_S	0.2426 ± 0.0059	0.2317 ± 0.0059	0.2485 ± 0.0035
$R_{CZ}/R_\odot$	0.7116 ± 0.0048	0.7223 ± 0.0053	0.713 ± 0.001
$\langle \delta c/c \rangle$	$0.0005^{+0.0006}_{-0.0002}$	0.0021 ± 0.001	⋯
α_{MLT}	2.18 ± 0.05	2.11 ± 0.05	⋯
Y_{ini}	0.2718 ± 0.0056	0.2613 ± 0.0055	⋯
Z_{ini}	0.0187 ± 0.0013	0.0149 ± 0.0009	⋯
Z_S	0.0170 ± 0.0012	0.0134 ± 0.0008	⋯

[a]See Basu and Antia (1997, 2004).

D. Antineutrinos

The Borexino scintillator detector has set the latest limit on the flux of solar $\bar{\nu}_e$ at Earth of 760 $\mathrm{cm^{-2}\,s^{-1}}$, assuming a spectral shape of the undistorted ^{8}B ν_e flux and using a threshold of 1.8 MeV (Bellini *et al.*, 2011). This corresponds to a 90% C.L. limit on a putative $\nu_e \to \bar{\nu}_e$ transition probability of 1.3×10^{-4} for $E_\nu > 1.8$ MeV.

In analogy with the geoneutrinos of Sec. VI, we find that the Sun contains a small fraction of the long-lived isotopes ^{40}K, ^{232}Th, and ^{238}U that produce a $\bar{\nu}_e$ flux (Malaney, Meyer, and Butler, 1990). However, it is immediately obvious that, at Earth's surface, this solar flux must be much smaller than that of geoneutrinos. If the mass fraction of these isotopes were the same in the Sun and Earth and if their distribution in Earth were spherically symmetric, the fluxes would have the proportions of $M_\odot/D_\odot^2$ vs $M_\oplus/R_\oplus^2$, with the solar mass $M_\odot$, its distance $D_\odot$, Earth's mass $M_\oplus$, and its radius $R_\oplus$. Thus the solar flux would be smaller in the same proportion as the solar gravitational field is smaller at Earth, i.e., about 6×10^{-4} times smaller.

The largest $\bar{\nu}_e$ flux comes from ^{40}K decay. The solar potassium mass fraction is around 3.5×10^{-6} (Asplund *et al.*, 2009), and the relative abundance of the isotope ^{40}K is 0.012%, so the ^{40}K solar mass fraction is 4×10^{-10}, corresponding to 8×10^{23} g of ^{40}K in the Sun or 1.3×10^{46} atoms. With a lifetime of 1.84×10^9 yr, the $\bar{\nu}_e$ luminosity is 2×10^{29} $\mathrm{s^{-1}}$ or a flux at Earth of around 100 $\mathrm{cm^{-2}\,s^{-1}}$. With a geo-$\bar{\nu}_e$ luminosity of around 2×10^{25} $\mathrm{s^{-1}}$ from potassium decay (Sec. VI), the average geoneutrino flux is 5×10^6 $\mathrm{cm^{-2}\,s^{-1}}$ at Earth's surface, although with large local variations.

An additional flux of higher-energy solar $\bar{\nu}_e$ comes from photofission of heavy elements such as uranium by the 5.5 MeV photon from the solar fusion reaction $p + d \to {}^3\mathrm{He} + \gamma$ (Malaney, Meyer, and Butler, 1990). One expects a $\bar{\nu}_e$ spectrum similar to a power reactor, where the fission is

caused by neutrons. However, this small flux of around 10^{-3} cm^{-2} s^{-1} is vastly overshadowed by reactor neutrinos.

E. Flavor conversion

While solar neutrinos are produced as ν_e, the flux at Earth shown in Fig. 7 (top panel) has a different composition because of flavor conversion on the way out of the Sun. The long distance between the Sun and Earth relative to the vacuum oscillation length implies that the propagation eigenstates effectively decohere, so we can picture the neutrinos arriving at Earth to be mass eigenstates. These can be reprojected on interaction eigenstates, notably on ν_e, if the detector is flavor sensitive.

Flavor conversion of solar neutrinos is almost perfectly adiabatic and, because of the hierarchy of neutrino-mass differences, well approximated by an effective two-flavor treatment. The probability of a produced ν_e to emerge at Earth in any of the three mass eigenstates is given by Eq. (C12), and the probability to be measured as the survival probability ν_e is given by Eq. (C13). For the limiting case of small E_ν, the matter effect is irrelevant and

$$P_{ee}^{\rm vac} = \frac{1+\cos^2 2\theta_{12}}{2}\cos^4\theta_{13} + \sin^4\theta_{13} = 0.533, \quad (19)$$

corresponding to the best-fit mixing parameters in normal ordering. In the other extreme of large energy or large matter density, one finds

$$P_{ee}^{\infty} = \frac{1-\cos 2\theta_{12}}{2}\cos^4\theta_{13} + \sin^4\theta_{13} = 0.292. \quad (20)$$

These extreme cases are shown as horizontal dashed lines in the lower panel of Fig. 7. Otherwise, P_{ee} depends on the weak potential at the point of production, so P_{ee} for a given E_ν depends on the radial source distributions in the Sun. These are shown in Fig. 11 according to an AGSS09 model of the Barcelona group, using the best-fit mixing parameters in normal ordering. Notice that such distributions for the EC-CNO reactions have not been provided but would be different from the continuum processes. The survival probabilities for the different source processes are shown in the lower panel of Fig. 7. As we see from the radial distributions of ^{8}B and hep, the corresponding curves in Fig. 7 essentially bracket the range of survival probabilities for all processes.

While neutrinos arriving at Earth have decohered into mass eigenstates, propagation through Earth causes flavor oscillations, producing coherent superpositions at the far end. Thus if the solar flux is observed through Earth ("at night"), this small effect needs to be included. This day-night asymmetry for the ^{8}B flux was measured by the Super-Kamiokande detector to be (Renshaw *et al.*, 2014; Abe *et al.*, 2016)

$$A_{\rm DN} = \frac{\Phi_{\rm day}-\Phi_{\rm night}}{(\Phi_{\rm day}+\Phi_{\rm night})/2} = (-3.3\pm 1.0_{\rm stat}\pm 0.5_{\rm syst})\%, \quad (21)$$

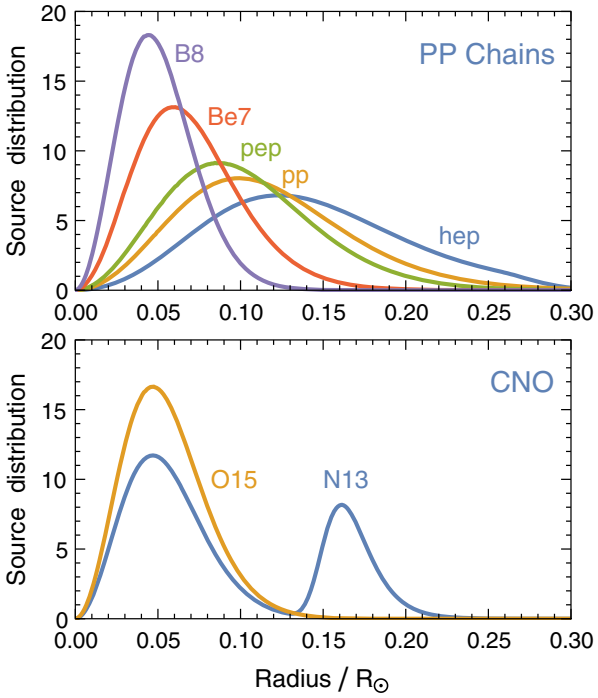

FIG. 11. Normalized distribution of neutrino production for the indicated source reactions according to the SSM of the Barcelona group (Vinyoles *et al.*, 2017) with AGSS09 composition. In the CNO cycle, the ^{17}F distribution is similar to that of ^{15}O.

corresponding to a 2.9σ significance. As measured in ν_e, the Sun shines brighter at night.

The energy-dependent ν_e survival probability for ^{8}B neutrinos shown in the lower panel of Fig. 7 implies a spectral deformation of the measured flux relative to the ^{8}B source spectrum. The latest Super-Kamiokande analysis (Abe *et al.*, 2016) is consistent with this effect, but also consistent with no distortion at all.

F. Observations and detection perspectives

Solar neutrino observations have a 50-year history, beginning in 1968 with the Homestake experiment (Davis, Harmer, and Hoffman, 1968; Cleveland *et al.*, 1998), a pioneering achievement that earned Raymond Davis the 2002 Nobel Prize in Physics. Homestake was based on the radiochemical technique of ^{37}Cl$(\nu_e, e^-)^{37}$Ar and subsequent argon detection, registering approximately 800 solar ν_e in its roughly 25 years of data taking that ended in 1994. Since those early days, many experiments have measured solar neutrinos (Wurm, 2017), and, in particular, Super-Kamiokande (Abe *et al.*, 2016), based on elastic scattering on electrons measured by Cherenkov radiation in water, has registered around 80 000 events since 1996 and has thus become sensitive to percent-level effects. The chlorine experiment was sensitive mainly to ^{8}B and ^{7}Be neutrinos, whereas the lowest threshold achieved for the water Cherenkov technique is around 4 MeV and thus registers only ^{8}B neutrinos.

Historically, the second experiment to measure solar neutrinos (1987–1995) was Kamiokande II and III in Japan (Hirata *et al.*, 1989; Fukuda *et al.*, 1996), a 2140 ton water

Cherenkov detector. Originally Kamiokande I was built to search for proton decay. Before measuring solar neutrinos, however, Kamiokande registered the neutrino burst from SN 1987A on February 23, 1987, feats that earned Masatoshi Koshiba the 2002 Nobel Prize in Physics.

The lower-energy fluxes, and notably the dominant pp neutrinos, became accessible with gallium radiochemical detectors using $^{71}\mathrm{Ga}(\nu_e, e^-)^{71}\mathrm{Ge}$. GALLEX (1991–1997) and subsequently GNO (1998–2003), using 30 tons of gallium, were mounted in the Italian Gran Sasso National Laboratory (Hampel *et al.*, 1999; Altmann *et al.*, 2005; Kaether *et al.*, 2010). The SAGE experiment in the Russian Baksan laboratory, using 50 tons of metallic gallium, has taken data since 1989 with results until 2007 (Abdurashitov *et al.*, 2009). However, the experiment keeps running (Shikhin *et al.*, 2017), mainly to investigate the gallium anomaly, a deficit of registered ν_e using laboratory sources (Giunti and Laveder, 2011), with a new source experiment BEST (Barinov *et al.*, 2018).

A breakthrough was achieved by the Sudbury Neutrino Observatory (SNO) in Canada (Chen, 1985; Aharmim *et al.*, 2010) that took data in two phases in the period 1999–2006. It used 1000 tons of heavy water (D_2O) and was sensitive to three detection channels: (i) Electron scattering $\nu + e \to e + \nu$, which is dominated by ν_e but has a small contribution from all flavors and is analogous to normal water Cherenkov detectors. (ii) Neutral-current dissociation of deuterons $\nu + d \to p + n + \nu$, which is sensitive to the total flux. (iii) Charged-current dissociation $\nu_e + d \to p + p + e$, which is sensitive to ν_e. Directly comparing the total ν flux with the ν_e one confirmed flavor conversion, an achievement honored with the 2015 Nobel Prize in Physics for Arthur MacDonald.

Another class of experiments uses mineral oil, augmented with a scintillating substance, to detect the scintillation light emitted by recoiling electrons in $\nu + e \to e + \nu$, which is analogous to the detection of Cherenkov light in water. While the scintillation light gain tends to be larger, one obtains no significant directional information. One instrument is KamLAND, using 1000 tons of liquid scintillator, which has taken data since 2002. It was installed in the cave of the decommissioned Kamiokande water Cherenkov detector. Its main achievement was to measure the $\bar{\nu}_e$ flux from distant power reactors to establish flavor oscillations. It has also measured the geoneutrino flux and today searches for neutrinoless double beta decay. In the solar neutrino context, it has measured the ^{7}Be and ^{8}B fluxes (Abe *et al.*, 2011; Gando *et al.*, 2015).

After the question of flavor conversion has largely been settled, the focus in solar neutrino research is precision spectroscopy, where the 300 ton liquid-scintillator detector Borexino in the Gran Sasso Laboratory, which has taken data since 2007, plays a leading role because of its extreme radiopurity. It has spectroscopically measured the pp, ^{7}Be, pep, and ^{8}B fluxes and has set the most restrictive constraints on the hep and CNO fluxes (Agostini *et al.*, 2018). The detection of the latter remains one of the main challenges in the field and might help to solve the solar opacity problem (Cerdeño *et al.*, 2018).

Recently, at the Neutrino 2020 virtual conference Borexino announced the first measurement of solar CNO neutrinos. The flux at Earth is found to be (Agostini *et al.*, 2020b)

$$\Phi_\nu = 7.0^{+3.0}_{-2.0} \times 10^8 \ \mathrm{cm}^{-2}\,\mathrm{s}^{-1}. \tag{22}$$

This result refers to the full Sun-produced flux after including the effect of adiabatic flavor Mikheyev-Smirnov-Wolfenstein (MSW) conversion. Making a comparison with the predictions shown in Table I, we find that there is agreement within the large experimental uncertainties after adding the C and N components. One cannot yet discriminate between the different opacity cases.

Future scintillator detectors with significant solar neutrino capabilities include the 1000 ton SNO+ (Andringa *et al.*, 2016), which uses the vessel and infrastructure of the decommissioned SNO detector, JUNO in China (An *et al.*, 2016), a shallow 20 kton medium-baseline precision reactor neutrino experiment that is under construction and is meant to measure the neutrino mass ordering, and the proposed 4 kton Jinping neutrino experiment (Beacom *et al.*, 2017), which would be located deep underground in the China Jinping Underground Laboratory (Cheng *et al.*, 2017). Recently, the SNO+ experiment measured the ^{8}B flux during its water commissioning phase (Anderson *et al.*, 2019).

The largest neutrino observatory will be the approved Hyper-Kamiokande experiment (Abe *et al.*, 2018), a 258 kton water Cherenkov detector (187 kton fiducial volume), which will register ^{8}B neutrinos, threshold 4.5 MeV visible energy, with a rate of 130 solar neutrinos/day.

Other proposed experiments include THEIA (Askins *et al.*, 2020), which would be the realization of the Advanced Scintillator Detector Concept (Alonso *et al.*, 2014). The latter would take advantage of new developments in water-based liquid scintillators and other technological advancements, the physics case ranging from neutrinoless double beta decay and supernova neutrinos to beyond the standard model physics (Orebi Gann, 2015). The liquid argon scintillator project DUNE, to be built for long-baseline neutrino oscillations, could also have solar neutrino capabilities (Capozzi *et al.*, 2019).

A new idea is to use dark-matter experiments to detect solar neutrinos, taking advantage of coherent neutrino scattering on large nuclei (Dutta and Strigari, 2019). For example, liquid argon–based WIMP direct detection experiments could be competitive in the detection of CNO neutrinos (Cerdeño *et al.*, 2018).

V. THERMAL NEUTRINOS FROM THE SUN

In the keV range, the Sun produces neutrino pairs of all flavors by thermal processes, notably plasmon decay, the Compton process, and electron bremsstrahlung. This contribution to the GUNS has never been shown, perhaps because no realistic detection opportunities exist at present. Still, this is the dominant ν and $\bar{\nu}$ flux at Earth for $E_\nu \lesssim 4$ keV. A future measurement would carry information about the solar chemical composition.

A. Emission processes

Hydrogen-burning stars produce neutrinos effectively by $4p + 2e \to {}^4\mathrm{He} + 2\nu_e$. These traditional solar neutrinos were discussed in Sec. IV, where we also discussed details about standard solar models. Moreover, all stars produce neutrino pairs by thermal processes, providing an energy-loss channel

that dominates in advanced phases of stellar evolution (Clayton, 1983; Bahcall, 1989; Raffelt, 1996; Kippenhahn, Weigert, and Weiss, 2012), whereas for the Sun it is a minor effect. The main processes are plasmon decay ($\gamma \to \bar{\nu} + \nu$), the Compton process ($\gamma + e \to e + \bar{\nu} + \nu$), bremsstrahlung ($e + Ze \to Ze + e + \bar{\nu} + \nu$), and atomic free-bound and bound-bound transitions. Numerical routines exist to couple neutrino energy losses with stellar evolution codes (Itoh *et al.*, 1996). A detailed evaluation of these processes for the Sun, including spectral information, was recently provided (Haxton and Lin, 2000; Vitagliano, Redondo, and Raffelt, 2017). While traditional solar neutrinos have MeV energies as behooves nuclear processes, thermal neutrinos have keV energies, corresponding to the temperature in the solar core.

Low-energy neutrino pairs are emitted by electrons, where we can use an effective neutral-current interaction of the form

$$\mathcal{L}_{\rm int} = \frac{G_{\rm F}}{\sqrt{2}} \bar{\psi}_e \gamma^\mu (C_{\rm V} - C_{\rm A}\gamma_5)\psi_e \bar{\psi}_\nu \gamma_\mu (1-\gamma_5)\psi_\nu. \quad (23)$$

Here $G_{\rm F}$ is Fermi's constant and the vector and axial-vector coupling constants are $C_{\rm V} = (1/2)(4\sin^2\Theta_W \pm 1)$ and $C_{\rm A} = \pm 1/2$ for ν_e (upper sign) and $\nu_{\mu,\tau}$ (lower sign). The flavor dependence derives from $W^\pm$ exchange in the effective e–ν_e interaction.

In the nonrelativistic limit, the emission rates for all processes are proportional to $(aC_{\rm V}^2 + bC_{\rm A}^2)G_{\rm F}^2$, where the coefficients a and b depend on the process, but always without a mixed term proportional to $C_{\rm V}C_{\rm A}$. This is a consequence of the nonrelativistic limit and implies that the flux and spectrum of ν and $\bar{\nu}$ are the same. Moreover, while $C_{\rm A}^2$ is the same for all flavors, the peculiar value $4\sin^2\Theta_W = 0.924\,88$ of the weak mixing angle implies that $C_{\rm V}^2 = 0.0014$ for $\nu_{\mu,\tau}$. Thus the vector-current interaction produces almost exclusively $\nu_e\bar{\nu}_e$ pairs and the thermal flux shows a strong flavor dependence.

The emission rates involve complications caused by in-medium effects such as screening in bremsstrahlung or electron-electron correlations in the Compton process. One can take advantage of the solar opacity calculations because the structure functions relevant for photon absorption carry-over to neutrino processes (Vitagliano, Redondo, and Raffelt, 2017). The overall precision of the thermal fluxes is probably on the 10% level, but a precise error budget is not available. Notice also that the solar opacity problem discussed in Sec. IV shows that on the precision level there remain open issues in our understanding of the Sun, probably related to the opacities or metal abundances, which may also affect thermal neutrino emission.

B. Solar flux at Earth

Integrating the emission rates over the Sun provides the flux at Earth shown in Fig. 12, where the exact choice of solar model is not important in view of the overall uncertainties. In the top panel, we show the flavor fluxes for unmixed neutrinos. The contribution from individual processes was discussed in detail by Vitagliano, Redondo, and Raffelt (2017). The nonelectron flavors are produced primarily by bremsstrahlung, although the Compton process dominates at the highest energies. For $\nu_e\bar{\nu}_e$, plasmon decay dominates, especially at lower energies. An additional source of ν_e derives from the nuclear pp process discussed in Sec. IV, which we show as a dashed line given by Eq. (18). For $E_\nu \lesssim 4$ keV, thermal neutrinos vastly dominate, and they always dominate for antineutrinos, overshadowing other astrophysical sources, e.g., primordial black holes decaying via Hawking radiation (Lunardini and Perez-Gonzalez, 2020).

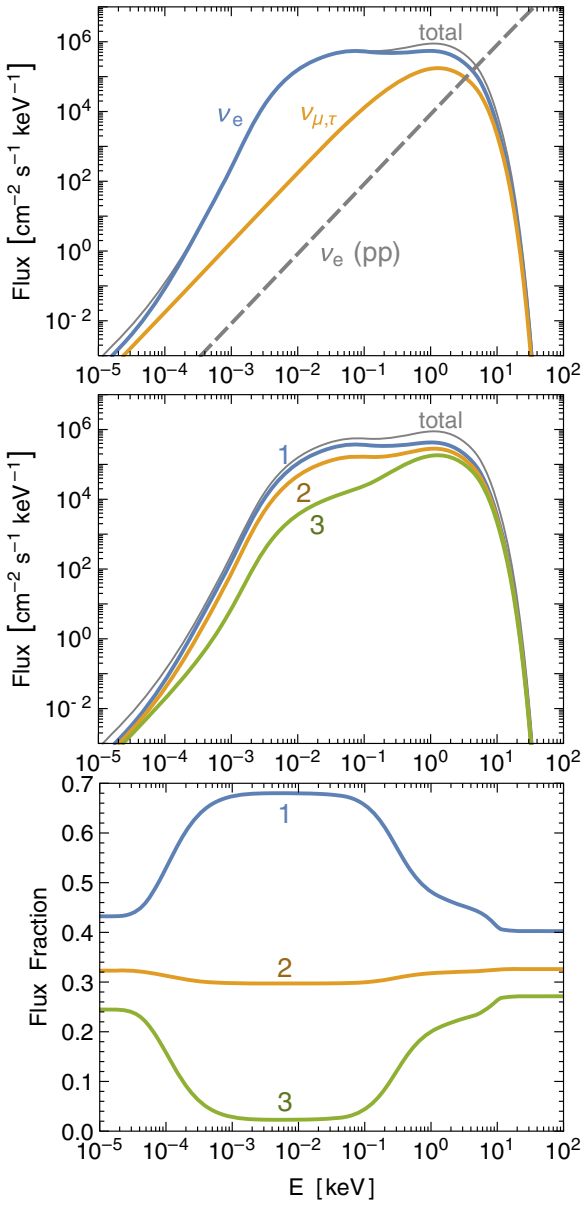

FIG. 12. Solar neutrino flux at Earth from thermal processes (Vitagliano, Redondo, and Raffelt, 2017). The antineutrino flux is the same. Top panel: flavor-eigenstate fluxes in the absence of oscillations. For comparison, we also show the low-energy tail from the nuclear pp reaction (dashed line), which produces only ν_e. Middle panel: mass-eigenstate fluxes for ν_i, with $i = 1, 2$, or 3 as indicated. This is the relevant representation for the fluxes arriving at Earth. Bottom panel: fractional mass-eigenstate fluxes.

Solar neutrinos arriving at Earth have decohered into mass eigenstates. They are produced in the solar interior, where according to Eq. (C5) the weak potential caused by electrons

is $V_e = \sqrt{2} G_F n_e \sim 7.8 \times 10^{-12}$ eV near the solar center. A comparison with $\delta m^2/2E = 3.7 \times 10^{-8}$ eV (keV/E) reveals that the matter effect is negligible for sub-keV neutrinos, which is in agreement with the discussion in Appendix C. Therefore, we can use the vacuum probabilities for a given flavor neutrino to be found in any of the mass eigenstates.

Specifically, from the top row of Eq. (B3), we use the best-fit probabilities for a ν_e or $\bar{\nu}_e$ to show up in a given mass eigenstate to be $P_{e1} = 0.681$, $P_{e2} = 0.297$, and $P_{e3} = 0.022$, which add up to unity. These probabilities apply to vector-current processes that produce almost pure $\nu_e \bar{\nu}_e$, whereas the axial-current processes, with equal C_A^2 for all flavors, can be thought of as producing an equal mixture of pairs of mass eigenstates. In this way we find the mass-eigenstate fluxes at Earth shown in the middle panel of Fig. 12 and the corresponding fractional fluxes in the bottom panel.

Integrating over energies implies a total flux, number density, and energy density at Earth of neutrinos plus antineutrinos of all flavors

$$\Phi_{\nu\bar{\nu}} = 6.2 \times 10^6 \text{ cm}^{-2}\,\text{s}^{-1}, \tag{24a}$$

$$n_{\nu\bar{\nu}} = 2.1 \times 10^{-4} \text{ cm}^{-3}, \tag{24b}$$

$$\rho_{\nu\bar{\nu}} = 507 \text{ meV cm}^{-3}, \tag{24c}$$

implying that $\langle E_\nu \rangle = \langle E_{\bar{\nu}} \rangle = 2.46$ keV. In analogy to traditional solar neutrinos, the flux and density changes by $\pm 3.4\%$ over the year due to the ellipticity of Earth's orbit. The local energy density in thermal solar neutrinos is comparable to the energy density of the CMB for massless cosmic neutrinos.

C. Extremely low energies

Thermal solar neutrinos appear to be the dominant flux at Earth for sub-keV energies all the way down to the CNB and the BBN neutrinos discussed in Secs. II and III. Therefore, it is useful to consider the asymptotic behavior at extremely low energies. For $E \lesssim 100$ meV, bremsstrahlung emission dominates that generically scales as E^2 at low energies (Vitagliano, Redondo, and Raffelt, 2017). A numerical integration over the Sun provides the low-energy flux at Earth from bremsstrahlung for either ν or $\bar{\nu}$:

$$\frac{d\Phi_\nu}{dE} = \frac{d\Phi_{\bar{\nu}}}{dE} = \frac{7.4 \times 10^6}{\text{cm}^2\,\text{s keV}} \left(\frac{E}{\text{keV}}\right)^2. \tag{25}$$

The fractions in the mass eigenstates 1, 2, and 3 are 0.432, 0.323, and 0.245, corresponding to the low-energy plateau in the bottom panel of Fig. 12 and which were already shown in the BBN context in Eq. (13). As explained by Vitagliano, Redondo, and Raffelt (2017), bremsstrahlung produces an almost pure $\nu_e \bar{\nu}_e$ flux by the vector-current interaction that breaks down into mass eigenstates according to the vacuum-mixing probabilities given in the top row of Eq. (B3). Moreover, bremsstrahlung produces all flavors equally by the axial-vector interaction. Adding the vector (28.4%) and axial-vector (71.6%) contributions provides these numbers.

One consequence of the relatively small bremsstrahlung flux is that there is indeed a window of energies between the CNB and extremely low-energy solar neutrinos where the BBN flux of Sec. III dominates.

For energies so low that the emitted neutrinos are not relativistic, this result needs to be modified. For bremsstrahlung, the emission spectrum is determined by phase space, so $d\dot{n} = Ap^2 dp = ApEdE$ with A some constant. For the flux of emitted neutrinos, we need a velocity factor $v = p/E$, so overall $d\Phi_\nu/dE \propto E^2 - m_\nu^2$ for $E \geq m_\nu$ and zero otherwise. The local density at Earth, on the other hand, does not involve p/E and thus is $dn_\nu/dE \propto E\sqrt{E^2 - m_\nu^2}$.

VI. GEONEUTRINOS

The decay of long-lived natural radioactive isotopes in Earth, notably ^{238}U, ^{232}Th, and ^{40}K, produce an MeV-range $\bar{\nu}_e$ flux exceeding 10^{25} s^{-1} (Marx and Menyhárd, 1960; Eder, 1966; Marx, 1969; Krauss, Glashow, and Schramm, 1984; Fiorentini, Lissia, and Mantovani, 2007; Dye, 2012; Bellini *et al.*, 2013; Ludhova and Zavatarelli, 2013; Smirnov, 2019). As these "geoneutrinos" are actually antineutrinos they can be detected despite the large solar neutrino flux in the same energy range. The associated radiogenic heat production is what drives much of geological activity such as plate tectonics or vulcanism. The abundance of radioactive elements depends on location, in principle allowing one to study Earth's interior with neutrinos,[5] although existing measurements by KamLAND and Borexino remain sparse.

A. Production mechanisms

Geoneutrinos are primarily $\bar{\nu}_e$ produced in decays of radioactive elements with lifetime comparable to the age of Earth, the so-called heat-producing elements (HPEs) (Ludhova and Zavatarelli, 2013; Smirnov, 2019). Geoneutrinos carry information on the HPE abundance and distribution and constrain the fraction of radiogenic heat contributing to the total surface heat flux of 50 TW. In this way, they provide indirect information on plate tectonics, mantle convection, and magnetic-field generation, as well as the processes that led to Earth's formation (Bellini *et al.*, 2013; Ludhova and Zavatarelli, 2013).

Around 99% of radiogenic heat comes from the decay chains of ^{232}Th, ^{238}U, and ^{40}K. The main reactions are (Fiorentini, Lissia, and Mantovani, 2007)

$$^{238}\text{U} \to {}^{206}\text{Pb} + 8\alpha + 8e + 6\bar{\nu}_e + 51.7 \text{ MeV}, \tag{26a}$$

$$^{232}\text{Th} \to {}^{208}\text{Pb} + 6\alpha + 4e + 4\bar{\nu}_e + 42.7 \text{ MeV}, \tag{26b}$$

$$^{40}\text{K} \to {}^{40}\text{Ca} + e + \bar{\nu}_e + 1.31 \text{ MeV}\ (89.3\%), \tag{26c}$$

$$e + {}^{40}\text{K} \to {}^{40}\text{Ar}^* + \nu_e + 0.044 \text{ MeV}\ (10.7\%). \tag{26d}$$

[5]See, for example, a dedicated conference series on Neutrino Geoscience (http://www.ipgp.fr/en/evenements/neutrino-geoscience-2015-conference) or Neutrino Research and Thermal Evolution of the Earth, Tohoku University, Sendai, October 25–27, 2016 (https://www.tfc.tohoku.ac.jp/event/4131.html).

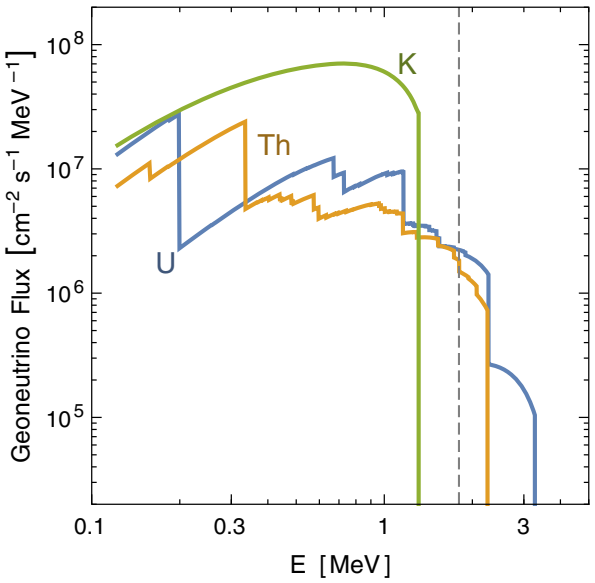

FIG. 13. Average geoneutrino flux ($\bar{\nu}_e$ before flavor conversion) from the main production chains, assuming the BSE model of Earth (Enomoto, 2005). The vertical dashed line marks the threshold of 1.806 MeV for inverse beta decay.

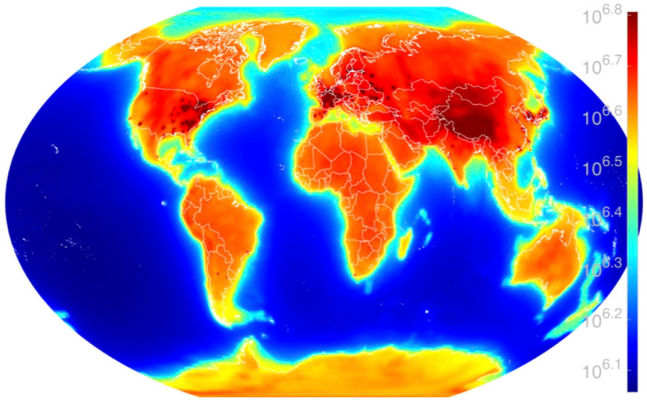

FIG. 14. Global map of the expected $\bar{\nu}_e$ flux (in cm^{-2} s^{-1}) of all energies from U and Th decays in Earth and from reactors. The hot spots in the Eastern U.S., Europe, and Japan are caused by nuclear power reactors. From Usman *et al.*, 2015.

The contribution from ^{235}U is not shown because of its small isotopic abundance. Electron capture on potassium is the only notable ν_e component, producing a monochromatic 44 keV line. Notice that it is followed by the emission of a 1441 keV γ ray to the ground state of ^{40}Ar. For the other reactions in Eq. (26) the average energy release in neutrinos is 3.96, 2.23, and 0.724 MeV per decay, respectively (Enomoto, 2005), while the remainder of the reaction energy shows up as heat. An additional 1% of the radiogenic heat comes from decays of ^{87}Rb, ^{138}La, and ^{176}Lu (Ludhova and Zavatarelli, 2013).

The geoneutrino spectra produced in these reactions, extending up to 3.26 MeV (Ludhova and Zavatarelli, 2013), depend on the possible decay branches and are shown in Fig. 13. The main detection channel is inverse beta decay $\bar{\nu}_e + p \to n + e^+$, with a kinematical threshold of 1.806 MeV (vertical dashed line in Fig. 13), implying that the large flux from ^{40}K is not detectable (Bellini *et al.*, 2013). On the other hand, a large fraction of the heat arises from the uranium and thorium decay chains. The resulting average flux is $\Phi_{\bar{\nu}_e} \simeq 2 \times 10^6$ cm^{-2} s^{-1}, which is comparable to the solar ν_e flux from ^{8}B decay. However, detecting geoneutrinos is more challenging because of their smaller energies.

The differential $\bar{\nu}_e$ geoneutrino flux at position $\vec{r}$ on Earth is given by the isotope abundances $a_i(\vec{r}')$ for any isotope i at the position $\vec{r}'$ and integrating over the entire Earth provides the expression (Fiorentini, Lissia, and Mantovani, 2007; Smirnov, 2019)

$$\Phi_{\bar{\nu}_e}(E,\vec{r}) = \sum_i A_i \frac{dn_i}{dE} \int_\oplus d^3\vec{r}' \frac{a_i(\vec{r}')\rho(\vec{r}')P_{ee}(E,|\vec{r}-\vec{r}'|)}{4\pi|\vec{r}-\vec{r}'|^2}. \quad (27)$$

Here dn_i/dE is the $\bar{\nu}_e$ energy spectrum for each decay mode, A_i is the decay rate per unit mass, $\rho(\vec{r})$ is the rock density, and P_{ee} is the $\bar{\nu}_e$ survival probability, where we have neglected matter effects so that P_{ee} depends only on the distance between production and detection points.

To evaluate Eq. (27) one needs to know the absolute amount and distribution of the HPEs. Although the crust composition is relatively well known, the mantle composition is quite uncertain (Fiorentini, Lissia, and Mantovani, 2007; Bellini *et al.*, 2013). Usually, the signal from the HPEs in the crust is computed on the basis of the total amount of the HPEs coming from the bulk silicate Earth (BSE) model, i.e., the model describing the Earth region outside its metallic core (McDonough and Sun, 1995; Palme and O'Neill, 2003); then the corresponding amount of elements in the mantle is extrapolated. The content of elements in Earth's mantle can be estimated on the basis of cosmochemical arguments, implying that abundances in the deep layers are expected to be larger than the ones in the upper samples.

Given their chemical affinity, the majority of HPEs are in the continental crust. This is useful as most of the detectors sensitive to geoneutrinos are on the continents and the corresponding event rate is dominated by Earth's contribution. Usually the continental crust is further divided into upper, lower, and middle continental crust. Among existing detectors, Borexino is placed on the continental crust in Italy (Caminata *et al.*, 2018; Agostini *et al.*, 2020a), while KamLAND is in a complex geological structure around the subduction zone (Gando *et al.*, 2013; Shimizu, 2017). An example for a global map of the expected $\bar{\nu}_e$ flux is shown in Fig. 14.

B. Earth modeling

Earth was created by accretion from undifferentiated material. Chondritic meteorites seem to resemble this picture in composition and structure. Earth can be divided into five regions according to seismic data: core, mantle, crust (continental and oceanic), and sediment. The mantle is solid but is affected by the convection that causes plate tectonics and earthquakes (Ludhova and Zavatarelli, 2013).

Seismology has shown that Earth is divided into several layers that can be distinguished by sound-speed discontinuities. Although seismology allows us to reconstruct the density

profile, it cannot determine the composition. The basic structure of Earth's interior is defined by the one-dimensional seismological profile dubbed the Preliminary Reference Earth Model (PREM), which is the basis for the estimation of geoneutrino production in the mantle (Dziewonski and Anderson, 1981). Meanwhile, thanks to seismic tomography, a three-dimensional view of the mantle structure has become available, for example, Laske *et al.* (2012) and Pasyanos *et al.* (2014), but differences with respect to the 1D PREM are negligible for geoneutrino estimation (Fiorentini, Lissia, and Mantovani, 2007).

As discussed in Sec. VI.A, uranium and thorium are the main HPEs producing detectable geoneutrinos. After the metallic core of Earth separated, the rest of Earth consisted of a homogeneous primitive mantle composed mainly of silicate rocks that then led to the formation of the present mantle and crust.

The outer layer is a thin crust that accounts for 70% of geoneutrino production (Fiorentini, Lissia, and Mantovani, 2007; Šrámek *et al.*, 2016). The crust probably hosts about half of the total uranium. The lithophile elements (uranium and thorium) tend to cluster in liquid phase and therefore concentrate in the crust, which is either oceanic or continental (Enomoto, 2005). The former is young and less than 10 km thick. The latter is thicker, more heterogeneous, and older that the oceanic counterpart. The crust is vertically stratified in terms of its chemical composition and is heterogeneous. The HPEs are distributed in both the crust and mantle. The geoneutrino flux strongly depends on location. In particular, the continental crust is about 1 order of magnitude richer in HPEs than the oceanic one. The continental crust is 0.34% of Earth's mass but contains 40% of the U and Th budget (Bellini *et al.*, 2013; Huang *et al.*, 2013).

The mantle, which consists of pressurized rocks at high temperature, can be divided into upper and lower mantles (Fiorentini, Lissia, and Mantovani, 2007). However, seismic discontinuities between the two parts do not divide the mantle into layers. We do not know whether the mantle moves as single or multiple layers, its convection dynamics, or whether its composition is homogeneous or heterogeneous. The available data are scarce and are restricted to the uppermost part.

Two models have been proposed (Hofmann, 1997). One is a two-layer model with a demarcation surface and a complete insulation between the upper mantle (poor in HPEs) and the lower layer. Another one is a fully mixed model, which is favored by seismic tomography. Concerning the estimation of the related geoneutrino flux, both models foresee the same amount of HPEs, but with different geometrical distributions (Mantovani *et al.*, 2004; Enomoto *et al.*, 2007). In the following, we assume a homogeneous distribution of U and Th in the mantle. Geophysicists have proposed models of mantle convection predicting that 70% of the total surface heat flux is radiogenic. Geochemists estimate this figure to be 25%; so the spread is large (Bellini *et al.*, 2013; Meroni and Zavatarelli, 2016).

Earth's innermost part is the core, which accounts for 32% of Earth's mass and is made of iron with small amounts of nickel (Fiorentini, Lissia, and Mantovani, 2007). Because of their chemical affinity, U and Th are believed to be absent in the core.

BSE models adopted to estimate the geoneutrino flux fall into three classes: geochemical, geodynamical, and cosmochemical (Ludhova and Zavatarelli, 2013). Geochemical models are based on the fact that the composition of carbonaceous chondrites matches the solar photospheric abundances of refractory lithophile and siderophile elements. A typical bulk-mass Th/U ratio is 3.9. Geodynamical models look at the amount of HPEs needed to sustain mantle convection. Cosmochemical models are similar to geochemical ones but assume a mantle composition based on enstatite chondrites and yield a lower radiogenic abundance.

A reference BSE model to estimate the geoneutrino production is the starting point for studying the expectations and potential of various neutrino detectors. It should incorporate the best available geochemical and geophysical information. The geoneutrino flux strongly depends on location, so the global map shown in Fig. 14 is only representative. It includes the geoneutrino flux from the U and Th decay chains as well as the reactor neutrino flux (Usman *et al.*, 2015).

A measurement of the geoneutrino flux could be used to estimate our planet's radiogenic heat production and to constrain the composition of the BSE model. A leading BSE model (McDonough and Sun, 1995) predicted a radiogenic heat production of 8 TW from ^{238}U, 8 TW from ^{232}Th, and 4 TW from ^{40}K, which together form about half the heat dissipation rate from Earth's surface. According to measurements in chondritic meteorites, the concentration mass ratio Th/U is 3.9. Currently, the uncertainties on the neutrino fluxes are as large as the predicted values.

The neutrino event rate is often expressed in terrestrial neutrino units (TNUs), i.e., the number of interactions detected in a target of 10^{32} protons (roughly corresponding to 1 kton of liquid scintillator) in 1 yr with maximum efficiency (Ludhova and Zavatarelli, 2013). Thus the neutrino event rates can be expressed as

$$^{232}\mathrm{Th}\ S = 4.07\ \mathrm{TNU} \times \Phi_{\bar{\nu}_e}/10^6\ \mathrm{cm}^{-2}\,\mathrm{s}^{-1}, \tag{28a}$$

$$^{238}\mathrm{U}\ S = 12.8\ \mathrm{TNU} \times \Phi_{\bar{\nu}_e}/10^6\ \mathrm{cm}^{-2}\,\mathrm{s}^{-1} \tag{28b}$$

for the thorium and uranium decay chains.

C. Detection opportunities

Geoneutrinos were first considered in 1953 to explain a puzzling background in the Hanford reactor neutrino experiment of Reines and Cowan, but even Reines's generous estimate of 10^8 cm^{-2} s^{-1} fell far short (the real explanation turned out to be cosmic radiation).[6] First realistic geoneutrino estimates appeared in the 1960s by Marx and Menyhárd (1960) and Marx (1969) and independently by Eder (1966), followed in the 1980s by Krauss, Glashow, and Schramm (1984).

[6]See Fiorentini, Lissia, and Mantovani (2007) for a reproduction of the private exchange between G. Gamow and F. Reines.

TABLE III. Geoneutrino observations. The Th/U abundance ratio is assumed to be the chondritic value.

	KamLAND[a]	Borexino[b]
Period	2002–2016	2007–2019
Live days	3900.9	3262.74
Exposure (10^{32} protons yr)	6.39	1.29 ± 0.05
IBD candidates	1130	154
Reactor $\bar{\nu}_e$	618.9 ± 33.8	$92.5^{+12.2}_{-9.9}$
Geoneutrinos (68% C.L.)		
Number of $\bar{\nu}_e$	139–192	43.6–62.2
Signal (TNU)	29.5–40.9	38.9–55.6
Flux (10^6 cm^{-2} s^{-1})	3.3–4.6	4.8–6.2

[a]See Watanabe (2016).
[b]See Agostini *et al.* (2020a).

The first experiment to report geoneutrino detection was KamLAND in 2005, a 1000 t liquid-scintillator detector in the Kamioka mine (Araki *et al.*, 2005a). The detection channel is inverse beta decay (IBD) ($\bar{\nu}_e + p \to n + e^+$) using delayed coincidence between the prompt positron and a delayed γ from neutron capture. The results were based on 749.1 live days, corresponding to an exposure of $(0.709 \pm 0.035) \times 10^{32}$ protons yr, providing 152 IBD candidates, of which 25^{+19}_{-18} were attributed to geo-$\bar{\nu}_e$. This signal corresponds to about one geoneutrino per month to be distinguished from a background that is 5 times larger. About 80.4 ± 7.2 of the background events were attributed to the $\bar{\nu}_e$ flux from nearby nuclear reactors: KamLAND was originally devised to detect flavor oscillations of reactor neutrinos (Sec. VII).

Over the years, the detector was improved, notably by background reduction through liquid-scintillator purification. A dramatic change was the shutdown of the Japanese nuclear power reactors in 2011 following the Fukushima Daiichi nuclear disaster (March 2011). For KamLAND this implied a reactor-off measurement of backgrounds and geoneutrinos that was included in the latest published results, based on data taken between March 9, 2002 and November 20, 2012 (Gando *et al.*, 2013). Preliminary results from data taken up to 2016, including 3.5 yr of a low-reactor period (and of this 2.0 yr reactor off), were shown at a conference in October 2016 (Watanabe, 2016) and also reported on by Smirnov (2019). We summarize these latest available measurements in Table III.

A second experiment that has detected geoneutrinos is Borexino, a 300 t liquid-scintillator detector in the Gran Sasso National Laboratory in Italy, reporting first results in 2010 (Caminata *et al.*, 2018). Despite its smaller size, Borexino is competitive because of its scintillator purity, large underground depth, and large distance from nuclear power plants, effects that all help to reduce backgrounds. Comprehensive results for the data-taking period December 2007–April 2019 were recently published (Agostini *et al.*, 2020a) and are summarized in Table III.

Reactor neutrinos (Sec. VII) are the main background for geoneutrino detection, whereas atmospheric neutrinos and the diffuse supernova neutrino background (Sec. IX) are negligible. Other spurious signals include intrinsic detector contamination, cosmogenic sources, and random coincidences of noncorrelated events. While the reactor flux at Borexino is usually much smaller than at KamLAND, the shutdown of the Japanese reactors has changed this picture for around 1/3 of the KamLAND live period. From Table III we conclude that at Borexino the reactor signal was around 1.7 times the geoneutrino signal, whereas at KamLAND this factor was on average around 3.7. Any of these $\bar{\nu}_e$ measurements refer to the respective detector sites and include the effect of flavor conversion on the way between source and detector.

The overall results in Table III assume a Th/U abundance ratio fixed at the chondritic value of 3.9, but both Borexino and KamLAND provide analyses with independent contributions. For example, KamLAND finds for the ratio $4.1^{+5.5}_{-3.3}$, which is consistent with the simplest assumption but with large uncertainties (Watanabe, 2016). KamLAND is also beginning to discriminate between the geodynamical, geochemical, and cosmochemical BSE models, somewhat disfavoring the latter. The radiogenic heat production is allowed to be roughly in the range 8–30 TW. Borexino finds a measured mantle signal of $21.2^{+9.5}_{-9.0}(\text{stat})^{+1.1}_{-0.9}(\text{syst})$ TNU, corresponding to the production of a radiogenic heat of $24.6^{+11.1}_{-10.4}$ TW (68% interval) from ^{238}U and ^{232}Th in the mantle. Assuming an 18% contribution of ^{40}K in the mantle and $8.1^{+1.9}_{-1.4}$ TW of the total radiogenic heat of the lithosphere, Borexino estimates the total radiogenic heat of Earth to be $38.2^{+13.6}_{-12.7}$ TW (Agostini *et al.*, 2020a). Overall, while the observation of geoneutrinos in these two detectors is highly significant, detailed geophysical conclusions ultimately require better statistics.

Several experiments, in different stages of development, will improve our knowledge. For example, SNO+ in Canada expects a geoneutrino rate of 20/yr (Arushanova and Back, 2017). The site is in the old continental crust containing felsic rocks that are rich in U and Th. The crust at the SNO+ location is especially thick, about 40% more than at Gran Sasso and Kamioka. JUNO in China also plans to measure geoneutrinos. Finally, the Hanohano project has been proposed in Hawaii, a 5 kton detector on the oceanic crust (Cicenas and Solomey, 2012). Because the oceanic crust is thin, 75% of the signal would come from the mantle.

VII. REACTOR NEUTRINOS

Nuclear power plants release a few percent of their energy production in the form of MeV-range $\bar{\nu}_e$ arising from the decay of fission products. In contrast to other human-made neutrino sources such as accelerators, reactors produce a diffuse flux that can dominate over geoneutrinos in entire geographic regions and are therefore a legitimate GUNS component. Historically, reactor neutrinos have been fundamental to the study of neutrino properties, including their first detection by Cowan and Reines in the 1950s, and they remain topical for measuring neutrino mixing parameters and possible sterile states (Giunti and Kim, 2007; Tanabashi *et al.*, 2018; Qian and Peng, 2019), as well as for many applied fields (Bergevin *et al.*, 2019).

A. Production and detection of reactor neutrinos

Nuclear power plants produce $\bar{\nu}_e$'s through β decays of neutron-rich nuclei. The main contributions come from the

fission of ^{235}U (56%), ^{239}Pu (30%), ^{238}U (8%), and ^{241}Pu (6%), where the percentages vary over time and we have reported typical values of fission fractions during operation (Giunti and Kim, 2007; Baldoncini *et al.*, 2015). In addition, below the detection threshold of inverse beta decay $E_{\rm min} = 1.8$ MeV there is another $\bar{\nu}_e$ source due to neutron captures. The most important is the decay of ^{239}U produced by the neutron capture on ^{238}U, which is usually written as $^{238}\mathrm{U}(n,\gamma)^{239}\mathrm{U}$. To obtain a basic estimate of the $\bar{\nu}_e$ flux from a reactor we note that on average a fission event releases about six neutrinos and a total energy of about 200 MeV. A nuclear power plant producing 1 GW of thermal power then produces a $\bar{\nu}_e$ flux of 2×10^{20} s^{-1} (Giunti and Kim, 2007).

The globally installed nuclear power corresponds to around 0.4 TW electric[7] or, with a typical efficiency of 33%,[8] to 1.2 TW thermal. This is a few percent of the natural radiogenic heat production in Earth, so the overall reactor neutrino flux is only a few percent of the geoneutrino flux, yet the former can dominate in some geographic regions and has a different spectrum.

Predicting the spectrum is a much more complicated task as many different decay branches must be included. In the last 50 years, two main approaches were used. One method predicts the time-dependent total flux by summing over all possible β-decay branches, but the spectrum is uncertain because the fission yields and end-point energies are often not well known, one needs a good model for the Coulomb corrections entering the Fermi function, etc. The alternative is to use the measured electron spectrum for different decay chains, which can be inverted by taking advantage of the relation

$$E_\nu = E_e + T_n + m_n - m_p \simeq E_e + 1.293 \text{ MeV}, \quad (29)$$

where T_n is the small recoil kinetic energy of the neutron and E_e is the energy of the outgoing positron.

Until 2011, the standard results were the ones obtained by Vogel and Engel (1989), but then two papers recalculated the spectrum at energies larger than 2 MeV with different methods, one by Huber (2011) and one by Mueller *et al.* (2011). Figure 15 shows the spectrum due to the dominant processes reported in Table II of Vogel and Engel (1989) for energies smaller than 2 MeV, while for larger energies we use Tables VII–IX of Huber (2011) for ^{235}U, ^{239}Pu, and ^{241}Pu and Table III of Mueller *et al.* (2011) for ^{238}U; finally, the low-energy spectrum of neutron capture $^{238}\mathrm{U}(n,\gamma)^{239}\mathrm{U}$ is directly extracted from Qian and Peng (2019). Notice that fits to the tables are reported in these references.

The detection of reactor neutrinos typically relies on inverse beta decay on protons $\bar{\nu}_e + p \to n + e^+$. The cross section is usually expressed in terms of well measured quantities such as

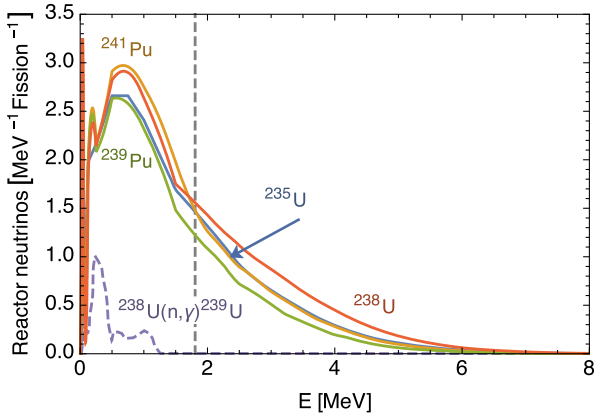

FIG. 15. The $\bar{\nu}_e$ energy spectra for ^{235}U, ^{238}U, ^{239}Pu, and ^{241}Pu fissions. The inverse beta-decay threshold is marked by a vertical dashed line. At low energies, the dominant contribution is due to neutron capture processes $^{238}\mathrm{U}(n,\gamma)^{239}\mathrm{U}$, here rescaled by a factor 1/20.

the neutron lifetime τ_n and the electron mass m_e (Vogel and Beacom, 1999),

$$\sigma_{\rm CC}^{\bar{\nu}_e p} = \frac{2\pi^2}{\tau_n m_e^5 f} E_e \sqrt{E_e^2 - m_e^2}. \quad (30)$$

Here f is the dimensionless phase-space integral

$$f = \int_{m_e}^{m_n - m_p} dE_e \frac{(m_n - m_p - E_e)^2 E_e \sqrt{E_e^2 - m_e^2}}{m_e^5}, \quad (31)$$

where we neglect the small neutron recoil energy. The detection signature features a prompt signal due to the positron followed by neutron capture. Alternatives to this process include charged- and neutral-current deuteron breakup using heavy water, $\bar{\nu}$-e elastic scattering, and coherent $\bar{\nu}$-nucleus interactions (Giunti and Kim, 2007).

As a typical example we show in Fig. 16 (top panel) the flux from the Japanese experimental fast reactor JOYO (Furuta *et al.*, 2012), which has 140 MW thermal power and a detector at the close distance of 24.3 m. Convolution with the inverse β cross section [Fig. 16 (bottom panel)] shows that the interactions peak for $E_{\bar{\nu}_e} \sim 4$ MeV. While the quantitative details strongly depend on the reactor and detector, several general features can be pointed out (Giunti and Kim, 2007). First, the large threshold implies that only reactions with large Q values can be observed, so only one-fourth of the total flux can be detected. Another important point is that reactor shutdowns can be used to measure background and that the intensity of the flux is proportional to the thermal power, which is accurately monitored. Moreover, the flux is extremely large, so the detectors do not need large shielding against cosmic rays. All of these advantages make reactor neutrinos a fundamental tool for measuring intrinsic neutrino properties such as mixing angles and mass differences.

The global flux is produced by around 500 reactors worldwide with an uneven geographic distribution. In Fig. 17 we show a global map, restricted to the narrow energy range 3.00–3.01 MeV, allowing one to discern flavor

[7]International Atomic Energy Agency, Power Reactor Information System; see https://pris.iaea.org/PRIS/.

[8]Thermal Efficiency of Nuclear Power Plants; see, for example, https://www.nuclear-power.net/nuclear-engineering /thermodynamics/laws-of-thermodynamics/thermal-efficiency/thermal-efficiency-of-nuclear-power-plants/.

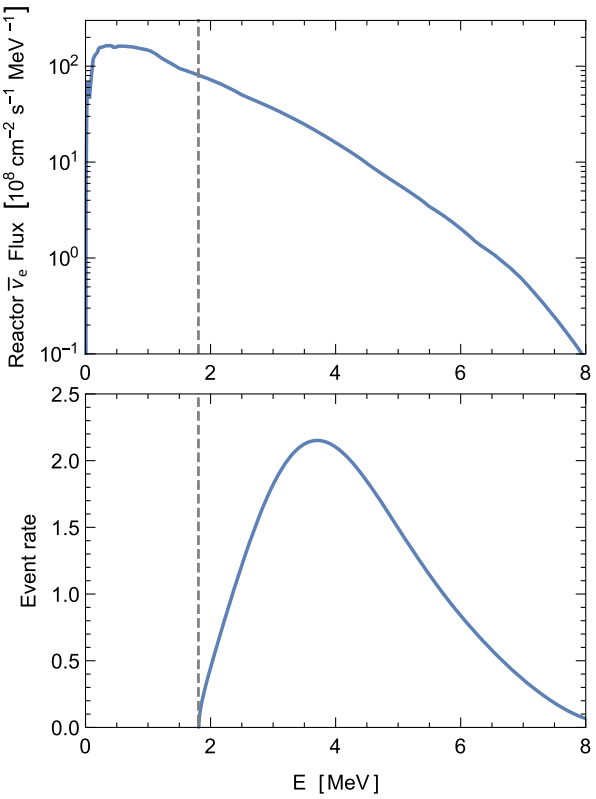

FIG. 16. Typical reactor neutrino spectrum, here from the Japanese experimental fast reactor JOYO (Furuta *et al.*, 2012). Top panel: flux at a distance of 24.3 m. Bottom panel: event rate (arbitrary units) as a function of neutrino energy, i.e., the neutrino energy distribution folded with the interaction cross section for inverse β decay. Only $\bar{\nu}_e$ above the threshold of 1.8 MeV (vertical dashed line) are detectable. The event rate peaks at $E_\nu \sim 4$ MeV.

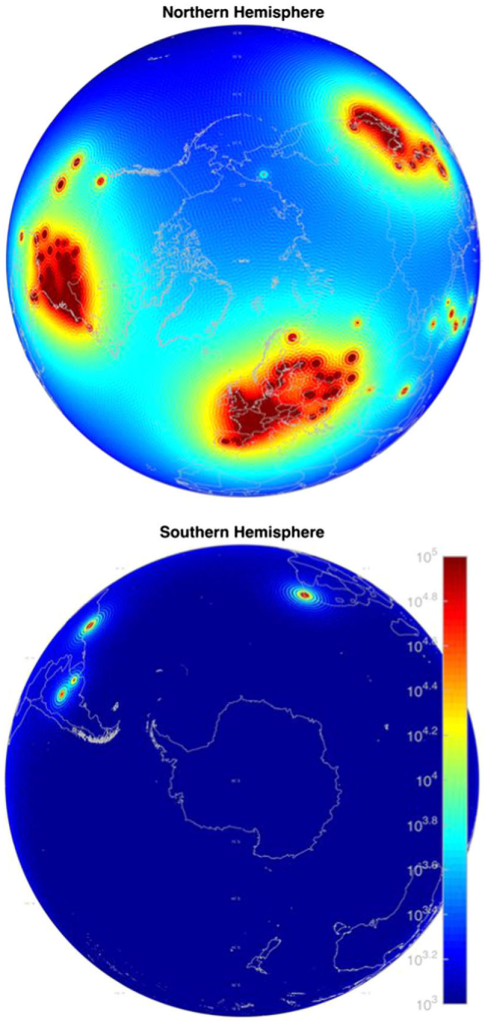

FIG. 17. Global map of the expected $\bar{\nu}_e$ flux (in $1/100$ cm^2/s) in the narrow energy range 3.00–3.01 MeV from all power reactors. Flavor oscillations driven by the "solar" mixing parameters are visible on the 100 km scale. From Usman *et al.*, 2015.

oscillations over 100 km distances. The three main centers of production are the Eastern U.S., Europe, and East Asia, most notably Japan.

B. Measurements

While we have included reactor neutrinos in our discussion of the diffuse neutrino background at Earth, reactors, or clusters of reactors, are typically used as nearby sources to study neutrino properties. Reactor experiments were the first successful attempt to detect the elusive neutrinos. The proposal of using inverse beta decay dates back to Bethe and Peierls (1934), but it was only in 1953 that Reines and Cowan started their experiments at Hanford and Savannah River, which eventually detected neutrinos for the first time (Cowan *et al.*, 1953). Nuclear power plants have been employed to study neutrino properties many times since.

Concerning flavor conversion, a milestone discovery was the detection of $\bar{\nu}_e$ disappearance by KamLAND in 2002 over an approximate distance of 180 km (Eguchi *et al.*, 2003), driven by the solar mixing parameters θ_{12} and δm^2. The subsequent measurement of a spectral distortion (Araki *et al.*, 2005b) gave the first direct evidence for the phenomenon of flavor oscillations with the usual energy dependence. Notice that matter effects here are subdominant, so one is essentially testing vacuum oscillations.

The earlier search over much shorter distances for oscillations driven by the mixing angle θ_{13} and the "atmospheric" mass difference Δm^2 by the CHOOZ (Apollonio *et al.*, 1999) and Palo Verde (Boehm *et al.*, 2001) experiments proved elusive. However, since 2012, a new generation of reactor experiments [Double Chooz (Abe *et al.*, 2012), Daya Bay (An *et al.*, 2012), and RENO (Ahn *et al.*, 2012)] has succeeded in measuring a nonzero value for θ_{13} with high precision.

The frontier of reactor neutrino measurements will be advanced by the JUNO detector (An *et al.*, 2016) that is currently under construction in China. One of the prime goals is to detect subtle three-flavor interference effects at an approximate distance of 60 km to establish the neutrino mass ordering.

Meanwhile, the "reactor antineutrino anomaly" (Mention *et al.*, 2011) remains unsettled, i.e., a few-percent deficit of the measured $\bar{\nu}_e$ flux close to the reactors. Other anomalies include $\bar{\nu}_e$ appearance and ν_e disappearance; see Böser *et al.* (2020) and references therein. One interpretation involves

oscillations to sterile neutrinos driven by an eV-scale mass difference (Conrad and Shaevitz, 2018; Giunti and Lasserre, 2019). Recent antineutrino flux predictions (Estienne *et al.*, 2019; Hayen *et al.*, 2019) have been used to reevaluate the significance of the reactor anomaly; in the ratios of measured antineutrino spectra an anomaly may still persist (Berryman and Huber, 2020).

VIII. SUPERNOVA NEUTRINOS

The core collapse of a massive star within a few seconds releases the gravitational binding energy of a neutron star (NS), $E_{\rm b} \sim 3 \times 10^{53}$ erg, in the form of neutrinos in what is known as a supernova (SN) explosion. This energy release is roughly comparable to that of all stars in the Universe within the same period. While the neutrino burst from the next nearest SN is one of the most cherished targets of neutrino astronomy, it is a transient signal and thus not part of the GUNS. We summarize here the main features of core-collapse neutrino emission primarily as an ingredient for the DSNB presented in Sec. IX. For reviews of SN neutrinos see Janka (2012), Scholberg (2012), Janka, Melson, and Summa (2016), and Mirizzi *et al.* (2016).

A. Generic features of supernova neutrinos

At the end of its life, the compact core of an evolved star becomes unstable and collapses to nuclear density, where the equation of state stiffens (Janka, 2012, 2017; Burrows, 2013). At this core bounce, a shock wave forms, moves outward, and ejects most of the mass in the form of a SN explosion, leaving behind a compact remnant that cools to become a NS. Typical masses are around $M_{\rm NS} \simeq 1.5 M_\odot$, with $2M_\odot$ the largest observed case. The radius is $R_{\rm NS} \simeq 12$–14 km, with the exact value and NS structure depending on the nuclear equation of state. Within these uncertainties one expects the release of the following binding energy:

$$E_{\rm b} \simeq \frac{3}{5}\frac{G_{\rm N} M_{\rm NS}^2}{R_{\rm NS}} \simeq 3 \times 10^{53}\ {\rm erg} \simeq 2 \times 10^{59}\ {\rm MeV}, \qquad (32)$$

with $G_{\rm N}$ Newton's gravitational constant.

This large amount of energy appears in the form of neutrinos because the interaction rate of γ and $e^\pm$ is so large in dense matter that they contribute little to energy transfer, whereas gravitons interact far too weakly to be effective. Moreover, in hot nuclear matter the neutrino mean free path is short compared to the geometric dimension of the collapsed object, so ν and $\bar\nu$ of all flavors thermalize, for example, by nucleon-nucleon bremsstrahlung and other processes (Bruenn, 1985). Hence, approximately we may think of the collapsed SN core as a blackbody source for ν and $\bar\nu$ of all flavors.

The diffusion character of neutrino transport leads to an estimated time of a few seconds for most of the energy trapped in the SN core to escape. The emission temperature depends on radiative transfer in the decoupling region ("neutrino sphere"), typically $T_\nu \simeq 3$–5 MeV, i.e., average energies $\langle E_\nu \rangle = (3/2) T_\nu \simeq 10$–$15$ MeV after neutrino decoupling (Janka, 2012, 2017; Burrows, 2013). This scale is similar to that of solar neutrinos and geoneutrinos, where, however, it is set by nuclear physics. Overall one expects an emission of around $E_{\rm b}/\langle E_\nu \rangle \simeq 3 \times 10^{57}$ particles for each of the six ν and $\bar\nu$ species.

Besides energy, the SN core must also radiate lepton number (deleptonization). The final NS contains only a small proton or electron fraction, whereas the collapsing material, consisting of elements between O and Fe, initially has an electron fraction $Y_e = 0.46$–0.5. A baryonic mass of $1.5 M_\odot$ corresponds to 2×10^{57} nucleons, implying that 1×10^{57} units of electron lepton number must escape in the form of ν_e, ignoring for now flavor conversion. Comparison with the estimated 6×10^{57} of ν_e plus $\bar\nu_e$ to be radiated by the required energy loss reveals a significant excess of ν_e over $\bar\nu_e$ emission (Mirizzi *et al.*, 2016).

The overall picture of neutrino energies and timescale of emission was confirmed on February 23, 1987 by the neutrino burst from SN 1987A in the Large Magellanic Cloud with a total of about two dozen events in three small detectors (Bionta *et al.*, 1987; Hirata *et al.*, 1987; Alekseev *et al.*, 1988). However, the data were too sparse for detailed quantitative tests. The next nearest SN would provide high statistics, especially in Super-Kamiokande, IceCube, or upcoming large detectors such as Hyper-Kamiokande or DUNE. The expected large number of neutrino events in these detectors may show detailed imprints of SN physics (Scholberg, 2018).

B. Reference neutrino signal

The standard paradigm of stellar core collapse and SN explosions has evolved over decades of numerical modeling (Janka, 2012; Janka, Melson, and Summa, 2016), first in spherical symmetry (1D) and over the past years with ever more refined 3D models. After the collapse has begun and when the density exceeds some 10^{12} g cm^{-3}, neutrinos are entrained by the infalling matter because of coherent scattering on large nuclei. When nuclear density of 3×10^{14} g cm^{-3} is reached, the core bounces and a shock wave forms within the core at an enclosed mass of around $0.5 M_\odot$. As the shock propagates outward, it loses energy by dissociating iron and eventually stalls at a radius of some 150 km, while matter keeps falling in. Meanwhile the neutrino flux streaming through this region deposits some of its energy, rejuvenating the shock wave, which finally moves on and ejects the outer layers. It leaves behind a hot and dense proto-neutron star (PNS), which cools and deleptonizes within a few seconds. This is the essence of the neutrino-driven explosion mechanism, also called the delayed explosion mechanism or Bethe-Wilson mechanism (Bethe and Wilson, 1985).

The corresponding neutrino signal falls into three main phases shown in Fig. 18, using a $27 M_\odot$ spherically symmetric model for illustration.[9] As in most simulations, neutrino radiative transfer is treated in a three-species approximation consisting of ν_e, $\bar\nu_e$, and ν_x, which stands for any of ν_μ, $\bar\nu_\mu$, ν_τ, or $\bar\nu_\tau$. This approach captures the main flavor dependence

[9] See the Garching Core-Collapse Supernova Data Archive at https://wwwmpa.mpa-garching.mpg.de/ccsnarchive/ for several suites of SN models.

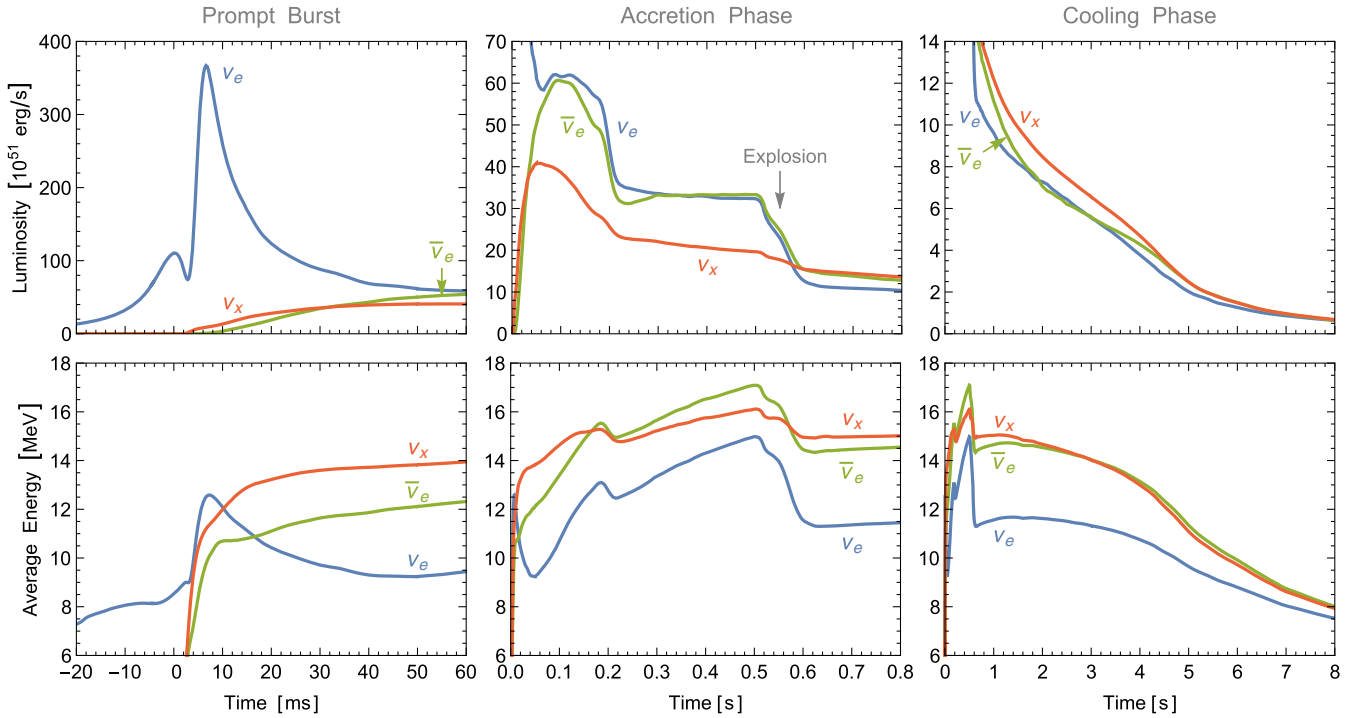

FIG. 18. Luminosities and average energies for ν_e, $\bar{\nu}_e$, and ν_x (representing any of ν_μ, $\bar{\nu}_\mu$, ν_τ, or $\bar{\nu}_\tau$) for the main phases of neutrino emission from a core-collapse SN. Left panels: infall, bounce, and initial shock-wave propagation, including prompt ν_e burst. Middle panels: accretion phase with significant flavor differences of fluxes and spectra. Right panels: cooling of the proto-neutron star (PNS), with only small flavor differences between fluxes and spectra. Based on a spherically symmetric $27M_\odot$ Garching model with explosion triggered by hand over 0.5–0.6 s. It uses the nuclear equation of state of Lattimer and Swesty with nuclear incompressibility modulus $K = 220$ MeV and includes a mixing-length treatment of PNS convection. The final gravitational mass is $1.592M_\odot$ (or 89.6% of the baryonic mass of $1.776M_\odot$), so the mass deficit is $E_b = 0.184\ M_\odot = 3.31 \times 10^{53}$ erg that was lost in neutrinos.

caused by charged-current interactions of the e-flavored states. However, heavy-flavor ν and $\bar{\nu}$ do not interact exactly the same because of recoil corrections and weak magnetism (Horowitz and Pérez-García, 2003). Moreover, the μ- and τ-flavored states differ due to the presence of some muons ($m_\mu = 105.7$ MeV) in matter that reaches temperatures of several tens of MeV (Bollig *et al.*, 2017).

Prompt burst.—Soon after bounce, the shock wave breaks through the edge of the iron core, liberating the conspicuous prompt ν_e burst that corresponds to a significant fraction of the overall lepton number. It is therefore also called the deleptonization or neutronization or breakout burst. During the postbounce time window −20 to 60 ms shown in the left panels in Fig. 18, the SN core radiates about 5% of the total energy that corresponds to the period shown in the rightmost panels, whereas it radiates 0.4×10^{57} units of lepton number, i.e., around 50% of what is emitted over the full period. The features of the prompt-burst phase are thought to be essentially universal (Liebendörfer *et al.*, 2003; Kachelrieß *et al.*, 2005). The small dip in the ν_e luminosity curve at $t = 0$–4 ms, for example, is explained by the shock first compressing matter to opaque conditions before the postshock layer reexpands to become transparent.

Accretion phase.—As the shock wave stalls, neutrino emission is powered by the accretion flow of matter onto the SN core, emitting ν_e and $\bar{\nu}_e$ with almost equal luminosities, but somewhat different average energies, so the ν_e particle flux is some 20% larger than the $\bar{\nu}_e$ one. The production and interaction is mostly by β processes on protons and neutrons. Heavy-flavor ν and $\bar{\nu}$, on the other hand, are produced in pairs and emerge from somewhat deeper layers, with a smaller radiating region and therefore smaller fluxes. Their average energies, however, are similar to that of $\bar{\nu}_e$. The large hierarchy of flavor-dependent average energies that was seen in the often-cited Livermore model (Totani *et al.*, 1998) is not physical (Raffelt, 2001) and is not borne out by present-day simulations. The luminosity drop at around 200 ms represents the infall of the Si/O interface, after which the accretion rate and luminosity become smaller. Over the entire accretion phase, the mass gain and concomitant contraction of the SN core show up in the increasing neutrino energies.

Explosion.—Spherically symmetric numerical models do not explode, except for the smallest-mass progenitors, such as electron-capture supernovae (Kitaura, Janka, and Hillebrandt, 2006), so the duration of the accretion phase, and whether an explosion occurs at all, cannot be inferred from these models. For example, the explosion in the case of Fig. 18 was triggered by hand during the 500–600 ms period. Three-dimensional simulations successfully explode and suggest that the explosion time strongly depends on the SN model and may vary up to few-hundred microseconds relative to what is shown in Fig. 18; see Bollig *et al.* (2017), Summa *et al.* (2018), Vartanyan *et al.* (2019), and Burrows *et al.* (2020). The quenching of accretion strongly reduces the ν_e and $\bar{\nu}_e$

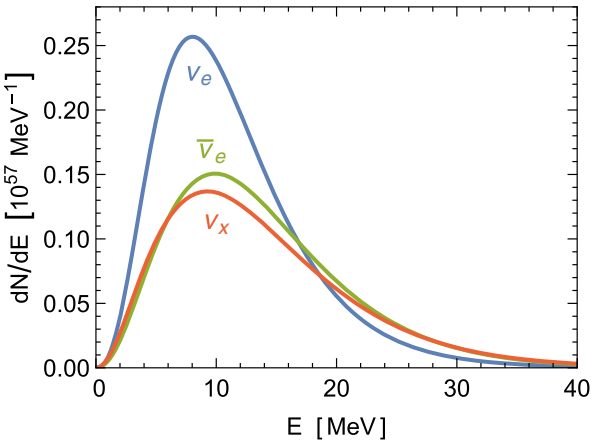

FIG. 19. Time-integrated spectra of the reference model of Fig. 18. The total particle emission is $3.2 \times 10^{57} \nu_e$, $2.4 \times 10^{57} \bar{\nu}_e$, and 2.3×10^{57} for each of ν_μ, $\bar{\nu}_\mu$, ν_τ, and $\bar{\nu}_\tau$.

luminosities that drop to the component provided by core emission.

Cooling.—The remaining evolution consists of cooling and deleptonization of the PNS. The luminosity is essentially equipartitioned among the six species, whereas $\langle E_{\nu_e} \rangle$ is smaller than the others, i.e., there is a net lepton-number flux. The quantitative details depend strongly on the PNS mass and the nuclear equation of state; see Oertel *et al.* (2017) and Nakazato and Suzuki (2019, 2020). Note that we show the neutrino signal until 8 s in Fig. 18, but this is not a hard cutoff. See Nakazato *et al.* (2013) and Nakazato and Suzuki (2020) for discussions of late SN neutrino emission. The neutronization burst and the accretion phase release about 50% of the total energy; the other half is emitted during the cooling phase.

The instantaneous neutrino spectra are quasithermal but do not follow a Fermi-Dirac distribution exactly. Rather they are "pinched"; i.e., the spread of energies around the mean is less than in the thermal case. Phenomenologically, the numerical spectra are well described by a gamma distribution of the form (Keil, Raffelt, and Janka, 2003; Tamborra *et al.*, 2012)

$$f(E) \propto \left(\frac{E}{E_{\rm av}}\right)^{\alpha} \exp\left[-\frac{(\alpha+1)E}{E_{\rm av}}\right], \tag{33}$$

where α is the "pinching parameter," with $\alpha = 2$ corresponding to a Maxwell-Boltzmann distribution. For any α, the parameter $E_{\rm av}$ matches $\langle E \rangle$, whereas α is fixed to match $\langle E^2 \rangle$ of the numerical spectrum by $\langle E^2 \rangle / \langle E \rangle^2 = (2+\alpha)/(1+\alpha)$. In addition, the overall normalization is fixed to match the numerical case. The pinching is largest for ν_e, especially during the prompt burst, and smallest for ν_x.

The time-integrated flux spectra of our reference model are shown in Fig. 19. They are superpositions of pinched spectra with different $E_{\rm av}$, which broadens their spectral shape, and therefore do not need to be pinched themselves. We find the average energies $\langle E_{\nu_e} \rangle = 11.3$ MeV, $\langle E_{\bar{\nu}_e} \rangle = 13.9$ MeV, and $\langle E_{\nu_x} \rangle = 13.8$ MeV, as well as the pinching parameters $\alpha_{\nu_e} = 2.5$, $\alpha_{\bar{\nu}_e} = 2.4$, and $\alpha_{\nu_x} = 2.0$. Thus in this example the integrated spectra follow nearly a Maxwell-Boltzmann distribution.

C. Electron-capture supernovae

Assuming that this scenario captures the main features of a SN neutrino signal, one still expects large case-by-case variations depending on progenitor properties. The lowest-mass SN progenitors [about $(8-10)M_\odot$] become unstable due to electron capture before nuclear burning of their O-Ne-Mg core can be ignited, so they never reach an iron core. These "electron-capture SNe" or "O-Ne-Mg-core SNe" could represent 30% of all cases because the initial mass function decreases rapidly with increasing mass. Spherically symmetric models of these low-mass progenitors explode after a short accretion phase but otherwise resemble what was shown earlier (Fischer *et al.*, 2010; Hüdepohl *et al.*, 2010).

D. Failed explosions

For higher-mass progenitors, numerical models do not explode. It remains open whether successful explosions in supernova simulations depend on quantitative details of neutrino energy transfer and 3D effects or on details of the progenitor models, or whether a crucial piece of input physics is missing. Moreover, probably not all collapsing stellar cores lead to successful explosions, the class of failed SNe, leaving a black hole (BH) instead of a NS as a compact remnant. Using the "compactness parameter" as a criterion, recent theoretical work hints that up to 40% of all collapsing cores may lead to BH formation (O'Connor and Ott, 2011; Ertl *et al.*, 2016; Sukhbold *et al.*, 2016).

The cosmic star-formation rate predicts perhaps twice the observed SNe rate at high redshifts, suggesting a significant fraction of failed explosions (Hopkins and Beacom, 2006; Horiuchi *et al.*, 2011). Likewise, the "red supergiant problem" suggests a cutoff of around 18 $M_\odot$ in the mass range of identified SN progenitors (Smartt *et al.*, 2009; Jennings *et al.*, 2014). A significant fraction of failed SNe would also naturally explain the compact-object mass distribution (Kochanek, 2015). Motivated by these hints, a survey looking for disappearing red supergiants in 27 galaxies within 10 Mpc with the Large Binocular Telescope was created (Adams *et al.*, 2017). Over the first 7 yr, ending in early 2016, this survey found six core-collapse SNe and one candidate for a failed SN, providing $0.14^{+0.33}_{-0.10}$ for the fraction of failed SNe.

In the neutrino signal of a failed SN, the cooling phase would be missing, whereas the accretion phase would abruptly end. The average neutrino energies would increase until this point and the ν_e and $\bar{\nu}_e$ fluxes would dominate (Sumiyoshi *et al.*, 2006; Nakazato *et al.*, 2008; Walk *et al.*, 2020). The overall emitted neutrino energy could exceed that of an exploding SN. The crucial point is that BH formation is delayed, not prompt, so the core bounce and shock scenario is crucial for the expected neutrino burst of both exploding and failed cases.

An intermediate class between exploding and failed progenitors are fallback SNe, where BH formation is delayed if the explosion energy is not sufficient to unbind the star (Fryer, 2009; Wong *et al.*, 2014). Hence, a fraction of the stellar mantle may fall back and push the NS beyond the BH limit.

E. Broken spherical symmetry in the stellar explosion

Observations of SN remnants as well as large NS kick velocities reveal that core-collapse SNe are not spherically symmetric. Recently, numerical simulations without global symmetries (3D simulations) with sophisticated neutrino transport have become available. They show that large-scale convective overturns develop during the accretion phase (Bethe, 1990). Moreover, the neutrino emission properties are also affected by large-scale instabilities, notably the standing accretion shock instability (SASI) (Blondin, Mezzacappa, and DeMarino, 2003; Tamborra *et al.*, 2013), a global sloshing or spiral hydrodynamical oscillation, and the lepton emission self-sustained asymmetry (LESA) (Tamborra *et al.*, 2014), whose effect is that deleptonization mostly occurs in one hemisphere.

For the neutrino signal, these phenomena imply that during the accretion phase the detailed signal properties depend on the observer direction. Moreover, the SASI mode would imprint periodic signal modulations that probably could be picked up with large detectors such as IceCube or Super-Kamiokande. The neutrino signal of the next nearby SN may provide details about the hydrodynamical behavior.

F. Flavor conversion

Numerical SN models treat neutrino transport usually in a three-species formalism consisting of ν_e, $\bar{\nu}_e$, and ν_x, representing any of ν_μ, $\bar{\nu}_\mu$, ν_τ, or $\bar{\nu}_\tau$ and completely ignore flavor conversion. From a numerical perspective, including flavor conversion is completely out of the question. From a theoretical perspective, many questions remain open because the matter effect of neutrinos on each other leads to collective flavor conversion phenomena that are not yet fully understood (Chakraborty *et al.*, 2016; Mirizzi *et al.*, 2016).

The flavor evolution of the prompt ν_e burst is probably similar to MSW conversion of solar neutrinos, except that the starting point is at far larger densities, requiring a three-flavor treatment. Moreover, neutrino-neutrino refraction would cause synchronized oscillations and, depending on the matter profile, cause a spectral split, i.e., a discontinuity in the conversion probability.

During the accretion phase, the $\nu_e\bar{\nu}_e$ flux is larger than the $\nu_\mu\bar{\nu}_\mu$ or $\nu_\tau\bar{\nu}_\tau$ one. Collective effects can lead to pair conversion of the type $\nu_e\bar{\nu}_e \leftrightarrow \nu_\mu\bar{\nu}_\mu$ or $\nu_e\bar{\nu}_e \leftrightarrow \nu_\tau\bar{\nu}_\tau$, i.e., pair annihilation on the level of forward scattering with a rate much faster than the usual nonforward scattering process. Conceivably it could lead to flavor equilibration not far from the neutrino decoupling region (Sawyer, 2016; Izaguirre, Raffelt, and , Tamborra, 2017). In addition to collective effects, one expects MSW conversion by the ordinary matter profile (Dighe and Smirnov, 2000), although the matter effect could be modified by density variations caused by turbulence in the convective regions. Far away from the SN, neutrinos would decohere into mass eigenstates. However, unlike with solar neutrinos, one cannot easily predict the energy-dependent probability for the various ν_i and $\bar{\nu}_i$ components.

G. Detection perspectives

The neutrino signal of SN 1987A on February 23, 1987 in three small detectors was a historical achievement, but the event statistics was sparse (Loredo and Lamb, 2002; Lunardini and Smirnov, 2004; Pagliaroli *et al.*, 2009). The next nearest (probably galactic) SN will be observed in a large number of detectors of different size, ranging from a few events to thousands (Super-Kamiokande) or even millions (IceCube), although in the latter case without event-by-event recognition (Scholberg, 2012; Mirizzi *et al.*, 2016; Scholberg, 2018). The various detectors will provide complementary information. What exactly one will learn depends on the exact type of core-collapse event,which could range from an electron-capture SN to a failed explosion with BH formation. It will also depend on concomitant electromagnetic and possibly gravitational-wave observations.

While the next nearby SN is perhaps the most cherished target of low-energy neutrino astronomy and will provide a bonanza of astrophysical and particle-physics information, its transient nature sets it apart from the general neutrino background. Therefore, a detailed discussion of the detection opportunities is beyond our scope; we refer the interested reader to Mirizzi *et al.* (2016) and Scholberg (2018).

IX. DIFFUSE SUPERNOVA NEUTRINOS

All collapsing stars in the visible Universe, a few per second, provide the DSNB. It dominates at Earth for 10–25 MeV and in the future could be measured by the JUNO and Gd-enriched Super-Kamiokande detectors, providing hints on the SN redshift distribution, the fraction of electromagnetically dim progenitors, and average SN energetics.

A. Basic estimate

The idea that the accumulated neutrinos from all collapsed stars in the Universe form an interesting cosmic background goes back to the early 1980s (Bisnovatyi-Kogan and Seidov, 1982; Domogatskii, 1984; Krauss, Glashow, and Schramm, 1984), while more current reviews were given by Ando and Sato (2004), Beacom (2010), Lunardini (2016), and Mirizzi *et al.* (2016). The DSNB flux and spectrum depend on the overall core-collapse rate, which is uncertain within perhaps a factor of 2 and on the average neutrino emission spectrum. Our baseline case (introduced later) predicts for the sum of all species

$$\Phi_{\Sigma\nu\bar{\nu}} = 126\ \mathrm{cm^{-2}\,s^{-1}}, \tag{34a}$$

$$n_{\Sigma\nu\bar{\nu}} = 4.2\times10^{-9}\ \mathrm{cm^{-3}}, \tag{34b}$$

$$\rho_{\Sigma\nu\bar{\nu}} = 25\ \mathrm{meV\,cm^{-3}}, \tag{34c}$$

with an average energy of 6.0 MeV, corresponding to an emission energy, averaged over all species, of 12.8 MeV. The DSNB energy density is almost the same as the CNB energy density of massless neutrinos that was given, for a single flavor, in Eq. (9). If the lightest neutrino mass is so large that all CNB neutrinos are dark matter today, the DSNB is the dominant neutrino radiation density in the present-day Universe.

We can compare the DSNB with the accumulated photons from all stars, the extragalactic background light (EBL), which provides a radiation density of around 50 $\mathrm{nW\,m^{-2}\,sr^{-1}}$

(Dole *et al.*, 2006). Integrating over directions yields a flux of 400 MeV cm^{-2} s^{-1} and thus an energy density of 13 meV cm^{-3}. Photons and neutrinos are redshifted in the same way, so the stars of the Universe have emitted about twice as much energy in the form of core-collapse neutrinos as in the form of light.

We can express the time-averaged neutrino luminosity L_ν of a given stellar population in units of the number of core-collapse events per unit time, assuming one event releases 2.5×10^{53} erg. Moreover, we can express the photon luminosity L_γ in units of the solar luminosity of $L_\odot = 4\times10^{33}$ erg/s, so a ratio $L_\nu/L_\gamma = 2$ corresponds to $1/100$ yr$/10^{10}L_\odot$ core-collapse events. This rate corresponds approximately to the usual SN unit, which is defined as 1 SNu = 1 SN$/(10^{10}L_{\odot\mathrm{B}}/100$ yr), with $L_{\odot\mathrm{B}}$ the solar luminosity in the blue spectral band. While the SN rate depends strongly on galaxy type, e.g., no core-collapse SNe in elliptical galaxies where no star formation takes place, averaged over all galaxies it is around 1 SNu (Cappellaro, Evans, and Turatto, 1999; Cappellaro and Turatto, 2001). Approximately, 1 SNu corresponds to one SN per century per galaxy. In other words, $L_\nu/L_\gamma\sim2$ of an average stellar population corresponds to the usual astronomical measure of the SN rate. Within uncertainties, the DSNB density of Eq. (34c) follows from expressing 1 SNu as a neutrino-to-photon luminosity ratio.

For DSNB detection, the $\bar\nu_e$ component is of particular interest. For energies below 10 MeV it is hidden under the reactor $\bar\nu_e$ background, so the higher-energy part of the DSNB spectrum is particularly important. It requires a more detailed discussion than a simple prediction of the overall DSNB density.

B. Redshift integral

The DSNB depends on the core-collapse rate $R_{\rm cc}(z)$ at cosmic redshift z and the average spectrum $F_\nu(E) = dN_\nu/dE$ emitted per such event, where ν can be any of the six species of neutrinos or antineutrinos. The long propagation distance implies loss of flavor coherence, so each ν represents a mass eigenstate. Each neutrino burst lasts for a few seconds, but this time structure plays no practical role because one will need to integrate for several years to detect even a small number of DSNB neutrinos. Moreover, the bursts sweeping through the detector somewhat overlap. Therefore, $F_\nu(E)$ is the average time-integrated number of neutrinos per energy interval emitted by a collapsing star.

The neutrino density spectrum accumulated from all cosmic epochs is given by the redshift integral

$$\frac{dn_\nu}{dE} = \int_0^\infty dz(z+1)F_\nu(E_z)n'_{\rm cc}(z), \tag{35}$$

to be multiplied by the speed of light to obtain the diffuse flux; see Appendix A. Here $E_z = (1+z)E$ is the blueshifted energy at emission of the detected energy E. The first factor $1+z$ arises as a Jacobian $dE_z/dE = 1+z$ between the emitted and detected energy intervals. It is assumed that the average neutrino flux spectrum $F_\nu(E)$ is the same at all cosmic epochs.

Finally $n'_{\rm cc}(z) = dn_{\rm cc}/dz$ is the core-collapse number per comoving volume per redshift interval. It is usually expressed in the form

$$n'_{\rm cc}(z) = \frac{R_{\rm cc}(z)}{H_0(1+z)\sqrt{\Omega_{\rm M}(1+z)^3+\Omega_\Lambda}}, \tag{36}$$

where H_0 is the Hubble expansion parameter, while $\Omega_{\rm M}$ and Ω_Λ are the present-day cosmic matter and dark-energy fractions. In the literature one usually finds $R_{\rm cc}(z)$, the number of core-collapse events per comoving volume per unit time (units Mpc^{-3} yr^{-1}). However, $R_{\rm cc}(z)$ is derived in terms of an assumed cosmological model because observations for a given redshift interval need to be translated to intervals of cosmic time; i.e., only $n'_{\rm cc}(z)$ has direct meaning. Thus a given $R_{\rm cc}(z)$ makes sense only in conjunction with the assumed underlying cosmological model.

We may further express $n'_{\rm cc}(z) = n_{\rm cc}f_{\rm cc}(z)$ in terms of the comoving density $n_{\rm cc}$ of all past core-collapse events times its normalized redshift distribution with $\int_0^\infty dzf_{\rm cc}(z) = 1$. Likewise, the neutrino emission spectrum is expressed as $F_\nu(E) = N_\nu f_\nu(E)$, with N_ν the total number of species ν emitted by an average core collapse times its normalized spectrum with $\int_0^\infty dEf_\nu(E) = 1$. With these definitions, Eq. (35) is

$$\frac{dn_\nu}{dE} = N_\nu n_{\rm cc}g_\nu(E), \tag{37}$$

with the energy spectrum of the accumulated neutrinos

$$g_\nu(E) = \int_0^\infty dz(z+1)f_\nu[(z+1)E]f_{\rm cc}(z). \tag{38}$$

It fulfills the normalization $\int_0^\infty dEg_\nu(E) = 1$ if $f_\nu(E)$ and $f_{\rm cc}(z)$ are normalized.

C. Cosmic core-collapse rate

The core-collapse rate as a function of redshift can be determined by direct SN observations. However, this approach may be significantly incomplete because core-collapse SNe can be electromagnetically dim or, for nonexploding cases, completely invisible. Therefore, usually one estimates the rate from the star-formation activity, essentially translating ultraviolet and infrared astronomical observations into a neutrino emission rate. The star-formation rate (mass processed into stars per comoving volume per time interval) as a function of redshift determined by different researchers is shown in Fig. 20. In keeping with previous DSNB studies we use the star-formation rate of Yüksel *et al.* (2008) as our reference case (red solid line). A similar representation, including an explicit allowed range, was provided by Mathews *et al.* (2014), shown as a gray long dashed line and shaded region. These rates considerably increase from the present to $z\sim1$, then level off to form a plateau, and decrease at larger redshift. Following these researchers we use the somewhat schematic cosmological parameters $H_0 = 70$ kms^{-1} Mpc^{-1} $= (13.9\,\mathrm{Gyr})^{-1}$, $\Omega_{\rm M} = 0.3$,

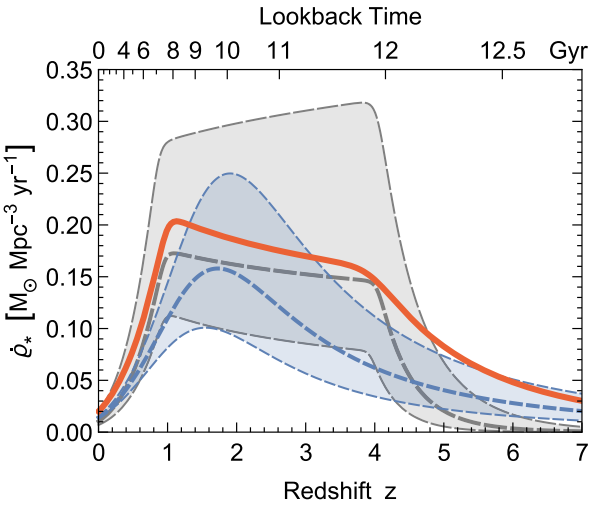

FIG. 20. Cosmic star-formation rate. Red solid line: best fit of Yüksel *et al.* (2008), which we use as our reference case. Gray long dashed lines: best fit and allowed range of Mathews *et al.* (2014). Blue short dashed lines: best fit and allowed range of Robertson *et al.* (2015). All of these researchers provided analytic fit functions that were used here.

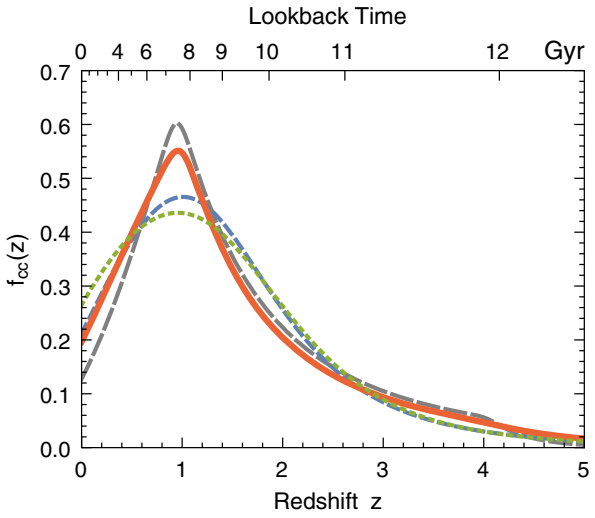

FIG. 21. Normalized core-collapse distribution as a function of redshift for the best-fit cases of Fig. 20 and in addition that of Madau and Dickinson (2014) in green (dotted line).

and $\Omega_\Lambda = 0.7$. A different form and allowed range was provided by Robertson *et al.* (2015), here shown as a blue short dashed line and shaded region. They used a somewhat different cosmological model, which we have transformed to our reference parameters. These results are similar to those provided by Madau and Dickinson (2014), which we do not show in Fig. 20.

To convert the star-formation rate into a core-collapse rate $R_{cc} = k_{cc}\dot{\varrho}_*$ we need the factor

$$k_{cc} = \frac{\int_{M_{min}}^{M_{max}} dM\psi(M)}{\int_{M_l}^{M_u} dM\, M\psi(M)} = (135\ M_\odot)^{-1}, \tag{39}$$

where $\psi(M) \propto M^{-2.35}$ is the Salpeter initial mass function (Salpeter, 1955) and $(M_l, M_u) = (0.1, 125)M_\odot$ is the overall stellar mass range. For stars that develop collapsing cores we use $(M_{min}, M_{max}) = (8, 125)M_\odot$, including those cases that do not explode as a SN but rather form a BH because these nonexploding cases are also powerful neutrino sources.

With this conversion factor we find for the integrated core-collapse density n_{cc} of the past cosmic history for the best-fit star-formation rates of the aforementioned researchers

$$\begin{aligned} &1.05 \times 10^7\ \text{Mpc}^{-3}\ [497],\\ &0.84 \times 10^7\ \text{Mpc}^{-3}\ [349],\\ &0.69 \times 10^7\ \text{Mpc}^{-3}\ [424],\\ &0.58 \times 10^7\ \text{Mpc}^{-3}\ [344]. \end{aligned} \tag{40}$$

If every core collapse emits on average $N_\nu \sim 2 \times 10^{57}$ neutrinos of each species, $n_{cc} \sim 10^7$ Mpc^{-3} yields a DSNB density in one species of $n_\nu \sim 2 \times 10^{64}$ Mpc^{-3} $= 0.7 \times 10^{-9}$ cm^{-3} or, after multiplying by the speed of light, an isotropic flux of 20 cm^{-2} s^{-1} in one species.

We show the normalized redshift distributions $f_{cc}(z)$ in Fig. 21. After convolution with the SN emission spectrum they yield similar neutrino distributions. To illustrate this point we assume a Maxwell-Boltzmann distribution $f_\nu(E) = (E^2/2T^2)e^{-E/T}$ for the time-integrated SN emission spectrum; see Sec. VIII.B. In this case the fiducial redshift distribution produces the DSNB spectrum shown in the top panel of Fig. 22. The other redshift distributions produce similar spectra, so we show the fractional difference to the reference case (Fig. 22, middle panel). The detection interval is 10–25 MeV, so for $T \sim 4$ MeV this corresponds to roughly 2–6 on the horizontal axis of Fig. 22. At the lower end of this interval, where the detectable flux is largest, the differences are extremely small, but up to 30% at the upper end for the Mathews *et al.* (2014) case. Even though the star-formation history looks quite different for the red and blue cases, the final DSNB spectrum is nearly the same.

Overall the DSNB spectrum is fairly insensitive to the exact redshift distribution $f_{cc}(z)$. In keeping with previous studies we use the distribution provided by Yüksel *et al.* (2008) as a fiducial case that is shown as a red line in the figures of this section.

In the bottom panel of Fig. 22 we show the average redshift contributing to the DSNB spectrum (only for our fiducial case) at a given energy. Even at the lower end of the detection interval, $\langle z \rangle$ is less than 1, and significantly smaller at higher energies. Therefore, the main contribution comes from relatively low redshifts.

The DSNB derived from a Maxwell-Boltzmann source spectrum is strongly antipinched (average energy for our fiducial case $\langle E \rangle = 1.41T$ and pinching parameter 0.84) and not well represented by a gamma distribution of the form of Eq. (33). However, one finds that the decreasing part of the spectrum is close to an exponential $e^{-E/T}$ and a good overall fit to the fiducial case is

$$g_\nu(E/T) = 1.15 \arctan[3(E/T)^{3/2}]e^{-1.03E/T}. \tag{41}$$

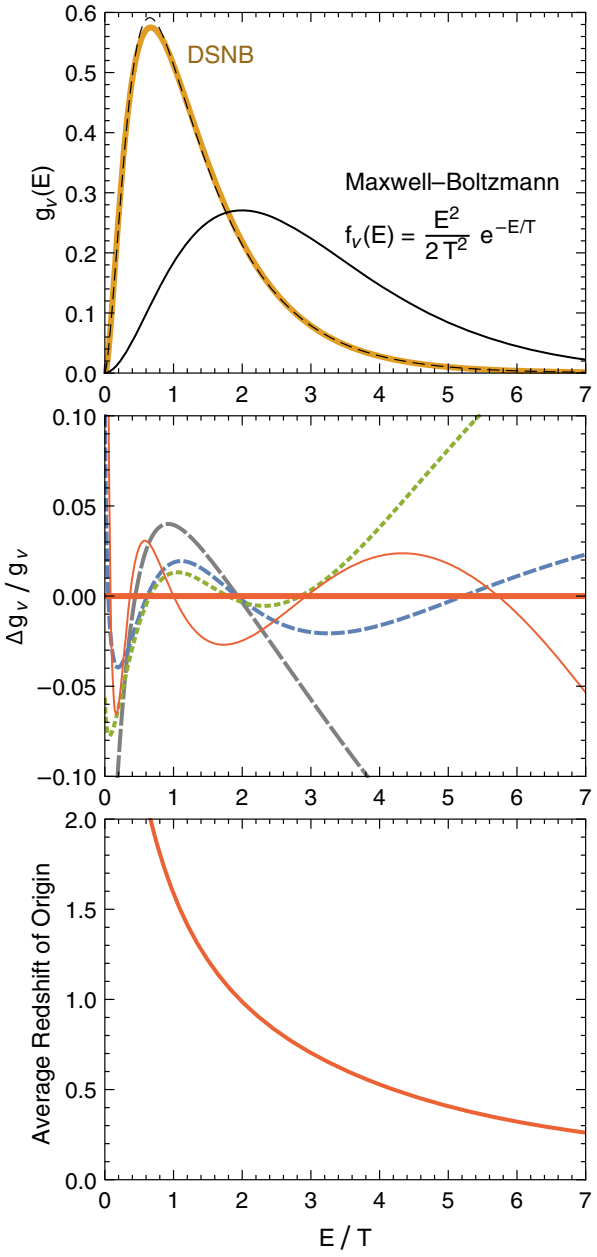

FIG. 22. Spectral properties of the DSNB. Top panel: Maxwell-Boltzmann source spectrum with temperature T (black) and corresponding DSNB spectrum (orange) for our fiducial redshift distribution of Yüksel *et al.* (2008). The dashed line is the fit function of Eq. (41); the fractional deviation is the red thin solid line the next panel. Middle panel: fractional difference of the Mathews *et al.* (2014) case (gray long dashed line), the Robertson *et al.* (2015) case (blue short dashed line), and the Madau and Dickinson (2014) case (green dotted line) to the fiducial spectrum (red thick solid line). Bottom panel: average of the source redshift for the fiducial case.

The deviation of this fit from our fiducial spectrum is shown in the middle panel of Fig. 22 as a thin red line. The deviation is smaller than the spread of different cases of star-formation histories.

The main uncertainty of the DSNB prediction is the total number of core-collapse events shown in Eq. (40). Moreover, these predictions involve an overall uncertainty in converting the star-formation rate into a core-collapse rate (the factor $k_{\rm cc}$). A mismatch of about a factor of 2 between direct SN observations and the core-collapse rate estimated from star formation was found, the so-called SN-rate problem (Horiuchi *et al.*, 2011). The most likely explanation is dust extinction, especially at higher redshift, or a relatively large fraction of dim SNe, and, in particular, of nonexploding, BH-forming cases (Horiuchi *et al.*, 2011, 2014; Adams *et al.*, 2013; Kochanek, 2014).

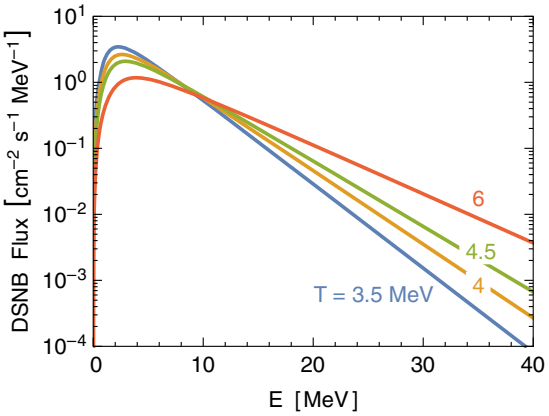

FIG. 23. DSNB flux in one species according to Eq. (42). The emission spectrum is taken to be a Maxwell-Boltzmann one with the indicated temperatures.

D. Average emission spectrum

The sparse data of SN 1987A are not detailed enough to give a good estimate of the neutrino spectrum and also need not be representative of the average case. Therefore, DSNB predictions depend on numerical SN models. To get a first impression we assume that the time-integrated spectrum is of the Maxwell-Boltzmann type. With Eq. (37) the DSNB flux for a given species ν is

$$\frac{d\Phi_\nu}{dE} = 4.45\ \mathrm{cm^{-2}\,s^{-1}\,MeV^{-1}}\,\frac{n_{\rm cc}}{10^7\ \mathrm{Mpc^{-3}}} \times \frac{6E_\nu^{\rm tot}}{2\times 10^{53}\ \mathrm{erg}}\left(\frac{4\ \mathrm{MeV}}{T}\right)^2 g_\nu(E/T), \qquad (42)$$

where $E_\nu^{\rm tot}$ is the total emitted energy in the considered species ν and $g_\nu(E/T)$ is the normalized spectrum of Eq. (41) that includes our fiducial redshift distribution. We show this spectrum for $T = 3.5$, 4, 4.5, and 6 MeV in Fig. 23, where values of around 4 MeV would be typical for a core-collapse SN, whereas 6 MeV could represent a BH-forming event with larger spectral energies.

We conclude that around the detection threshold of 10 MeV, the flux predictions are similar and depend primarily on the overall normalization, i.e., the cosmic core-collapse rate and the average energy release. For larger E, the spectra scale essentially as $e^{-E/T}$ and thus depend strongly on the effective emission temperature. Therefore, the flux at the upper end of the detection window (~20 MeV) is particularly sensitive to the fraction of BH-forming events (Nakazato *et al.*, 2008;

Lunardini, 2009; Priya and Lunardini, 2017; Møller *et al.*, 2018; Schilbach, Caballero, and McLaughlin, 2019).

More recent and sophisticated predictions synthesize the average emission spectrum from a suite of numerical SN models (Nakazato *et al.*, 2015; Horiuchi *et al.*, 2018; Møller *et al.*, 2018). Note that the high-energy tail of the DSNB spectrum is higher in these papers than what was adopted in the Super-Kamiokande analysis (Bays *et al.*, 2012), which was based on simplified modeling of the SN population and relied on older and more approximate SN models. For illustration, we here follow Møller *et al.* (2018) and consider three components, a $9.6M_\odot$ progenitor model, representing the range $(8-15)M_\odot$ including electron-capture SNe, a $27M_\odot$ model, representing the higher-mass exploding cases, and a $40M_\odot$ nonexploding case called "slow BH formation" by Møller *et al.* (2018). Using a Salpeter initial mass function, the $(8\text{–}15)M_\odot$ range encompasses 59% of all collapsing stars. The minimal prediction further assumes that the $(15\text{–}40)M_\odot$ progenitors (32%) explode, and all progenitors with larger masses (9%) follow the slow-BH case. The fiducial case of Møller *et al.* (2018) assumes a larger fraction of 21% of BH formation, whereas an extreme case would be with 41% such cases, leaving only the $(8\text{–}15)M_\odot$ range to explode.

We show the main characteristics of these spectral components in Table IV. The exploding models use four-species neutrino transport and thus provide separate emission spectra for ν_e, $\bar{\nu}_e$, ν_x, and $\bar{\nu}_x$. For each model and each species we show the total number of emitted particles N_ν, the emitted energy $E_\nu^{\rm tot}$, and the average neutrino energy $E_{\rm av}$ and pinching parameter α of the time-integrated spectrum. The overall emitted energy is $E_{\rm tot} = E_{\nu_e}^{\rm tot} + E_{\bar{\nu}_e}^{\rm tot} + 2E_{\nu_x}^{\rm tot} + 2E_{\bar{\nu}_x}^{\rm tot}$. We convolve these emission spectra with our fiducial redshift distribution, which does not change N_ν but instead only the spectral shape. Inspired by Eq. (41), we approximate the spectra by fit functions of the form

$$g_\nu(E) = \frac{a}{T}\arctan\left[b\left(\frac{E}{T}\right)^q\right]\exp\left[-\left(\frac{E}{T}\right)^p\right], \tag{43}$$

where the global factor a is constrained by normalization $\int_0^\infty dE g_\nu(E) = 1$. In the measurement region $E \gtrsim 10$ MeV, the spectrum scales as $\exp[-(E/T)^p]$, with $p \sim 1$. The fit parameter T sets the energy scale and is one way of defining an effective temperature for the nonthermal emission spectrum. For a given species ν, the DSNB flux is

$$\frac{d\Phi_\nu}{dE} = \frac{10.3}{\rm cm^2\,s\,MeV}\frac{n_{\rm cc}}{10^7\ {\rm Mpc}^{-3}}\frac{N_\nu}{10^{57}}\,g_\nu(E), \tag{44}$$

where the parameter T is assumed to be in units of MeV. These fits represent the numerical spectra to better than a few percent, especially in the detection region. The fractional deviation always looks similar to the dashed red line in the middle panel of Fig. 22.

We show the DSNB fluxes for each species in Fig. 24 for each core-collapse model as if the entire DSNB were caused by only one of them. The higher-mass models, with a longer period of accretion, have hotter spectra, especially the BH-forming case. For the exploding cases, the x spectra provide larger fluxes at high energies than the e-flavored ones, whereas for the BH case it is the opposite because the long accretion period produces larger fluxes of ν_e and $\bar{\nu}_e$ than of the other species.

In Fig. 25 we show DSNB fluxes based on the minimal case of Møller *et al.* (2018) with a mixture of 59%, 32%, and 9% of the $9.6M_\odot$, $27M_\odot$, and $40M_\odot$ models (red) and their fiducial case with 59%, 20%, and 21% (gray). The mixed cases show a much smaller spread between the flavor-dependent spectra (solid versus dashed lines). This effect is partly owed to the inverted flavor dependence between the exploding and nonexploding models. Moreover, near the detection threshold of

TABLE IV. Characteristics of the time-integrated neutrino emission of the core-collapse models used to synthesize our illustrative DSNB example; for details see Møller *et al.* (2018). For each species ν we give the total number of emitted particles N_ν, the emitted energy $E_\nu^{\rm tot}$, the average energy $E_{\rm av}$, the pinching parameter α, and $E_{\rm av}^{\rm DSNB}$ after convolution with our fiducial redshift distribution. The remaining parameters determine the fit function of Eq. (43) for the normalized DSNB spectrum.

		N_ν 10^{57}	$E_\nu^{\rm tot}$ 10^{52} erg	$E_{\rm av}$ (MeV)	α	$E_{\rm av}^{\rm DSNB}$ (MeV)	a	b	q	p	T (MeV)
9.6 $M_\odot$ (SN)	ν_e	2.01	3.17	9.8	2.81	4.59	1.347	1.837	1.837	0.990	2.793
	$\bar{\nu}_e$	1.47	2.93	12.4	2.51	5.83	1.313	1.770	1.703	0.969	3.483
	ν_x	1.61	3.09	12.0	2.10	5.62	1.173	2.350	1.672	0.953	3.432
	$\bar{\nu}_x$	1.61	3.27	12.7	1.96	5.95	1.145	2.401	1.620	0.944	3.617
27 $M_\odot$ (SN)	ν_e	3.33	5.87	11.0	2.17	5.16	1.575	0.489	1.775	0.794	1.824
	$\bar{\nu}_e$	2.61	5.72	13.7	2.25	6.41	1.260	1.791	1.667	0.942	3.700
	ν_x	2.56	5.21	12.7	1.88	5.95	1.153	2.106	1.615	0.916	3.400
	$\bar{\nu}_x$	2.56	5.53	13.5	1.76	6.32	1.111	2.337	1.569	0.916	3.690
40 $M_\odot$ (BH)	ν_e	3.62	9.25	16.0	1.66	7.47	1.065	2.340	1.809	0.866	3.904
	$\bar{\nu}_e$	2.88	8.61	18.7	1.99	8.75	1.089	3.199	1.801	0.951	5.486
	ν_x, $\bar{\nu}_x$	1.72	4.83	17.5	1.46	8.21	1.227	1.090	1.314	0.822	3.707
Mix 1	$\langle\nu\rangle$	2.14	4.14	12.1	1.74	5.66	1.471	0.356	1.755	0.724	1.592
(59,32,9)	$\langle\bar{\nu}\rangle$	1.94	4.20	13.5	1.80	6.34	1.308	0.940	1.614	0.822	2.687
Mix 2	$\langle\nu\rangle$	2.09	4.25	12.7	1.52	5.95	1.362	0.318	1.768	0.690	1.486
(59,20,21)	$\langle\bar{\nu}\rangle$	1.88	4.26	14.2	1.64	6.63	1.301	0.734	1.617	0.777	2.439

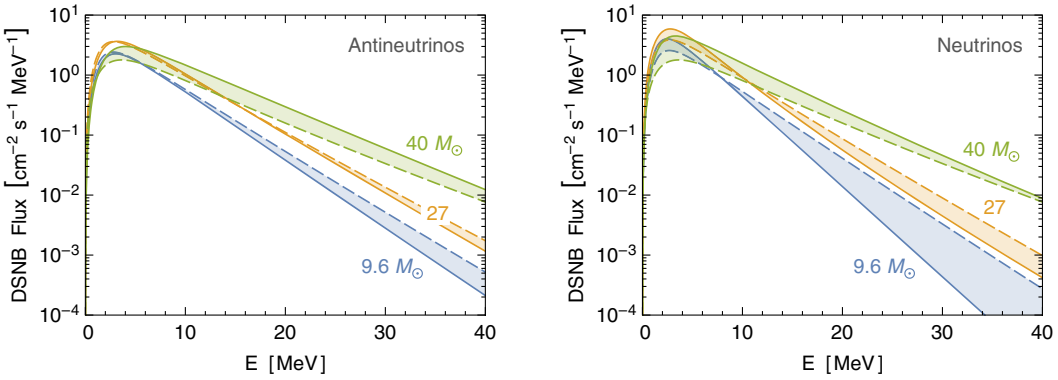

FIG. 24. DSNB flux for the $9.6M_\odot$, $27M_\odot$, and $40M_\odot$ core-collapse models described in the text, where the actual flux would be a superposition of these reference cases. For each neutrino species, the flux is given by Eq. (44) with the parameters of Table IV. Solid lines are for ν_e or $\bar{\nu}_e$ and dashed lines are for ν_x or $\bar{\nu}_x$, so the flux for each mass eigenstate is a superposition of solid and dashed spectra, i.e., in the shaded bands, depending on flavor evolution upon leaving the source.

around 10 MeV, the exact mix leaves the DSNB prediction nearly unchanged.

E. Flavor Conversion

Neutrinos are produced with flavor-dependent fluxes and spectra so that flavor conversion on the way from the decoupling region modifies the escaping flavor composition, or rather the final mix of mass eigenstates. Moreover, the way in which this effect is relevant depends on the detection method. As argued in Sec. VIII.F, SN neutrino flavor conversion is not yet fully understood, so by the current state of the art there is no reliable prediction. On the other hand, flavor conversion would be a small effect on the overall DSNB prediction as seen in Fig. 25, where the difference between the dashed and solid lines is quite small, especially near the detection threshold of 10 MeV where most events would be measured.

Therefore, as a baseline prediction we use fluxes that are flavor averages of the form $\Phi_{\langle\nu\rangle} = (\Phi_{\nu_e} + 2\Phi_{\nu_x})/3$. We show the spectral characteristics for our two illustrative mixtures in Table IV. For our minimal mix 1, we find the total DSNB flux, number density, and energy density at Earth of neutrinos plus antineutrinos of all flavors that were shown in Eq. (34). Concerning normalization, the main uncertainty is the overall core-collapse rate. Concerning the spectral shape, the main uncertainty is the fraction of BH-forming cases.

F. Detection perspectives

The DSNB has not yet been detected, but restrictive upper limits exist that are shown in Fig. 26. They were obtained by the Super-Kamiokande (SK) I, II, and III water Cherenkov detector (Bays *et al.*, 2012), SK IV with neutron tagging (Zhang *et al.*, 2015), and the KamLAND liquid-scintillator detector (Gando *et al.*, 2012). All of these limits are based on the inverse beta-decay reaction $\bar{\nu}_e + p \to n + e^+$. These limits do not yet reach the predictions, but keeping in mind that the cosmic core-collapse rate and its BH-forming component could be larger than assumed here means that any significant experimental improvement could lead to a detection.

DSNB detection is a question not only of event rate but of identification and rejection of several backgrounds that can mimic DSNB events. A first detection should become possible over the next decade with the upcoming Gd-enhanced Super-Kamiokande water Cherenkov detector (Beacom and Vagins, 2004; Labarga, 2018) and later with a possible Gd-enhanced version of the upcoming Hyper-Kamiokande (Abe *et al.*, 2018). Another promising contender is the upcoming JUNO 20 kt scintillator detector (An *et al.*, 2016). A complementary detection channel, using the ν_e flux, may be offered by the upcoming liquid argon detector DUNE at the LBNF facility in the U.S. (Acciarri *et al.*, 2016; Cocco *et al.*, 2004). A detailed forecast of these opportunities is beyond the scope of our discussion.

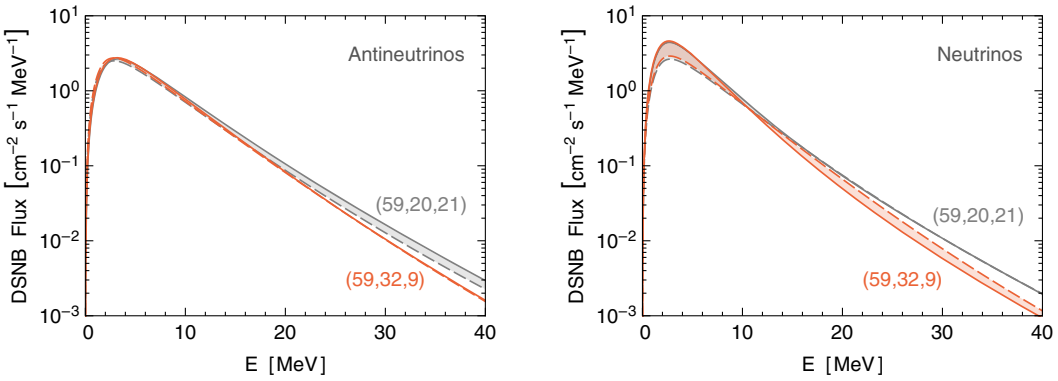

FIG. 25. DSNB flux for the two indicated mixes of the $9.6M_\odot$, $27M_\odot$, and $40M_\odot$ source models.

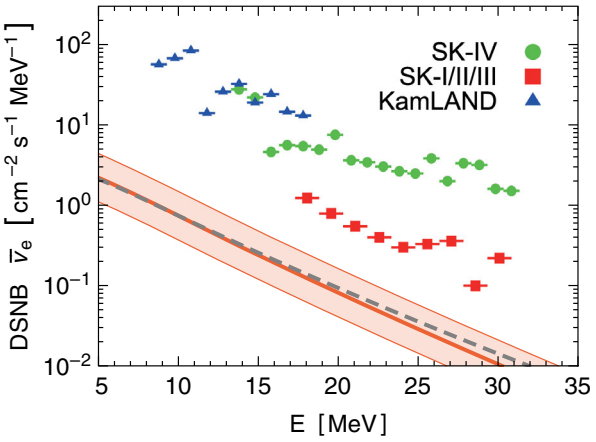

FIG. 26. Experimental limits on the $\bar{\nu}_e$ component of the DSNB by Super-Kamiokande (SK) I, II, and III (Bays *et al.*, 2012), SK IV (Zhang *et al.*, 2015), and KamLAND (Gando *et al.*, 2012). The fiducial predicted flux is mix 1 (red solid line) with an adopted normalization uncertainty of a factor of 2 in either direction (shaded band). We also show mix 2 (gray dashed line), which includes a larger fraction of BH-forming cases. Adapted from Nakazato *et al.*, 2015.

X. ATMOSPHERIC NEUTRINOS

Atmospheric neutrinos are produced by cosmic rays interacting with the atmosphere of Earth or the Sun (Seckel, Stanev, and Gaisser, 1991; Ingelman and Thunman, 1996; Gaisser, Engel, and Resconi, 2016; Argüelles *et al.*, 2017; Edsjö *et al.*, 2017; Ng *et al.*, 2017). Historically, they were the first "natural neutrinos" to be detected (Achar *et al.*, 1965; Reines *et al.*, 1965) and later played a fundamental role in establishing flavor oscillations by the Super-Kamiokande water Cherenkov detector (Fukuda *et al.*, 1998). Nowadays, atmospheric neutrinos are employed to measure the neutrino mass and mixing parameters with high precision, while, on the other hand, they are a background to the detection of astrophysical neutrinos.

A. Cosmic rays

Charged particles like electrons, protons, and heavier nuclei are accelerated within cosmic reservoirs or on their way to Earth in the presence of astrophysical shocks and magnetic turbulence. These particles constitute the cosmic-ray flux. It further interacts with Earth's atmosphere, producing a secondary particle flux that includes neutrinos. The origin of cosmic rays as well as their composition (the fraction of heavy nuclei and protons) remains subject of vivid debate. The correspondent neutrino flux depends on the cosmic-ray composition, the scattering cross section with the atmosphere as well as radiative losses, and the branching ratios of the by-products.

Comparing the cosmic-ray composition with the chemical composition of the Solar System reveals interesting differences (Gaisser, Engel, and Resconi, 2016). One is that the relative contribution of heavy nuclei with respect to hydrogen is larger in cosmic rays (Wang *et al.*, 2002; Lodders, 2003; de Nolfo *et al.*, 2006; George *et al.*, 2009; Dartois *et al.*, 2015). This could be due to the relative greater ionization energy of hydrogen compared to heavy elements; in fact only ionized or charged particles can be accelerated. An additional, straightforward reason could be a difference in the source composition itself (Cassé, Goret, and Cesarsky, 1975). Finally, for volatile elements, it is possible that this could be due to a mass-to-charge dependence of the acceleration efficiency, with heavier ions being more favorably accelerated (Meyer, Drury, and Ellison, 1997). Another striking difference is that two groups of elements (Li, Be, and B is one; Sc, Ti, V, Cr, and Mn the other) are more abundant in cosmic rays. This is because they are produced in spallation processes (scattering of cosmic rays in the interstellar medium) instead of stellar nucleosynthesis (Tanabashi *et al.*, 2018).

Turning to the energy distribution, above 10 GeV a good approximation to the differential spectrum per nucleon is given by an inverse power law of the form

$$\frac{dN_N}{dE} \propto E^{-(\gamma+1)}, \tag{45}$$

where $\gamma \approx 1.7$ up to around 3×10^6 GeV, e.g., $\gamma_{\text{proton}} = 1.71 \pm 0.05$ (Gaisser, Engel, and Resconi, 2016), and $\gamma \approx 2.0$ at larger energies. This spectral break is known as the knee of the cosmic-ray flux. A second break, known as second knee, is near 10^8 GeV. Near 3×10^9 GeV there is another break known as the ankle. Including the normalization given in Tanabashi *et al.* (2018), the spectrum between several GeV and 100 TeV is

$$\frac{dN_N}{dE} = \frac{1.8 \times 10^4}{(\text{GeV/nucleon})\,\text{m}^2\,\text{s}\,\text{sr}} \left(\frac{E}{\text{GeV/nucleon}}\right)^{-(\gamma+1)}. \tag{46}$$

Below 10 GeV, all cosmic-ray spectra show "solar modulation" (Gleeson and Axford, 1968; Strauss *et al.*, 2012; Maccione, 2013; Cholis, Hooper, and Linden, 2016), a time variation caused by the solar wind, a low-energy plasma of electrons and protons ejected by the Sun with its 11 yr cycle. The shieldlike effect of the solar activity translates to an anticorrelation between the latter and cosmic-ray spectra. Moreover, low-energy particles entering the atmosphere also suffer geomagnetic effects. Therefore, low-energy secondary particle fluxes, including neutrinos, depend on both location and time.

B. Conventional neutrinos

Cosmic rays entering the atmosphere scatter and produce secondary particles, especially charged or neutral pions and kaons, which in turn decay and produce the "conventional neutrinos" (Stanev, 2004) as a main contribution at low energies. The detailed decay chains are[10]

$$\begin{aligned} \pi^\pm &\to \mu^\pm + \nu_\mu(\bar{\nu}_\mu) \\ &\downarrow \\ e^\pm + \nu_e(\bar{\nu}_e) + \bar{\nu}_\mu(\nu_\mu), \end{aligned} \tag{47}$$

[10]More details on the decay channels and their branching ratios were given by Olive *et al.* (2014) and Tanabashi *et al.* (2018).

$$K^{\pm} \to \mu^{\pm} + \nu_{\mu}(\bar{\nu}_{\mu}). \tag{48}$$

Three-body decays of kaons also occur, for example,

$$K^{\pm} \to \pi^0 + e^{\pm} + \nu_e(\bar{\nu}_e). \tag{49}$$

Some of the kaons decay purely into pions, for example, in processes such as

$$K^{\pm} \to \pi^{\pm} + \pi^0, \tag{50}$$

which in turn produce neutrinos. On the other hand, cosmic rays also produce π^0 that decay to photons

$$\pi^0 \to \gamma + \gamma, \tag{51}$$

establishing a connection between high-energy astrophysical photons and neutrinos; see Sec. XI.

Up to 1 GeV, all muons decay before reaching the ground, implying a neutrino μ/e flavor ratio of

$$\frac{\nu_{\mu} + \bar{\nu}_{\mu}}{\nu_e + \bar{\nu}_e} \simeq 2. \tag{52}$$

At somewhat higher energies, μ decay becomes negligible and π and K decays dominate. The resultant ν_{μ} plus $\bar{\nu}_{\mu}$ flux is given by the fit (Gaisser and Honda, 2002; Stanev, 2004; Gaisser, 2019)[11]

$$\frac{dN_{\nu}}{dE_{\nu}} \simeq 0.0096 \frac{1}{\mathrm{cm}^2\,\mathrm{s\,sr\,GeV}} \left(\frac{E_{\nu}}{\mathrm{GeV}}\right)^{-2.7} \times \left(\frac{1}{1 + 3.7E_{\nu}\cos\theta/\epsilon_{\pi}} + \frac{0.38}{1 + 1.7E_{\nu}\cos\theta/\epsilon_K}\right), \tag{53}$$

where ϵ is the energy scale for the most probable process in propagation (decay versus interaction); for pions $\epsilon_{\pi} \simeq 115$ GeV and for kaons $\epsilon_K \simeq 850$ GeV. Moreover, θ is the zenith angle of observation.

Asymptotically at high energies the $\pi:K$ neutrino production is 1:3. The resultant flavor is mainly muonic, while the electronic one becomes negligible as shown in Fig. 27. This feature can be understood by observing that at high enough energies the muon-neutrino flux scales as $E_{\nu}^{-3.7}$, while electron neutrinos originating from muons scale as $E_{\nu}^{-4.7}$, where the extra power of E_{ν}^{-1} comes from the muon Lorentz factor that reduces its decay probability, making scattering more likely. At some energy, the ν_e and $\bar{\nu}_e$ produced directly by kaon decays take over and then their flux also scales as $E_{\nu}^{-3.7}$, but with a much smaller flux than the muon flavor.

In a first approximation, atmospheric neutrinos seen by a detector at or below the ground are isotropic. The atmospheric source mass intersected by a differential solid angle $d\Omega$ scales with r^2, which cancels the geometric $1/r^2$ flux dilution exactly, where r is the distance between detector and atmosphere in the chosen direction.

[11]We thank T. Gaisser for insightful clarifications concerning the semianalytical fit to the atmospheric muon-neutrino flux.

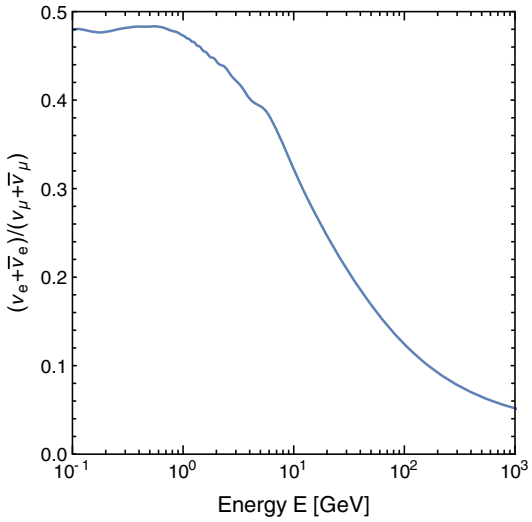

FIG. 27. Atmospheric neutrino e/μ flavor ratio, corresponding to the source fluxes (no oscillations) shown in Fig. 28.

There are important corrections to this simple picture. In fact in the few-GeV range, which was crucial for establishing flavor oscillations, the flux is essentially up-down symmetric, but it is enhanced in the horizontal direction because there is a longer decay path before muons reach the ground (Gaisser and Honda, 2002; Honda *et al.*, 2004; Stanev, 2004). A similar effect operates at high energies for kaon decays.

At energies beyond a few TeV, Earth is no longer completely transparent to neutrinos, so the flux from below is diminished (Nicolaidis, 1988; Nicolaidis, Jannane, and Tarantola, 1991; Gonzalez-Garcia *et al.*, 2008; Donini, Palomares-Ruiz, and Salvado, 2019). For energies up to about 1 PeV, neutrinos of any flavor are more efficiently absorbed than antineutrinos because they scatter on nuclei, while the scattering on electrons is negligible. Nuclei in Earth's matter are heavy and contain more neutrons (quark content udd) than protons (quark content udd). Taking into account that neutrinos (antineutrinos) can exchange a W boson with d (u), the reaction $\nu + A \to l + B$ becomes more likely than $\bar{\nu} + A \to l + B$. With increasing energy, valence quarks become negligible relative to sea quarks, so the cross sections of ν and $\bar{\nu}$ become asymptotically equal. The only exception is provided by the Glashow resonance (Glashow, 1960)

$$\bar{\nu}_e + e^- \to W^- \to X \tag{54}$$

at $E_{\nu} \simeq m_W^2/2m_e \simeq 6$ PeV, so there is a region in which $\bar{\nu}_e$ are more likely to be absorbed than ν_e.

C. Prompt neutrinos

Atmospheric neutrinos produced by charmed mesons are called prompt neutrinos (Volkova, 1980; Gondolo, Ingelman, and Thunman, 1996; Pasquali and Reno, 1999; Enberg, Reno, and Sarcevic, 2008; Gaisser, 2019). They consist of equal amounts e and μ flavor and a small τ component. The prompt flux contribution was expected to be large in the TeV to PeV range ($\epsilon_{\mathrm{charm}} \simeq$ PeV), where the only other contribution comes from kaon decay. The latter is distinguishable thanks to its

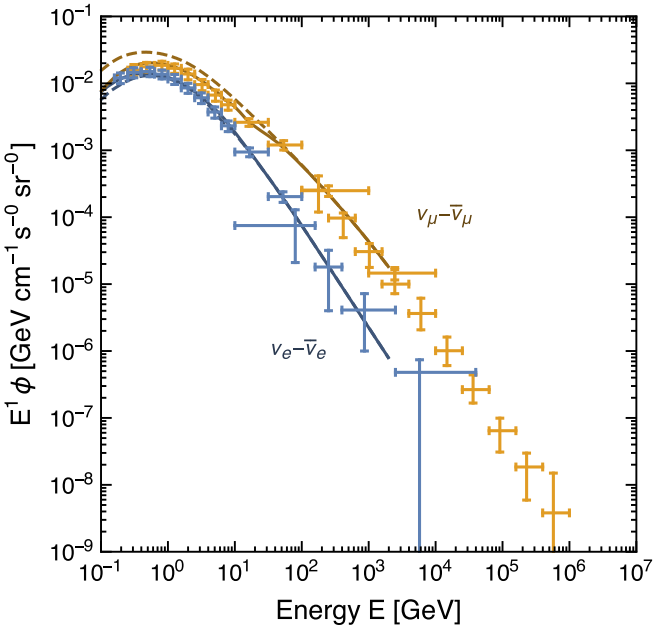

FIG. 28. Atmospheric neutrino flux per solid angle, averaged over directions, as a function of energy for $\nu_\mu + \bar{\nu}_\mu$ (upper curve, orange) and $\nu_e + \bar{\nu}_e$ (lower curve, blue). The data points at low and medium energies represent the Super-Kamiokande observations (Richard *et al.*, 2016) and of IceCube at high energies (Aartsen *et al.*, 2015c, 2015d). The dashed lines are theoretical predictions at the Kamioka site for average solar activity (Honda *et al.*, 2015); the solid lines are the expected fluxes including flavor oscillations. The $\nu_\tau + \bar{\nu}_\tau$ flux appearing in this case is not shown, corresponding to the difference between the orange dashed and solid lines.

angular distribution, which is enhanced in the horizontal direction because of the larger kaon decay path. Prompt neutrinos, instead, are isotropic up to high energies because of the short charmed-meson lifetime of 10^{-12}–10^{-13} s. Moreover, the prompt flux is harder, so it will dominate beyond a certain energy. Semianalytical expressions for the prompt flux were given by Volkova and Zatsepin (1999). The uncertainty in the estimates of this flux is quite large (Garzelli *et al.*, 2017), while conventional atmospheric neutrino predictions are affected by an ∼10% uncertainty (Honda *et al.*, 2007), the prompt flux has large uncertainties due to poor knowledge of the charm meson production processes (Garzelli, Moch, and Sigl, 2015).

Concerning recent developments, IceCube did not find a significant prompt component (Aartsen *et al.*, 2015b, 2016c). Moreover, recent calculations accounting for the latest measurements of the hadronic cross sections predicted a prompt neutrino flux that is generally lower than its previous benchmark estimation (Bhattacharya *et al.*, 2016).

D. Predictions and observations

To predict the atmospheric neutrino flux one needs to solve a set of transport equations, which are coupled integro-differential equations. While semianalytical approximations exist, numerical solutions are more reliable. To reproduce the theoretically expected flux in Fig. 28 (dashed lines), we use the tables publicly available from Honda *et al.* (2015). For the extremely low-energy ($\lesssim$100 MeV) flux included in Fig. 1, we use FLUKA results (Battistoni *et al.*, 2005). We choose Kamioka as a site because the geographic dependence is more important for low-energy neutrinos, which have been measured mostly by Super-Kamiokande. Because we are not aiming for a high-precision fit, we consider the flux under the mountain in Kamioka and take the Sun at average magnetic activity. As explained earlier, the μ/e flavor ratio begins approximately at 2 at low energies and then increases. Concerning uncertainties, Fedynitch, Becker Tjus, and Desiati (2012) quantified the systematic influence caused by the choice of primary cosmic-ray flux models and the interaction model. The average errors on the ν_μ and ν_e fluxes at high energies were found to be $^{+32\%}_{-22\%}$ and $^{+25\%}_{-19\%}$, respectively.

Neutrinos produced in the atmosphere can change flavor before reaching the detector. For the given mixing parameters (Appendix B) and for GeV energies, ν_e and $\bar{\nu}_e$ remain essentially unaffected, because the mean weak potential describing Earth's matter effect is large compared to $\delta m^2/2E$ and because they have only a small admixture of the third mass eigenstate. The main effect derives from two-flavor oscillations in the ν_μ-ν_τ sector, driven by the "atmospheric mass difference" $\Delta m^2 \sim (50\ \mathrm{meV})^2$ with an oscillation length $L_{\rm osc} = 4\pi E/\Delta m^2 \sim 990\ \mathrm{km}\, E/\mathrm{GeV}$. Therefore, neutrinos from above show the primary flavor content, whereas those from below, after traveling thousands of kilometers, show significant ν_μ disappearance. This up-down asymmetry was the smoking-gun signature detected by Super-Kamiokande (Fukuda *et al.*, 1998) and honored with the 2015 Nobel Prize in Physics for Takaaki Kajita.

The solid lines in Fig. 28 show the predicted angle-averaged fluxes when flavor oscillations are included. Without aiming for a precision comparison in our plot, they agree well with the measured fluxes that are from Super-Kamiokande at low and medium energies (10^{-1}–10^3 GeV) (Richard *et al.*, 2016) and from IceCube at high energies (10^2–10^6 GeV) (Aartsen *et al.*, 2015c, 2015d). While the primary ν_τ flux of prompt neutrinos is small, there is a large ν_τ component from flavor conversion that we do not show and that is difficult to measure because of the short lifetime of the τ lepton produced in charged-current interactions. It was only recently that the first evidence of atmospheric ν_τ appearance was reported by IceCube DeepCore (Aartsen *et al.*, 2019).

E. Experimental facilities

The main experimental facilities sensitive to atmospheric neutrinos have been IceCube (Aartsen *et al.*, 2015c, 2015d), Super-Kamiokande (Richard *et al.*, 2016), SNO (Aharmim *et al.*, 2010), and MINOS (Adamson *et al.*, 2011). SNO, although mainly built to detect solar neutrinos, also detected high-energy atmospheric neutrinos. SNO was located 2 km underground, and therefore near-horizontal downward-going muons with typical energies of 100 GeV originated as a result of the atmospheric neutrino interactions. Given the measured atmospheric Δm^2, the effect of flavor conversion is small for the near-horizontal downward-going muons. Hence, these muon data were used to calibrate the estimated atmospheric

neutrino flux. SNO is currently being replaced by its successor SNO+ (Lozza, 2019), which, however, does not have atmospheric neutrinos as a main goal for the next future. MINOS was a long-baseline neutrino oscillation experiment and has been the first magnetized tracking detector for atmospheric neutrinos.

IceCube measures atmospheric neutrinos as a background for extremely high-energy astrophysical neutrinos in the range 100 GeV–400 TeV. Neutrinos with energies up to 1 GeV will have the final-state particle "fully contained" in the detector. Muon neutrinos with higher energies may result in a muon leaving the detector, the "partially contained" events. To measure the atmospheric flux accurately, it is important to pinpoint the vertex position of the interaction and classify the neutrino event accordingly. IceCube DeepCore (Abbasi *et al.*, 2012) is an infill of eight strings added to the IceCube array and is dedicated to the detection of neutrinos with energy below 100 GeV. As with IceCube, the deep-sea Cherenkov detectors ANTARES and its successor Km3NeT (Elewyck Van, 2019) allow us to exploit atmospheric neutrinos to study flavor-oscillation physics.

The largest statistics of atmospheric neutrinos for neutrino oscillation studies is dominated by the Super-Kamiokande data. Hyper-Kamiokande (Abe *et al.*, 2018) will provide an even larger amount of data.

Among the detectors specifically dedicated to the observation of atmospheric neutrinos, there is the project of the India-based Neutrino Observatory (INO) (Indumathi, 2015). It will be located in a 1.2 km deep cave near Theni, India. INO promises to provide a precise measurement of neutrino mixing parameters.

F. Solar atmospheric neutrinos

An additional contribution to the GUNS comes from the Sun in the form of "solar atmospheric neutrinos," which are produced by cosmic-ray interactions in the solar atmosphere (Ingelman and Thunman, 1996; Argüelles *et al.*, 2017; Edsjö *et al.*, 2017; Ng *et al.*, 2017). While the production processes are analogous to those in Earth's atmosphere, the Sun's atmosphere is thinner, so pions and kaons can travel much larger distances without collisions. This results in a neutrino flux that is both larger and harder at high energies as shown in Fig. 29. The detection of low-energy ($\lesssim$1 TeV) solar atmospheric neutrinos, while not possible with ongoing experiments, would be useful to probe the magnetic field of the solar atmosphere (Ng *et al.*, 2017).

The fluxes shown in Fig. 29 correspond to Fig. 1 of Ng *et al.* (2017), where they assumed the solar magnetic field of Seckel, Stanev, and Gaisser (1991) for the flux up to 300 GeV and the model of Ingelman and Thunman (1996) at larger energies. What is shown is the primary $\nu_\mu + \bar{\nu}_\mu$ flux that will be diminished by flavor oscillations before reaching Earth.

To compare the solar flux with the diffuse background of Earth atmospheric neutrinos, the latter must be integrated over a suitable solid angle. A naive estimate is the solar angular cone $\theta_{\rm Sun} \simeq 0.17°$ (dashed orange line in Fig. 29). However, muons coming from different directions can decay producing neutrinos along a direction lying in the solar angular cone, so the flux must be integrated over the energy-dependent muon-neutrino

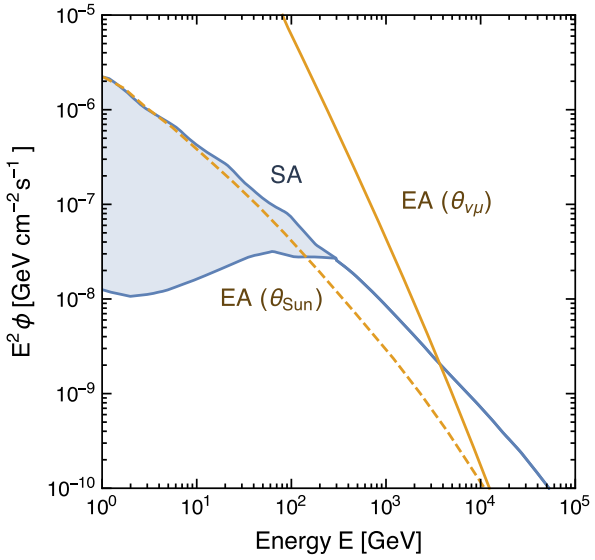

FIG. 29. The $\nu_\mu + \bar{\nu}_\mu$ solar atmospheric neutrino (SA) flux (blue) compared to Earth's (EA) (orange), the latter integrated over the solar angular cone (dashed) and over the muon-neutrino angular cone (solid); see Ng *et al.* (2017) and references therein. The SA uncertainty at low energies (blue shaded region) is due to the modeling of the magnetic fields at the solar surface and those carried by the solar wind.

separation angle $\theta_{\nu\mu} \simeq 1°\sqrt{1\ \text{TeV}/E_\nu}$ (Ng *et al.*, 2017) (solid orange line in Fig. 29 marked EA).

The detection of high-energy ($\gtrsim$1 TeV) solar atmospheric neutrinos is conceivable in 10 yr of data taking by IceCube and KM3NeT (Ng *et al.*, 2017; In and Jeong, 2018), and would mark an important milestone for neutrino astronomy, as well as being an important calibration source for future neutrino telescopes in different hemispheres.

XI. EXTRATERRESTRIAL HIGH-ENERGY NEUTRINOS

The era of high-energy neutrino astronomy was born with the detection of neutrinos of astrophysical origin by the IceCube Neutrino Observatory (Aartsen *et al.*, 2013a, 2013b, 2016c). These events have energies ranging from a few TeV to a few PeV. Their arrival directions do not exhibit anisotropies, suggesting that only up to ∼1% of the observed flux may come from our Galaxy (Ahlers and Murase, 2014; Denton, Marfatia, and Weiler, 2017; Albert *et al.*, 2018). More neutrinos are instead expected from sources distributed on cosmological scales, such as dim or choked astrophysical jets, star-forming galaxies (SFGs), gamma-ray bursts (GRBs), active galactic nuclei (AGNs), and galaxy clusters. For recent reviews see Mészáros (2017), Waxman (2017), Murase (2017), Ahlers and Halzen (2018), and Ahlers, Helbing, and Pérez de los Heros (2018).

A. Production mechanisms and detection prospects

Neutrinos in the energy range of interest are produced by cosmic-ray interactions in the source or its surroundings, or during cosmic-ray propagation en route to Earth. The reactions involve proton-proton (pp) or proton-photon ($p\gamma$)

interactions, leading to the following production channels for neutrinos and gamma rays: $\pi^0 \to \gamma + \gamma$, $\pi^\pm \to \mu^\pm + \nu_\mu(\bar{\nu}_\mu)$, and $\mu^\pm \to e^\pm + \bar{\nu}_\mu(\nu_\mu) + \nu_e(\bar{\nu}_e)$ in analogy with atmospheric neutrino production (Sec. X.B).

Before absorption and reprocessing of extremely high-energy γ rays, the relative fluxes of neutrinos and gammas is approximately regulated by the ratio of $\pi^\pm$ to π^0 production, whereas the ν-flavor distribution would be $\nu_e:\nu_\mu:\nu_\tau \simeq 1:2:0$. After a long distance of propagation, the oscillation-averaged composition reaching the detector is expected to be $\nu_e:\nu_\mu:\nu_\tau \simeq 1:1:1$ (Learned and Pakvasa, 1995; Farzan and Smirnov, 2008).

The diffuse neutrino intensity at Earth from extragalactic sources is given by the integral of the spectral distribution for each source F_{ν_α}, convolved with the source distribution (a function of redshift z and source luminosity L) over the comoving volume $\rho(z, L)$:

$$\phi(E_\nu) = \frac{1}{4\pi}\int_0^\infty dz \int_{L_{\min}}^{L_{\max}} dL_\nu \frac{1}{H(z)}\rho(z, L_\nu) \times \sum_\alpha F_{\nu_\alpha}[(1+z)E_\nu], \tag{55}$$

with $H(z)$ the Hubble factor at redshift z.

Equation (55) can be approximately expressed in the form (Waxman and Bahcall, 1998)

$$\phi_\nu = \xi \frac{L_\nu n_s R_H}{4\pi}, \tag{56}$$

where ξ accounts for the redshift evolution of sources ($\xi = 2$ or 3 is usually assumed for sources following the star-formation rate), n_s is the source density, and $R_H = c/H_0 \simeq 400$ Mpc is the Hubble radius. Comparing Eq. (56) to the diffuse flux observed by IceCube (2.8×10^{-8} GeV/cm^2 s sr), we obtain (Gaisser, Engel, and Resconi, 2016)

$$n_s L_\nu = \frac{4\times 10^{43}}{\xi}\frac{\text{erg}}{\text{Mpc}^3\,\text{yr}} \sim 10^{43}\frac{\text{erg}}{\text{Mpc}^3\,\text{yr}}. \tag{57}$$

Equation (57) provides the minimum power density necessary to produce the neutrino flux observed by IceCube. Hence any viable neutrino source needs to sit above the line defined by Eq. (57) in the luminosity-density plane in Fig. 30; such a plot was originally shown in various forms by Silvestri and Barwick (2010), Murase, Beacom, and Takami (2012), and Kowalski (2015).

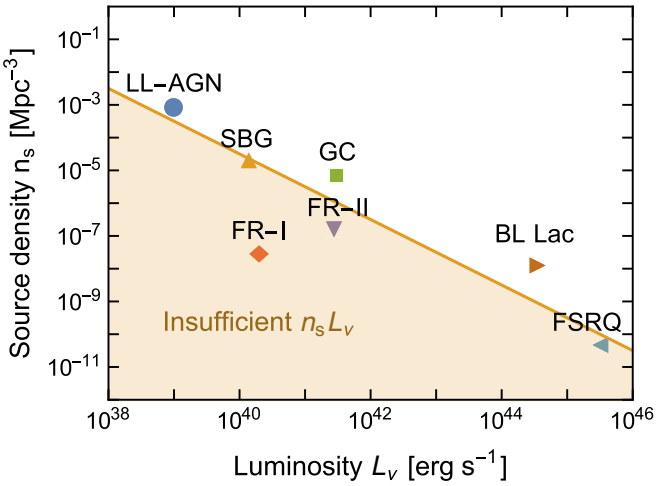

FIG. 30. Source density vs neutrino luminosity for potential sources of high-energy neutrinos. The markers are examples of benchmark astrophysical sources: low-luminosity active galactic nuclei (LL-AGNs), starburst galaxies (SBGs), galaxy clusters (GCs), BL Lacertae objects (BL-Lacs), Fanaroff-Riley galaxies of type I and II (FR-I and FR-II), and flat-spectrum radio quasars (FSRQs). See Mertsch, Rameez, and Tamborra (2017) and Ackermann *et al.* (2019) for details on the estimation of (L_ν, n_s).

B. Multimessenger connections

Assuming that all particles populating the high-energy sky originate from the same source classes, the cosmic energy density of high-energy neutrinos should be connected to the one of γ rays observed by the Fermi Telescope (Fornasa and Sánchez-Conde, 2015) and to the one of ultrahigh-energy cosmic rays seen by the Auger Observatory (Grenier, Black, and Strong, 2015); see Murase, Ahlers, and Lacki (2013) and Ahlers and Halzen (2018) for more details.

The extragalactic γ-ray background observed by the Fermi Telescope derives from pointlike sources and an isotropic component. Current IceCube data cannot be consistently interpreted by employing the same composition of sources. This is especially true for the 10–100 TeV neutrino energy spectrum that cannot be fitted by invoking a common origin for neutrinos and γ rays (Murase, Guetta, and Ahlers, 2016; Denton and Tamborra, 2018c).

A direct correlation between TeV–PeV neutrinos and ultrahigh-energy cosmic rays should also exist, but no clear evidence has been found yet (Moharana and Razzaque, 2015; Aartsen *et al.*, 2016d). Cosmic rays could be trapped in the source because of strong magnetic fields and hence produce neutrinos through collisions with the gas. The efficiency of this process is related to the total energy stored in the source under the assumption that it is calorimetric.

Cosmic rays above 3×10^{18} eV are thought to be of extragalactic origin, while a mainly galactic origin is expected at smaller energies. Observation of extragalactic cosmic rays allows one to establish an upper bound on the fluence of neutrinos of astrophysical origin produced in cosmic reservoirs; this leads to the so-called Waxman and Bahcall bound (Waxman and Bahcall, 1998; Bahcall and Waxman, 2001)

$$E_\nu \phi_\nu < 2 \times 10^{-8} \xi \text{ GeV}/(\text{cm}^2\,\text{s}\,\text{sr}), \tag{58}$$

where ξ is the same as in Eq. (56). Equation (58) should be considered an upper limit on neutrino emission from the sources of ultrahigh-energy cosmic rays under the assumption that the spectrum scales as E^{-2}, as predicted by Fermi acceleration. The Waxman and Bahcall bound was derived under the assumption that sources are optically thin to photomeson and proton-nucleon interactions such that protons

are free to escape. If optically thick sources exist, this bound does not hold.

High-energy neutrinos are emitted by a plethora of astrophysical sources; however, we focus here on SFGs, GRBs, and AGNs. These are the most efficient neutrino emitters. In particular, concerning AGNs, we focus on a subclass, blazars, currently considered to constitute the bulk of the extragalactic γ-ray diffuse emission (Ackermann *et al.*, 2016). A dozen of the IceCube neutrino events are likely to be connected to a blazar (Aartsen *et al.*, 2018a, 2018b), but given their energy those neutrino events do not contribute to the diffuse IceCube flux. The nondetection of point sources generating multiple neutrino events from astrophysical sources provides a lower limit on the local density of these sources and an upper limit on their effective neutrino luminosity (Murase and Waxman, 2016; Mertsch, Rameez, and Tamborra, 2017). Finally, we discuss the predicted flux of cosmogenic neutrinos produced by cosmic-ray interactions en route to Earth.

C. Star-forming galaxies

SFGs are stationary sources compared with transient ones, such as GRBs and AGNs, that are discussed later. SFGs are perfect examples of calorimetric sources (Loeb and Waxman, 2006; Waxman, 2017). Presumably they produce high-energy neutrinos mostly through pp interactions (Loeb and Waxman, 2006; Thompson *et al.*, 2006; Lacki *et al.*, 2011).

Beyond normal galaxies such as our Milky Way, another class of SFGs consists of starburst galaxies. These are individually more luminous than SFGs as they undergo a phase of enhanced star-formation activity (up to 100 times higher than normal galaxies).

Our understanding of star formation has dramatically improved in the past decade. In particular, the Herschel Space Observatory (Gruppioni *et al.*, 2013) provided an unprecedented estimation of the infrared luminosity function of SFGs up to redshift 4 and made possible the distinction among different subclasses. In fact, beyond normal and starburst galaxies, the Herschel Observatory provided for the first time information on SFGs containing low-luminosity AGNs or AGNs obscured by dust (after correcting for the contribution of AGNs) (Gruppioni *et al.*, 2013). All these classes contribute to the star-formation activity.

Among all galaxies, about 38% are normal, 7% are of the starburst type, and the remaining ones are SFGs containing AGNs. The abundance of each class varies as a function of redshift, with normal galaxies more abundant at low redshifts ($z < 1.5$). The γ-ray energy distribution of normal galaxies is observed to be softer ($F_\gamma \propto E_\gamma^{-2.7}$) on average than that of starburst galaxies ($F_\gamma \propto E_\gamma^{-2.2}$–$E_\gamma^{-2.3}$ (Ackermann *et al.*, 2012; Bechtol *et al.*, 2017). Finally, star-forming galaxies containing active galactic nuclei can have an energy spectral distribution resembling normal galaxies or starburst galaxies depending on redshift (Tamborra, Ando, and Murase, 2014).

Neutrinos are thought to be produced in SFGs through pp interactions under the assumption that $\mathcal{O}(100)$ PeV cosmic rays are produced and confined in these sources. This assumption might be optimistic given that the Galactic cosmic-ray spectrum breaks at 3 PeV.

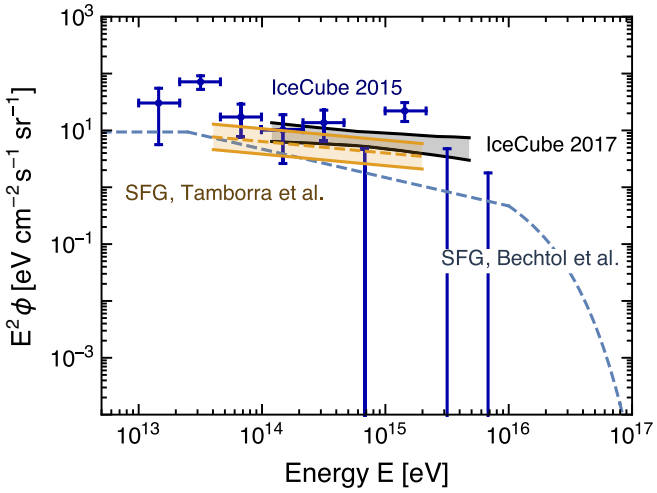

FIG. 31. Diffuse neutrino flux per flavor $\nu_\alpha + \bar{\nu}_\alpha$ from SFGs. The dashed line reproduces the results of Bechtol *et al.* (2017), where an upper limit to the contribution from blazars was calculated by analyzing the γ-ray flux. The orange band (marked "SFG, Tamborra *et al.*") reproduces the results of Tamborra, Ando, and Murase (2014) based on the infrared data. Notice that the spectral shape is slightly different given the different injection spectral indices adopted in the theoretical estimations. Also shown is the IceCube neutrino flux per flavor according to Aartsen *et al.* (2015a) (data points) and a more recent estimation including high-energy data only (Aartsen *et al.*, 2017c) (black band marked "IceCube 2017").

As a consequence of pp interactions in the source, a direct connection between the estimated neutrino and γ-ray emission can be established (Thompson *et al.*, 2006; Lacki *et al.*, 2011; Tamborra, Ando, and Murase, 2014; Senno *et al.*, 2015; Sudoh, Totani, and Kawanaka, 2018). One can then estimate the neutrino emission following the modeling proposed by Tamborra, Ando, and Murase (2014) using the infrared data from the Herschel Space Observatory (Gruppioni *et al.*, 2013). As the infrared luminosity function is connected to that of γ rays (Ackermann *et al.*, 2016), one can estimate the correspondent neutrino spectrum by applying the relation

$$\sum_{\nu_\alpha} \phi_{\nu_\alpha}(E_{\nu_\alpha}) \simeq 6\phi_\gamma(E_\gamma), \tag{59}$$

with $E_\gamma \simeq 2E_\nu$ and ϕ_γ the γ-ray diffuse intensity. The expected ϕ_{ν_α} from SFGs as a function of E_ν is shown in Fig. 31 (orange band).

Note that Bechtol *et al.* (2017) provided a more conservative upper limit on the expected neutrino emission from star-forming galaxies by relying on the most recent constraints on the diffuse extragalactic γ-ray sky from the Fermi Telescope (Ackermann *et al.*, 2016; Bechtol *et al.*, 2017); this corresponds to the dashed blue line in Fig. 31. These results are in agreement with current tomographic constraints (Ando, Tamborra, and Zandanel, 2015). The detection of neutrinos from stacked searches of star-forming galaxies is currently statistically disfavored (Murase and Waxman, 2016; Feyereisen, Tamborra, and Ando, 2017; Mertsch, Rameez, and Tamborra, 2017).

D. Gamma-ray bursts

GRBs are among the most energetic transients in our Universe. They are divided into long-duration (> 2 s) and short-duration (< 2 s) bursts according to the electromagnetic observations by BATSE (Mészáros, 2006). Long-duration GRBs are thought to originate from the death of massive stars. They are usually classified as low- and high-luminosity GRBs according to their isotropic luminosity.

High-luminosity GRBs are routinely observed by Swift and the Fermi Gamma-ray Burst Monitor. They are characterized by a Lorentz boost factor of $\Gamma \simeq 500$ and isotropic luminosity of about 10^{52} erg/s. We know less about low-luminosity GRBs mostly because they are dimmer, with a typical isotropic luminosity of about 10^{48} erg/s, and therefore are more difficult to observe. Low-luminosity GRBs have a Lorentz factor 1 order of magnitude less than high-luminosity ones.

GRBs produce high-energy neutrinos mostly through $p\gamma$ interactions (Waxman and Bahcall, 1997; Dai and Lu, 2001; Waxman, 2003; Guetta *et al.*, 2004; Mészáros, 2013). The main reactions are

$$p + \gamma \to \Delta \to n + \pi^+ \quad \text{or} \quad p + \pi^0, \tag{60a}$$

$$p + \gamma \to K^+ + \Lambda/\Sigma, \tag{60b}$$

with the pions, muons, kaons, and neutrons decaying to neutrinos of muon and electron flavor (Guetta *et al.*, 2004), as described earlier. Usually the injected photon energy distribution is parametrized through a band spectrum (broken power law) with a break energy defined as a function of the isotropic energy. According to the fireball model (Piran, 1999), because the main neutrino production channel is through $p\gamma$ interactions and the proton spectrum is proportional to E_p^{-2} (without breaks), the resultant neutrino spectrum will have a break corresponding to the break energy of the photon spectrum (Guetta *et al.*, 2004). Above the first break, the neutrino spectrum should be the same as the proton spectrum. However, radiative processes (i.e., radiation losses through synchrotron, inverse Compton, bremsstrahlung, etc.) affect the observable neutrino spectrum and steepen it at higher energies (Baerwald, Hummer, and Winter, 2012; Hummer, Baerwald, and Winter, 2012; Tamborra and Ando, 2015).

The neutrino events detected thus far by IceCube are not in spatial or temporal correlation with known GRBs (Aartsen *et al.*, 2016a, 2017a); the neutrino nonobservation from these sources places upper bounds on the neutrino emission that remains consistent with theoretical models. High-luminosity GRBs are also excluded as main sources of the diffuse high-energy neutrino flux observed by IceCube (Mészáros, 2017). However, low-luminosity or choked GRBs could produce high-energy neutrinos abundantly and partially explain the IceCube flux (Murase *et al.*, 2006; Murase *et al.*, 2008; Tamborra and Ando, 2015; Senno, Murase, and Mészáros, 2016). A choked jet is a jet successful in accelerating particles, but such that the electromagnetic radiation cannot escape (Razzaque, Mészáros, and Waxman, 2004; Ando and Beacom, 2005; Murase and Ioka, 2013). Choked jets have been invoked to explain the neutrino data in the low-energy tail of the spectrum in the 10–100 TeV range (Murase and Ioka, 2013; Murase, Guetta, and Ahlers, 2016; Senno, Murase, and Mészáros, 2016), although details of the modeling of the neutrino emission might produce results in tension with current data (Denton and Tamborra, 2018c).

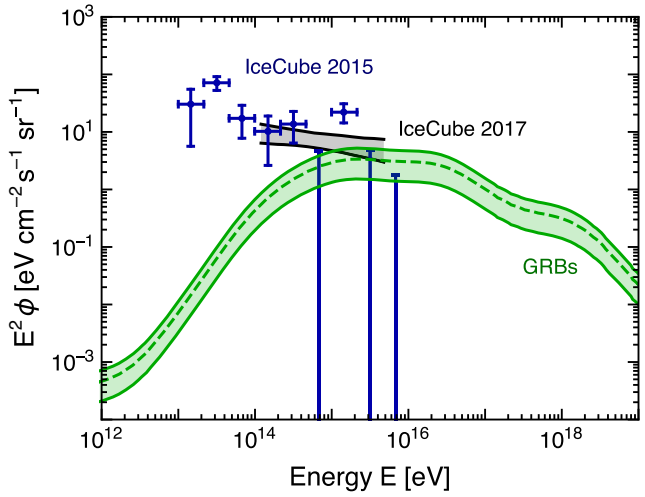

FIG. 32. Diffuse neutrino flux per flavor $\nu_\alpha + \bar{\nu}_\alpha$ from GRBs (Denton and Tamborra, 2018a). The green band marked "GRBs" tracks the uncertainty of the local star-formation rate (Strolger *et al.*, 2015). Also shown is the IceCube neutrino flux from two datasets, as in Fig. 31.

Figure 32 shows the diffuse neutrino emission per flavor ($\nu_\alpha + \bar{\nu}_\alpha$) and mass eigenstates from long-duration GRBs. It was obtained according to the advanced model presented in Fig. 5 of Denton and Tamborra (2018a), which includes high-luminosity, low-luminosity, and choked GRBs. The astrophysical uncertainty is based on the error in the measurement of the local star-formation rate (Strolger *et al.*, 2015).

Short GRBs have typical luminosities similar to those of long high-luminosity GRBs but originate from compact binary mergers. The expected diffuse neutrino background from these sources is much smaller than the one from long-duration GRBs because of the merger distribution on cosmic scales (Tamborra and Ando, 2015). However, a sizable neutrino flux could be detected if one invokes a large fraction of magnetars connected to these bursts (Fang and Metzger, 2017) or by exploiting the GRB extended emission that can potentially provide a larger target photon field (Kimura *et al.*, 2017).

E. Blazars

AGNs are mainly powered by mass accretion onto supermassive black holes at the center of their host galaxies (Padovani *et al.*, 2017). AGNs are among the most luminous sources of electromagnetic radiation and have been proposed as powerful high-energy cosmic accelerators (Murase, 2017).

AGNs can be divided in radio-quiet and radio-loud objects. The latter are characterized by an emission from the jet and lobes that is especially prominent at radio wavelengths, whereas in radio-quiet objects the continuum emission comes

from the core regions and the jet-related emission is weak. Radio-loud AGNs are promising cosmic accelerators and powerful neutrino sources.

Blazars are a special kind of loud AGNs with the jet pointing toward us. Blazars are characterized by extreme variability and strong emission over the entire electromagnetic spectrum. Blazars are divided into BL Lacertae objects (BL-Lacs) and flat-spectrum radio quasars (FSRQs). These two categories have different optical spectra, with the latter showing strong and broad emission lines and the former characterized by optical spectra with weak emission lines.

In the following, we focus on neutrino production from blazars as they are expected to be rich neutrino factories. However, radio-quiet AGNs may also contribute to the diffuse neutrino background (Murase, 2017), although the neutrino production is affected by large uncertainties.

The photon spectrum of blazars is characterized by two broad bumps (Padovani *et al.*, 2017). The low-energy peak can occur at frequencies in the range 0.01–13 keV, while the high-energy peak can be in the 0.4–400 MeV range. The low-energy emission of blazars comes from electron synchrotron radiation with the peak frequency related to the maximum energy at which electrons can be accelerated. On the other hand, the origin of the high-energy emission is still under debate: it might originate from inverse Compton radiation or from the decay of pions generated by accelerated protons.

The electromagnetic spectrum evolves with the blazar luminosity, the so-called blazar sequence. The correspondent neutrino production occurs through $p\gamma$ interactions (Protheroe, 1997; Atoyan and Dermer, 2001); in fact high-energy protons are accelerated through diffusive shock acceleration or stochastic acceleration in the jet. Protons then interact with synchrotron photons coming from nonthermal electrons that are coaccelerated in the jets. Given their abundance and brightness, the detection of neutrinos from stacked searches of blazars is statistically favored (Murase and Waxman, 2016; Feyereisen, Tamborra, and Ando, 2017; Mertsch, Rameez, and Tamborra, 2017).

BL-Lacs produce up to 40%–70% of the gamma-ray diffuse background in the 0.1–10 GeV range. Assuming that neutrinos are produced through $p\gamma$ interactions, the gamma-ray and neutrino luminosity from blazars may be connected through an efficiency factor $Y_{\nu\gamma}$ varying between 0.1 and 2 so that $L_\nu = Y_{\nu\gamma} L_\gamma$ (Petropoulou *et al.*, 2015).

To estimate the neutrino production from the blazar population, it is useful to rely on the blazar sequence. Although one can assume a distribution in the Lorentz factor of the jet, $\Gamma = 10$ is here assumed to be a representative value during a typical variability time of 10^6 s. Cosmic rays undergo Fermi acceleration and acquire a power-law energy distribution $F_p(E_p) = E_p^{-2} \exp(-E_p/E_{\max})$, with $E_{\max}$ the maximum energy that cosmic rays have in the source. In $p\gamma$ interactions, neutrinos carry about 5% of the energy of the primary proton.

The target photon field is determined according to the blazar sequence (Ghisellini *et al.*, 2017). Beyond synchrotron and inverse Compton peaks present in the BL-Lac spectral energy distribution, FSRQs typically exhibit broad lines from atomic emission of the gas surrounding the accretion disk. By deriving the neutrino spectral energy distribution from the gamma-ray one and by relying on the blazar distribution at cosmological distances as from Fermi acceleration (Ajello *et al.*, 2012, 2014), Palladino *et al.* (2019) estimated the neutrino diffuse emission from blazars by imposing bounds on the nonobservation of neutrino events from dedicated stacking searches and by assuming that the baryonic loading varies with the luminosity as a power law. The neutrino production from FSRQs is estimated to be about 30% of the BL-Lac one (Padovani *et al.*, 2015).

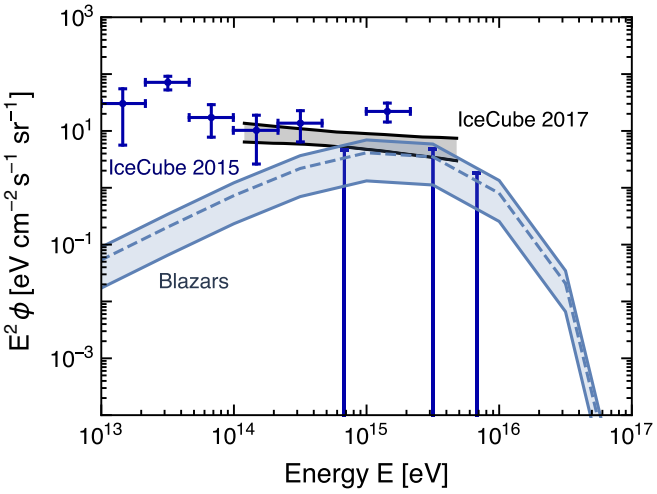

FIG. 33. Diffuse neutrino background per flavor $\nu_\alpha + \bar{\nu}_\alpha$ from blazars (Palladino *et al.*, 2019). The blue band marked "Blazars" reproduces the possible variations (1σ) due to the uncertainties on the modeling of the neutrino emission. Also shown is the IceCube neutrino flux from two datasets as in Fig. 31.

Figure 33 shows the neutrino emission per flavor from blazars. It was obtained from Scenario 3 of Palladino *et al.* (2019); the 1σ uncertainty band includes all uncertainties due to the modeling of neutrino emission. Given the large uncertainties on the modeling of the diffuse neutrino emission from blazars, we refer the interested reader to Becker, Biermann, and Rhode (2005), Murase, Inoue, and Dermer (2014), Padovani *et al.* (2015), Aartsen *et al.* (2017b), and Murase (2017) for examples of alternative independent estimations of the neutrino emission.

In this section, we focus on the diffuse neutrino emission from AGNs. However, IceCube recently reported hints for the detection of a dozen neutrino events along the direction of the blazar TXS 0506 + 056 (Aartsen *et al.*, 2018a, 2018b). The interpretation of the neutrino energy distribution is currently in tension with the corresponding electromagnetic observations; however, if confirmed, this would correspond to the first detection of high-energy neutrinos from a cosmic source.

F. Cosmogenic neutrinos

Ultrahigh-energy cosmic rays (UHECRs) have energies up to 10^{20} eV; these are the particles with the highest energies observed in nature (Anchordoqui, 2019). The sources producing them and the mechanisms behind their acceleration are unknown. Results from the Pierre Auger Observatory suggest a light composition at 1 EeV that tends to become heavier with increasing energy (Aab *et al.*, 2014). Telescope Array data

seem to confirm this trend, suggesting a mixed composition (Abbasi *et al.*, 2019).

On their way to Earth, UHECRs interact with radiation, specifically with the CMB and the extragalactic background light (EBL), which is the cosmic population of photons in the infrared range. The energy spectrum of nucleons is mostly affected by the CMB because of pair production and photopion production, whereas the energy spectrum of heavier nuclei is affected by the EBL through pair production and photodisintegration. Photopion interactions occur when nucleons N with Lorentz factor $\Gamma \geq 10^{10}$ interact with the CMB and pions are produced ($N + \gamma \to N + \pi^{0,\pm}$). For lower Γ, the same process can take place with the EBL. The strong flux suppression at high energies coming from the photopion production is responsible for the so-called Greisen-Zatsepin-Kuz'min (GZK) cutoff (Greisen, 1966; Zatsepin and Kuz'min, 1966; Abbasi *et al.*, 2008). Photodisintegration takes place when UHE nuclei are stripped by one or more nucleons by interacting with the CMB or EBL

$$(A, Z) + \gamma \to (A - n, Z - n') + nN, \tag{61}$$

where n and n' are the numbers of stripped nucleons and protons, respectively. Mesons produced in these interactions quickly decay and produce a flux of cosmogenic neutrinos (Berezinsky and Zatsepin, 1969; Allard *et al.*, 2006; Kotera, Allard, and Olinto, 2010; Ahlers and Halzen, 2012; Aloisio *et al.*, 2015; Heinze *et al.*, 2016). The β decay of nucleons and nuclei from photodisintegration can also lead to neutrino production. However, while neutrinos produced from pion decay have energies that are a few percent of the parent nucleus, those produced from β decay carry less than one part per thousand of the parent nucleon's energy.

The cosmogenic neutrino spectrum is also sensitive to the maximum UHECR energy and heavy composition at the source (or a weaker evolution of cosmic-ray sources) tends to produce a significantly lower cosmogenic neutrino flux (Aloisio *et al.*, 2015). The largest contribution is instead obtained if one assumes a proton source; this is, however, currently disfavored by Fermi data (Alves Batista *et al.*, 2019).

While the cosmic-ray spectrum is dominated by nearby sources, the neutrino flux will receive contributions up to cosmological scales. Moreover, the cosmogenic neutrino flux will also change according to the assumed source composition (Ahlers and Halzen, 2012; Aloisio *et al.*, 2015).

Cosmogenic neutrinos have not been detected yet and IceCube has recently placed a new upper limit on this flux (Aartsen *et al.*, 2016b). This nonobservation disfavors sources with a cosmological evolution that is stronger than the one predicted from the star-formation rate, such as AGNs (Aartsen *et al.*, 2016b) if one assumes a proton composition at the source. We show the predicted flux in Fig. 34, where we reproduce the results reported by Møller, Denton, and Tamborra (2019). Note that a lower cosmogenic neutrino flux may also be expected for mixed composition; see Kotera, Allard, and Olinto (2010) and Alves Batista *et al.* (2019). The upper bounds obtained by ANITA and Auger are, respectively, shown in green and orange (Ackermann *et al.*, 2019). The next generation of radio facilities, such as the Giant Radio Array for Neutrino Detection (GRAND; see the yellow curve in Fig. 34 for its projected sensitivity) and the Antarctic Ross Ice-Shelf Antenna Neutrino Array (ARIANNA), will also be able to detect this flux, which contributes to the highest-energy range in the GUNS.

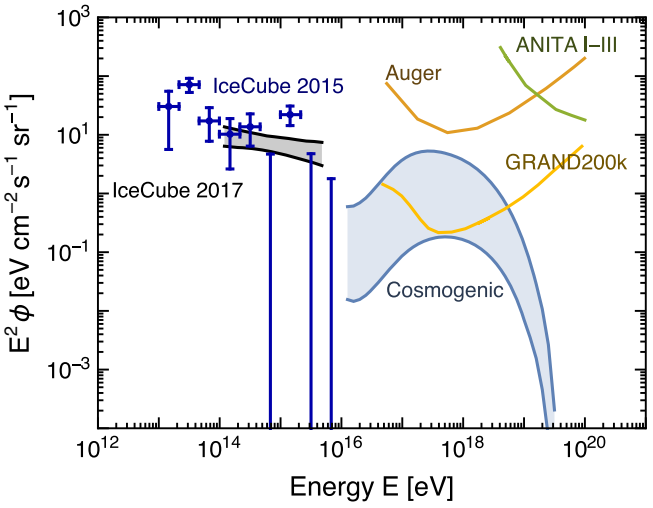

FIG. 34. Cosmogenic neutrino flux per flavor $\nu_\alpha + \bar{\nu}_\alpha$ (Møller, Denton, and Tamborra, 2019). The bands reproduce the largest possible variations due to the uncertainties on the ultrahigh-energy cosmic-ray composition and source redshift evolution. The exclusion measurements of Auger, ANITA phases I–III, and projected 3 yr sensitivity for GRAND (200 000-antenna array) are marked accordingly and shown, respectively, in orange, green, and yellow (Ackermann *et al.*, 2019; Álvarez-Muñiz *et al.*, 2020). Also shown is the IceCube neutrino flux from two datasets, as in Fig. 31.

G. Future detection prospects

IceCube remains the only experiment that detects high-energy neutrinos from astrophysical sources. Considering further experimental efforts in the field of high-energy neutrino astronomy, IceCube-Gen2 (Aartsen *et al.*, 2014) is currently under planning. Another upcoming detector is KM3NeT (Adrián-Martínez *et al.*, 2016), which will have better sensitivity to Galactic sources.

For neutrino energies above the PeV range, GRAND (Fang *et al.*, 2018) is currently being designed and developed. ARIANNA (Barwick *et al.*, 2015), a hexagonal radio array, has already delivered first constraints on cosmogenic neutrinos. The Askaryan Radio Array is currently being developed (Allison *et al.*, 2012). POEMMA (Olinto *et al.*, 2018) is being designed for the detection of cosmogenic tau neutrinos.

XII. DISCUSSION AND OUTLOOK

In analogy with the seminal grand unified photon spectrum of Ressell and Turner (1990), we have presented the GUNS. This is a complete overview of the diffuse neutrino and antineutrino backgrounds at Earth ranging from the cosmic neutrino background in the meV range to cosmogenic neutrinos reaching up to 10^{18} eV.

The lowest-energy neutrinos are those from the CNB and the $\bar{\nu}_e$'s from neutron and triton decay left over from big-bang nucleosynthesis. While these fluxes have not yet been detected, the CNB may eventually become experimentally accessible, depending on the actual neutrino mass spectrum. The lowest-energy neutrinos on our plot that have ever been observed are solar pp neutrinos down to 100 keV.

Neutrinos from nuclear reactions in the Sun and atmospheric neutrinos are the best measured and theoretically best understood sources. They have played a crucial role in detecting and exploring neutrino flavor conversion. Neutrinos from these sources continue to contribute to global fits of neutrino mixing parameters and in the search for possible nonstandard effects in the neutrino sector.

In the few-MeV range, "antineutrino astronomy" is a field encompassing geological $\bar{\nu}_e$ sources as well as nuclear power reactors. Geoneutrinos have been observed for more than a decade, but thus far with somewhat limited statistics. It will take larger detectors to begin neutrino geology in earnest. In the long run, geoneutrino research will have practical implications, e.g., it could be employed for verification in the context of nuclear nonproliferation. Reactor neutrinos remain crucial sources for investigating neutrino mixing parameters or to study coherent neutrino scattering.

Geoneutrinos and neutrinos from reactors are relevant in the same energy range as the DSNB. Likely the latter will be measured for the first time by the upcoming gadolinium-enhanced Super-Kamiokande detector and the JUNO scintillator detector, advancing the frontiers of neutrino astronomy to cosmological distances.

Atmospheric neutrinos partly overlap with the DSNB signal. Atmospheric neutrinos were crucial for the discovery of neutrino flavor conversions and to measure the neutrino mixing parameters. In the future, a precise determination of the atmospheric neutrino flux will be fundamental for the detection of the DSNB to extract better constraints on the supernova population, as well as to better discriminate among the neutrinos of astrophysical origin in the range 1–50 TeV.

Above some TeV, the neutrino backgrounds have been far less explored. The IceCube neutrino telescope detects a flux of astrophysical neutrinos up to a few PeV, whose sources remain to be discovered. At even higher energies, the detection of cosmogenic neutrinos will open a new window on the ultra-high-energy sky. Future experimental progress in this energy range will depend on increased statistics based on larger detection volumes as well as new detector technologies. An improved source identification in the context of multimessenger studies will also contribute to better exploring this part of the GUNS.

The GUNS plot reveals the neutrino potential of charting an extremely wide energy range. While astrophysical neutrinos have been instrumental for detecting flavor conversion, the mass and mixing parameters are now becoming a question of precision determination in laboratory experiments and global fits. The most exciting perspectives to learn about neutrino properties as well as their sources sit at the low- and high-energy tails of the GUNS. In particular, the branch of high and ultrahigh-energy neutrino astronomy is only in its infancy. The high-energy tail of the GUNS could unlock the secrets of the most energetic events occurring in our Universe, shed light on the origin of cosmic rays, and constrain standard and nonstandard neutrino properties.

While we hope that our GUNS plot provides a useful overview of the global neutrino flux at Earth, we also anticipate that it will continue to require frequent updating from both new observations and new theoretical ideas and insights.

ACKNOWLEDGMENTS

In Munich, Germany, we acknowledge support by the Deutsche Forschungsgemeinschaft through Grant No. SFB 1258 (Collaborative Research Center "Neutrinos, Dark Matter, Messengers") and the European Union through Grant No. H2020-MSCA-ITN-2015/674896 (Innovative Training Network "Elusives"). In Copenhagen, Denmark, this project was supported by the Villum Foundation (Project No. 13164), the Carlsberg Foundation (Grant No. CF18-0183), the Danmarks Frie Forskningsfond (Grant No. 8049-00038B), and the Knud Højgaard Foundation.

APPENDIX A: UNITS AND DIMENSIONS

We use natural units with $\hbar = c = k_{\rm B} = 1$. The neutrino flux at Earth is shown integrated over all angles for all types of sources (pointlike sources such as the Sun, diffuse such as geoneutrinos, or isotropic such as the DSNB), for example, in units $\mathrm{cm}^{-2}\,\mathrm{s}^{-1}\,\mathrm{MeV}^{-1}$. On the other hand, in Secs. X and XI we follow the convention usually adopted in the neutrino-astronomy literature and show the fluxes in units $\mathrm{cm}^{-2}\,\mathrm{s}^{-1}\,\mathrm{GeV}^{-1}\,\mathrm{sr}^{-1}$; i.e., the fluxes have been obtained by integrating over all angles and dividing by 4π.

Multiplying the angle-integrated neutrino flux with the cross section of a target particle provides a differential detection rate per target particle $d\dot{n}/dE$. To take advantage of directional capabilities in some detectors one needs to restore the angular characteristic of the neutrino flux. Dividing our 4π-integrated flux by the speed of light provides the number density at Earth per energy interval dn/dE, for example, in units of $\mathrm{cm}^{-3}\,\mathrm{MeV}^{-1}$, with the exception of nonrelativistic CNB neutrinos where the appropriate velocity has to be used. We mention these seemingly trivial details because sometimes one finds incorrect factors 4π in plots showing fluxes from both diffuse and pointlike sources.

There is no ambiguity about the local number density, which may or may not have a nontrivial angular distribution. The 4π-integrated flux can be interpreted as the number of neutrinos passing through a sphere of 1 cm^2 cross-sectional area per second. Other researchers have used the picture of neutrinos passing from one side through a disk of 1 cm^2 area per second, which is a factor $1/4$ smaller for an isotropic distribution such as the CNB. Such a definition would be appropriate for the detection of CMB photons by a horn antenna where we could count only the photons passing through the entrance cross section of the horn. Likewise, the emitted flux from a blackbody surface, as expressed by the Stefan-Boltzmann law, is a factor $1/4$ smaller than the energy density of isotropic blackbody radiation.

APPENDIX B: NEUTRINO MASS MATRIX

Neutrino fluxes from practically any source depend on flavor so that what arrives at the detector depends on flavor oscillations driven by neutrino masses and mixing. We restrict ourselves to a minimal scenario that includes only the three known species.

The weak-interaction neutrino fields ν_α with $\alpha = e$, μ, or τ are given in terms of fields with definite masses ν_i by a unitary transformation $\nu_\alpha = \sum_{i=1}^{3} \mathsf{U}_{\alpha i}\nu_i$, implying

$$|\nu_\alpha\rangle = \sum_{i=1}^{3} \mathsf{U}^*_{\alpha i}|\nu_i\rangle \quad \text{and} \quad |\bar{\nu}_\alpha\rangle = \sum_{i=1}^{3} \mathsf{U}_{\alpha i}|\bar{\nu}_i\rangle \tag{B1}$$

for neutrino and antineutrino single-particle states (Giunti and Kim, 2007). The mixing matrix is conventionally expressed in terms of three two-flavor mixing angles $0 \le \theta_{ij} < \pi/2$ and a CP-violating phase $0 \le \delta < 2\pi$ in the form

$$\begin{aligned}\mathsf{U} &= \begin{pmatrix} 1 & 0 & 0 \\ 0 & c_{23} & s_{23} \\ 0 & -s_{23} & c_{23} \end{pmatrix} \begin{pmatrix} c_{13} & 0 & s_{13}e^{-i\delta} \\ 0 & 1 & 0 \\ -s_{13}e^{-i\delta} & 0 & c_{12} \end{pmatrix} \begin{pmatrix} c_{12} & s_{12} & 0 \\ -s_{12} & c_{12} & 0 \\ 0 & 0 & 1 \end{pmatrix} \\ &= \begin{pmatrix} c_{12}c_{13} & s_{12}c_{13} & s_{13}e^{-i\delta} \\ -s_{12}c_{23} - c_{12}s_{23}s_{13}e^{i\delta} & c_{12}c_{23} - s_{12}s_{23}s_{13}e^{i\delta} & s_{23}c_{13} \\ s_{12}s_{23} - c_{12}c_{23}s_{13}e^{i\delta} & -c_{12}s_{23} - s_{12}c_{23}s_{13}e^{i\delta} & c_{23}c_{13} \end{pmatrix},\end{aligned} \tag{B2}$$

where $c_{ij} = \cos\theta_{ij}$ and $s_{ij} = \sin\theta_{ij}$. We have left out a factor $\mathrm{diag}(1, e^{i\alpha_{21}/2}, e^{i\alpha_{31}/2})$ of Majorana phases that are important in neutrinoless double beta decay, but not for flavor oscillations.

The best-fit mixing angles determined from global fits of all flavor-oscillation data are given in Table V. Within uncertainties, the octant of θ_{23} remains unknown, i.e., if $\sin^2\theta_{23}$ is larger or smaller than $1/2$. CP violation is favored, but the range of allowed δ remains large.

With the results of Table V for normal mass ordering one finds the matrix of mixing probabilities, which is the same for ν and $\bar{\nu}$,

$$(|\mathsf{U}_{\alpha i}|^2) = \begin{pmatrix} 0.681^{+0.013}_{-0.014} & 0.297^{+0.014}_{-0.013} & 0.0214^{+0.0009}_{-0.0007} \\ 0.109^{+0.074}_{-0.035} & 0.352^{+0.080}_{-0.065} & 0.539^{+0.019}_{-0.069} \\ 0.210^{+0.040}_{-0.073} & 0.351^{+0.067}_{-0.082} & 0.439^{+0.069}_{-0.019} \end{pmatrix}. \tag{B3}$$

The uncertainties correspond to the maximal and minimal values within the 1σ ranges shown in Table V. The rows and columns of this matrix of probabilities always have to add up to 1. The first row means that a produced ν_e has a 68% chance to be a ν_1, 30% to be ν_2, and 2% to be ν_3. The mass eigenstates are conventionally numbered such that the probabilities in the first row appear in declining order, i.e., according to the ν_i admixtures to ν_e.

TABLE V. Neutrino mixing angles according to Capozzi *et al.* (2018), which are similar to those of Esteban *et al.* (2017) and de Salas *et al.* (2018).

	Normal ordering		Inverted ordering	
	Best fit	1σ range	Best fit	1σ range
$\sin^2\theta_{12}$	0.304	0.291–0.318	0.303	0.290–0.317
$\sin^2\theta_{13}$	0.0214	0.0207–0.0223	0.0218	0.0211–0.0226
$\sin^2\theta_{23}$	0.551	0.481–0.570	0.557	0.533–0.574
δ/π	1.32	1.14–1.55	1.52	1.37–1.66

The matrix U being unitary, its inverse U^{-1}, which allows us to express mass states in terms of flavor states, is identical with its conjugate transpose $\mathsf{U}^\dagger$. Therefore, the probabilities for finding a given mass eigenstates in any of the flavors correspond to the columns of Eq. (B3). The last column tells us that a ν_3, for example, in the cosmic neutrino background, has a 2% chance of being ν_e, a 54% chance of being ν_μ, and 44% of being ν_τ, and likewise for the other columns.

The numbering convention of mass states leaves open the ordering of the mass values. The matter effect on flavor conversion in the Sun implies $m_1 < m_2$. The atmospheric ordering may be normal with $m_1 < m_2 < m_3$ or inverted with $m_3 < m_1 < m_2$. Global fits somewhat prefer normal ordering. The probability matrix for inverted ordering is similar to Eq. (B3) within the shown uncertainties.

Flavor oscillations of relativistic neutrinos are driven by the squared-mass differences. We express the mass spectrum in terms of the parameters (Capozzi *et al.*, 2018)

$$\delta m^2 = m_2^2 - m_1^2 = 73.4\ \mathrm{meV}^2, \tag{B4a}$$

$$\Delta m^2 = m_3^2 - \frac{m_1^2 + m_2^2}{2} = \pm 2.45 \times 10^3\ \mathrm{meV}^2, \tag{B4b}$$

where normal ordering corresponds to $\Delta m^2 > 0$ and inverted ordering corresponds to $\Delta m^2 < 0$. The nominal 1σ range of the measured values is 1.4% and 2.2%, respectively. The small mass splitting δm^2 is also called the solar mass difference because it drives solar neutrino conversion, whereas Δm^2 is the atmospheric one. Often the atmospheric splitting is instead identified with either $m_3^2 - m_2^2$ or $m_1^2 - m_3^2$, depending on the mass ordering, which, however, is a less practical convention.

Direct laboratory limits on the unknown overall mass scale of approximately 2 eV derive from the electron end point spectrum in tritium β decay (Tanabashi *et al.*, 2018). The KATRIN experiment is expected to improve the sensitivity to approximately 0.2 eV in the near future (Arenz *et al.*, 2018).

Cosmological data constrain the fraction of hot dark matter, implying 95% C.L. limits $\sum m_\nu < 0.11$–0.68 eV, depending on the data and cosmological model used (Ade *et al.*, 2016; Lesgourgues and Verde, 2018; Aghanim *et al.*, 2020). Near-future surveys should be able to set a lower limit, i.e., provide a neutrino-mass detection (Lesgourgues and Verde, 2018). These results have to be interpreted with the usual caveats about cosmological assumptions and possible unrecognized systematics.

The neutrino signal from the next nearest supernova can provide a 95% C.L. time-of-flight limit of 0.14 eV if the emission shows few-millisecond time variations caused by hydrodynamic instabilities as suggested by 2D and 3D simulations (Ellis *et al.*, 2012).

Searches for neutrinoless double beta decay are sensitive only to Majorana masses, and specifically to the combination $\langle m_\nu \rangle = |\sum_{i=1}^{3} \mathsf{U}_{ei}^2 m_i|$. Current limits are on the level of 0.11–0.52 eV, depending on the isotope and on uncertainties of the nuclear matrix elements (Tanabashi *et al.*, 2018).

APPENDIX C: NEUTRINO MIXING IN MATTER

When they propagate in matter, neutrinos experience a flavor-dependent potential caused by the electroweak interaction. In a normal medium consisting of nuclei and electrons, it is

$$V_{\rm weak} = \pm\sqrt{2} G_{\rm F} n_B \times \begin{cases} Y_e - Y_n/2 & \text{for } \nu_e, \\ -Y_n/2 & \text{for } \nu_{\mu,\tau}, \end{cases} \tag{C1}$$

where n_B is the baryon density, $Y_e = n_e/n_B$ is the net electron fraction per baryon (electrons minus positrons), and $Y_n = n_n/n_B$ is the neutron fraction. The upper sign is for ν, and the lower sign is for $\bar{\nu}$. Equivalently, we can use a nominally negative baryon density to denote the $\bar{\nu}$ potential. Radiative corrections actually provide a small difference between the ν_μ and ν_τ potentials (Botella, Lim, and Marciano, 1987; Mirizzi *et al.*, 2009), as does the possible presence of muons in a supernova core (Bollig *et al.*, 2017). We also ignore background neutrinos that complicate neutrino propagation in the form of collective flavor evolution (Duan, Fuller, and Qian, 2010).

The flavor of a neutrino of fixed energy E evolves as a function of distance z as $i\partial_z \Psi = (\mathsf{H}_0 + \mathsf{V})\Psi$, where Ψ is a three-vector of flavor amplitudes, whereas antineutrinos evolve as $i\partial_z \bar{\Psi} = (\mathsf{H}_0^* - \mathsf{V})\bar{\Psi}$. In the ultrarelativistic limit, the mass contribution in the flavor basis is

$$\mathsf{H}_0 = \frac{1}{2E} \mathsf{U} \begin{pmatrix} m_1^2 & 0 & 0 \\ 0 & m_2^2 & 0 \\ 0 & 0 & m_3^2 \end{pmatrix} \mathsf{U}^\dagger \tag{C2}$$

and the matrix of potential energies is

$$\mathsf{V} = \sqrt{2} G_{\rm F} \begin{pmatrix} n_e - n_n/2 & 0 & 0 \\ 0 & -n_n/2 & 0 \\ 0 & 0 & -n_n/2 \end{pmatrix}. \tag{C3}$$

Without flavor mixing, the in-medium dispersion relation in the relativistic limit is given by the effective masses $m_{\rm eff}^2 = m^2 + V_{\rm weak} 2E$, shown as thin gray lines in Fig. 35 for a schematic choice of mass and mixing parameters. A nominally negative density is used to show the energy levels for antineutrinos. The background medium is taken to have equal densities of electrons and neutrons, as would be the case for ^{4}He or ^{12}C. For a different composition, the lines acquire a

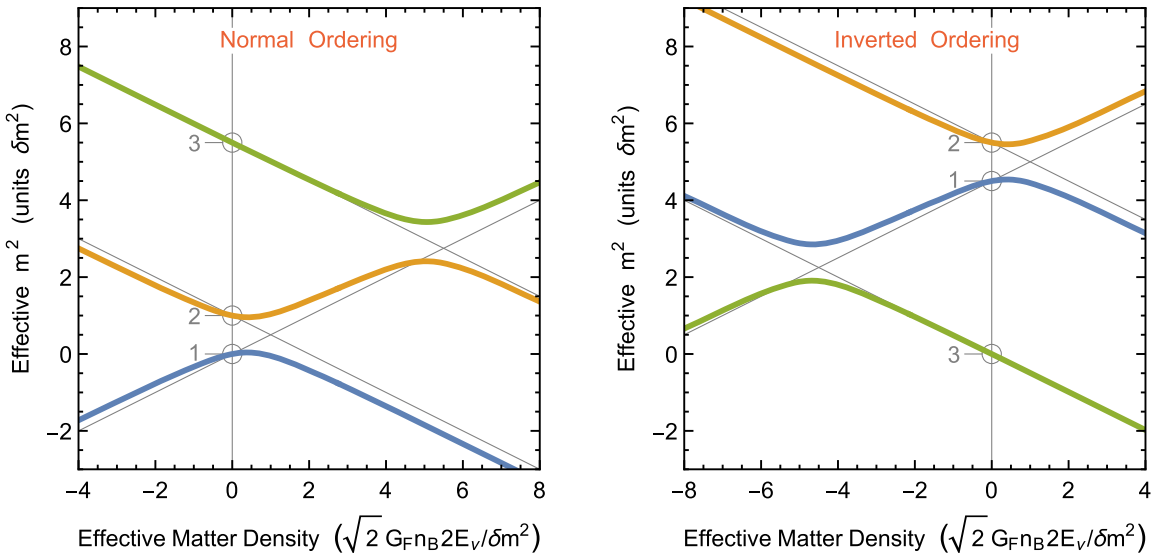

FIG. 35. Effective neutrino masses in a medium in units of the solar mass difference δm. For this schematic plot $m_1 = 0$, the atmospheric mass difference was chosen as $\Delta m^2 = 5\delta m^2$, and the mixing angles were chosen as $\sin^2\theta_{12} = 0.30$ and $\sin^2\theta_{13} = 0.01$. The electron and neutron densities were taken to be equal ($n_e = n_n = n_B/2$), which is appropriate for a medium consisting of ^{4}He or ^{12}C. A negative density is to be interpreted as a positive density for the energy levels of antineutrinos. At zero density the levels are the squared vacuum masses. The thin gray lines are the energy levels for vanishing mixing angles.

different slope caused by the common neutral-current potential for all flavors.

For nonvanishing mixing angles, the effective masses are obtained by diagonalizing $\mathsf{H}_0 + \mathsf{V}$, which is achieved by a unitary matrix U_M such that

$$\mathsf{M}^2_\mathrm{eff} = \begin{pmatrix} m^2_{1,\mathrm{eff}} & 0 & 0 \\ 0 & m^2_{2,\mathrm{eff}} & 0 \\ 0 & 0 & m^2_{3,\mathrm{eff}} \end{pmatrix} = \mathsf{U}^\dagger_\mathrm{M}(\mathsf{U}\mathsf{M}^2\mathsf{U}^\dagger + 2E\mathsf{V})\mathsf{U}_\mathrm{M}. \tag{C4}$$

For antineutrinos, one substitutes $\mathsf{V} \to -\mathsf{V}$ and $\delta \to -\delta$, the latter equivalent to $\mathsf{U} \to \mathsf{U}^*$. Notice that $m^2_{i,\mathrm{eff}}$ can be negative because it is just a formal way for writing the in-medium energy levels. In Fig. 35, the $m^2_{i,\mathrm{eff}}$ are shown as thick colored lines. Notice that θ_{23} and δ do not enter if the ν_μ and ν_τ potentials are equal; otherwise there will be a third level crossing. Notice also that asymptotically the colored lines have a nonvanishing offset relative to the gray lines.[12]

Of particular interest is the case of neutrinos produced at high density in the interior of a star that then propagate all the way to the surface. If the propagation is adiabatic (and this is the case for solar and supernova neutrinos), a state originally in a propagation eigenstate emerges as such. Thus we should decompose the flavor states at the point of production into local propagation states that then connect to vacuum mass states at the stellar surface (MSW effect). In sufficiently dense matter, the propagation eigenstates coincide with interaction eigenstates. In Fig. 35 (normal ordering), ν_e produced at extremely high density corresponds to the largest m^2_eff, i.e., the thick green line. Following this line to zero density (vacuum), we see that a produced ν_e emerges as the mass eigenstate ν_3. Conversely, a $\bar{\nu}_e$ (large negative density) is on the blue line and thus emerges as ν_1. A detailed discussion of all such cases, relevant in the supernova context, was provided by Dighe and Smirnov (2000).

Often the flavor-diagonal contribution to V provided by neutrons is not included because it drops out of the oscillation equation. In this case, and using the best-fit mixing parameters in normal ordering from Table V, the same plot of $m^2_{i,\mathrm{eff}}$ is shown in Fig. 36 (top panel). In the Sun, the central density is 150 g cm^{-3} with $Y_e = 0.681$, corresponding to $n_e = 6.14 \times 10^{25}$ cm^{-3} $= 4.72 \times 10^{11}$ eV^3 and thus to $V_e = 7.8 \times 10^{-12}$ eV, where

$$V_e = \sqrt{2} G_\mathrm{F} n_e. \tag{C5}$$

With $E = 18.8$ MeV, near the highest solar ν_e energy, one finds that $V_e 2E < 233$ meV$^2 = 4.0\ \delta m^2$, as indicated by a vertical dashed line in Fig. 36.

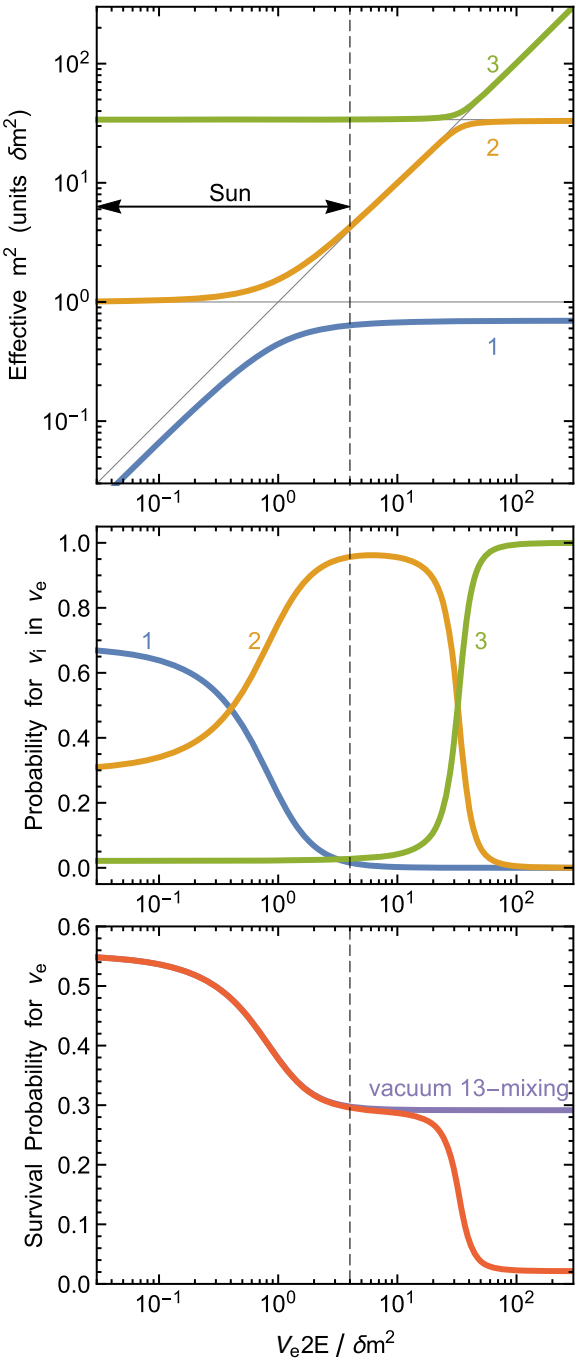

FIG. 36. Neutrino mixing in matter. Top panel: effective masses squared $m^2_{i,\mathrm{eff}}$, with $i = 1$, 2, or 3, in units of the solar value δm^2. The neutron contribution, which is flavor diagonal, has been ignored. The mixing parameters are the best-fit values in normal ordering from Table V. In the Sun, the maximum on the horizontal axis is 4.0 (vertical dashed line), corresponding to $n_e = 6.14 \times 10^{25}$ cm^{-3} at the solar center and the largest ν_e energy of $E = 18.8$ MeV. Middle panel: probability of a produced ν_e to be in the propagation eigenstate 1, 2, or 3, corresponding to $|\mathsf{U}^\mathrm{M}_{ei}|^2$. Bottom panel: probability of a produced ν_e, after adiabatic propagation, to be measured as a ν_e according to Eq. (C6). For solar conditions (left of the dashed line), ignoring the matter effect on 13 mixing yields a good approximation.

[12]Similar plots in the context of supernova neutrinos (Dighe and Smirnov, 2000) showed in-medium curves asymptotically approaching the zero-mixing lines. This behavior is caused by the transition from their Eq. (43) to their Eq. (44), where one should expand consistently to lowest order in all m^2.

The probability for ν_e that was produced in the medium to be found in any of the propagation eigenstates i is $P_{ei}^{\rm M} = |{\sf U}_{ei}^{\rm M}|^2$, which is shown in Fig. 36 (middle panel) from a numerical solution for $\mathsf{U}_{\rm M}$ using the best-fit mixing parameters. At zero density, P_{ei} correspond to the top row in the matrix of Eq. (B3). At extremely high density, ν_e essentially coincides with ν_3, so after adiabatic propagation it would emerge in the third mass eigenstate, as mentioned earlier.

Neutrinos propagating from a distant source decohere into mass eigenstates, so, for example, ν_e produced in the Sun arrive with probabilities P_{ei} in the different mass eigenstates, depending on the exact point of production and depending on their energy. A detector that is sensitive only to ν_e projects from each of the ν_i fluxes the ν_e component, corresponding to the probability $|\mathsf{U}_{ei}|^2$, so the ν_e survival probability is

$$P_{ee} = \sum_{i=1}^{3} |{\sf U}_{ei}^{\rm M}|^2 |\mathsf{U}_{ei}|^2, \tag{C6}$$

shown as a red line in Fig. 36 (bottom panel). For neutrinos produced at extremely low density and/or with extremely low energies, this is, using Eq. (B2),

$$P_{ee}^{\rm vac} = (c_{12}^4 + s_{12}^4)c_{13}^4 + s_{13}^4 = 0.553, \tag{C7}$$

where the numerical value is for the best-fit mixing angles in normal mass ordering.

The mass differences are hierarchical, $\delta m^2 \ll \Delta m^2$, allowing for an approximate determination of $\mathsf{U}_{\rm M}$ (Denton, Minakata, and Parke, 2016; Ioannisian and Pokorski, 2018). Writing it in the form of Eq. (B2), one finds for the in-medium mixing angles $\theta_{23}^{\rm M} = \theta_{23}$, $\delta^{\rm M} = \delta$, and

$$2\theta_{12}^{\rm M} = \arctan\left(\cos 2\theta_{12} - \epsilon_\odot, \cos\theta'_{13}\sin 2\theta_{12}\right), \tag{C8a}$$

$$2\theta_{13}^{\rm M} = \arctan\left(\cos 2\theta_{13} - \epsilon_{\rm a}, \sin 2\theta_{13}\right), \tag{C8b}$$

where $\theta'_{13} = \theta_{13}^{\rm M} - \theta_{13}$. Here $\alpha = \arctan(x, y)$ is an angle such that $\sin\alpha = y/\sqrt{x^2+y^2}$ and $\cos\alpha = x/\sqrt{x^2+y^2}$. Further,

$$\epsilon_\odot = \frac{2EV_e}{\delta m^2}\left(\cos^2\theta_{13}^{\rm M} + \frac{\sin^2\theta'_{13}}{\epsilon_{\rm a}}\right), \tag{C9a}$$

$$\epsilon_{\rm a} = \frac{2EV_e}{m_3^2 - m_1^2 - \delta m^2\sin^2\theta_{12}}, \tag{C9b}$$

where $\epsilon_{\rm a} < 0$ for inverted mass ordering ($m_3^2 < m_1^2$). The approximate analytic probabilities $|U_{ei}^{\rm M}|^2$ agree well with the numerical values shown in the middle panel of Fig. 36. The agreement is better than 10^{-3} except for $|U_{e1}^{\rm M}|^2$, where above 10 on the horizontal axis the analytic probability falls off faster than the numerical one. The differences between analytic and numerical solutions are essentially irrelevant on a level of precision where we have ignored radiative corrections to the weak potential.

The maximum value of $2EV_e$ in the Sun is small compared to $m_3^2 - m_1^2$, so for solar conditions we may neglect the matter effect on θ_{13}. In this case $\mathsf{U}_{\rm M}$ is given in terms of the vacuum mixing angles except for

$$2\theta_{12}^{\rm M} = \arctan\left(\cos 2\theta_{12} - \epsilon_\odot, \sin 2\theta_{12}\right), \tag{C10}$$

with

$$\epsilon_\odot = \frac{2EV_e}{\delta m^2}\cos^2\theta_{13}. \tag{C11}$$

In this case, the probability for a produced ν_e to be found in any of the three propagation eigenstates is

$$P_{e1} = \cos^2\theta_{13}\cos^2\theta_{12}^{\rm M}, \tag{C12a}$$

$$P_{e2} = \cos^2\theta_{13}\sin^2\theta_{12}^{\rm M}, \tag{C12b}$$

$$P_{e3} = \sin^2\theta_{13}. \tag{C12c}$$

The ν_e survival probability is

$$P_{ee} = \frac{1 + \cos 2\theta_{12}\cos 2\theta_{12}^{\rm M}}{2}\cos^4\theta_{13} + \sin^4\theta_{13}, \tag{C13}$$

marked as "vacuum 13–mixing" in Fig. 36 (bottom panel). The best-fit value $\sin^2\theta_{13} = 0.0214$ implies that we can safely neglect $\sin^4\theta_{13}$, whereas $\cos^4\theta_{13} = 0.958$ deviates significantly from 1.

APPENDIX D: CONSTRUCTING THE GUNS PLOT

For those wishing to construct their own version of the GUNS plot of Fig. 1, we provide here the exact input information that we have used. We also provide numerical tables, enclosed as ancillary files [Supplemental Material (502)], that can be used for this purpose.

The GUNS plot shows the sum over all flavor or mass eigenstates for neutrinos (solid lines) and antineutrino (dashed lines). Notice that the uncertainty bands for atmospheric, IceCube, and cosmogenic neutrinos are only indicative because in the literature one finds $E^2\phi_\nu$ and its uncertainty, so the uncertainty of ϕ_ν also depends on the energy uncertainty in a steeply falling spectrum.

The IceCube and cosmogenic fluxes in Fig. 1 can be compared to the corresponding figures in the main text by multiplying the curves in Fig. 1 with $E^2/4\pi \times 2/3$. In Fig. 1 we show an angle-integrated flux, hence the factor $1/4\pi$, to obtain the fluxes per solid angle, shown usually in the high-energy neutrino-astronomy literature. The factor $1/3$ translates the sum over all flavors to a single-flavor flux, assuming flavor equipartition arriving at Earth. The factor 2 sums over neutrinos plus antineutrinos.

1. Cosmic neutrino background.—For the CNB we assume the neutrino masses of Eq. (2). We show blackbody radiation for one mass eigenstate, following Eq. (6) and listed as a numerical table in the file `CNB.dat` [Supplemental Material (502)]. In addition there are two line sources (expressed in

units of $\mathrm{cm}^{-2}\,\mathrm{s}^{-1}$ in the upper panel of Fig. 1 and in units of $\mathrm{eV}\,\mathrm{cm}^{-2}\,\mathrm{s}^{-1}$ in the lower panel), corresponding to the m_2 and m_3 mass eigenstates. The normalization is given by the integral of Eq. (2). The line fluxes can be found in the file `CNB-lines.dat` [Supplemental Material (502)].

2. Neutrinos from big-bang nucleosynthesis.—For neutrinos produced by the decay of neutrons and tritium during big-bang nucleosynthesis, we adopt the fluxes given by Ivanchik and Yurchenko (2018). The tables `BBN-neutron.dat` and `BBN-tritium.dat` [Supplemental Material (502)] are courtesy of them.

3. Thermal neutrinos from the Sun.—For neutrinos produced by thermal processes in the Sun we use the flux computed by Vitagliano, Redondo, and Raffelt (2017); see the table `Sun-thermal.dat` [Supplemental Material (502)].

4. Solar neutrinos from nuclear reactions.—The solar neutrino flux is equivalent to Fig. 7. The flux from the *pp* chains and CNO cycle is given (except for hep) by the measurements shown in Table I. For the CNO and hep fluxes the range is bracketed by the lowest AGSS09 and highest GS98 predictions. The flux is given by the sum of all the processes contributing to the solar neutrino flux, which can be found in `tables/Sun-nuclear-B8.dat`, `tables/3515 Sun-nuclear-N13.dat`, `tables/Sun-nuclear- 3516 O15.dat`, `tables/Sun-nuclear-hep.dat`, and `3517 tables/Sun-nuclear-pp.dat` [Supplemental Material (502)]. The lines due to electron capture are provided in `Sun-lines.dat` [Supplemental Material (502)].

5. Geoneutrinos.—The average geoneutrino flux is the sum over the different processes shown in Fig. 13. We used the publicly available data given by Enomoto (2005). The flux is tabulated in `Geoneutrinos.dat` [Supplemental Material (502)].

6. Reactor neutrinos.—The reactor $\bar{\nu}_e$ flux is tabulated in `Reactor.dat` [Supplemental Material (502)] for the example of 140 MW thermal power and a detector at a close distance of 81 m. We assume that each reaction release 205 MeV and the number of neutrinos per reaction per unit energy is obtained as in Fig. 15 (see also the main text). Notice that this is not equivalent to the JOYO detector example shown in Fig. 16. The choice of this reactor-detector system is arbitrary and can be rescaled accordingly. What to show on the GUNS plot is somewhat arbitrary because reactor fluxes depend most sensitively on the locations of all GUNS components.

7. Diffuse supernovae neutrino background.—The DSNB neutrino and antineutrino fluxes can be found in `DSNB.dat` [Supplemental Material (502)]. The table has five entries: energy, lower and upper bound for the neutrino flux, and lower and upper bound for the antineutrino flux. Each flux was calculated as $\phi_{\nu_e} + 2\phi_{\nu_x}$. The uncertainty band was obtained considering the simplified scenario discussed in the main text for the supernova masses $(9.6, 27, 40)M_\odot$, with (50,20,21)% and (59,32,9)% for the supernova models.

8. Atmospheric neutrinos.—Atmospheric neutrino and antineutrino fluxes can be found in `Atmospheric.dat` [Supplemental Material (502)], in each case the sum of the electron and muon flavored fluxes. The low-energy points ($\lesssim$100 MeV) are from the tables given by Battistoni *et al.* (2005), while the energy range (100 MeV $\lesssim E \lesssim$ 1 TeV) is from the publicly available results given by Honda *et al.* (2015). We show the flux for average solar activity at the Kamioka site. The high-energy ($E \gtrsim 1$ TeV) flux is taken from Aartsen *et al.* (2015c) and Richard *et al.* (2016).

9. IceCube neutrinos.—The high-energy astrophysical neutrino flux (in units $10^{-20}\,\mathrm{eV}^{-1}\,\mathrm{cm}^{-2}\,\mathrm{s}^{-1}$), as measured by IceCube, is tabulated in `IceCube.dat` [Supplemental Material (502)] with upper and lower bounds of the expected cosmogenic flux. These data are taken from the high-energy event analysis of Aartsen *et al.* (2017c).

10. Cosmogenic neutrinos.—Cosmogenic neutrinos are tabulated in three columns in `Cosmogenic.dat` [Supplemental Material (502)], i.e., energy and fluxes (in units $10^{-30}\,\mathrm{eV}^{-1}\,\mathrm{cm}^{-2}\,\mathrm{s}^{-1}$) for two models of the primary cosmic-ray composition, taken to represent an upper and a lower bound. The data used in the figure were estimated by Møller, Denton, and Tamborra (2019).

11. Overall GUNS plot.—As an example for constructing the GUNS plot from these data files we also include a *Mathematica* notebook named `Produce-your-GUNS.nb` [Supplemental Material (502)] that can be used to create other variations of this plot.

REFERENCES

Aab, A., *et al.* (Pierre Auger Collaboration), 2014, "Depth of maximum of air-shower profiles at the Pierre Auger Observatory. II. Composition implications," Phys. Rev. D **90**, 122006.

Aartsen, M. G., *et al.* (IceCube Collaboration), 2013a, "Evidence for high-energy extraterrestrial neutrinos at the IceCube detector," Science **342**, 1242856.

Aartsen, M. G., *et al.* (IceCube Collaboration), 2013b, "First Observation of PeV-Energy Neutrinos with IceCube," Phys. Rev. Lett. **111**, 021103.

Aartsen, M. G., *et al.* (IceCube Collaboration), 2014, "IceCube-Gen2: A vision for the future of neutrino astronomy in Antarctica," arXiv:1412.5106.

Aartsen, M. G., *et al.* (IceCube Collaboration), 2015a, "A combined maximum-likelihood analysis of the high-energy astrophysical neutrino flux measured with IceCube," Astrophys. J. **809**, 98.

Aartsen, M. G., *et al.* (IceCube Collaboration), 2015b, "Atmospheric and astrophysical neutrinos above 1 TeV interacting in IceCube," Phys. Rev. D **91**, 022001.

Aartsen, M. G., *et al.* (IceCube Collaboration), 2015c, "Development of a general analysis and unfolding scheme and its application to measure the energy spectrum of atmospheric neutrinos with IceCube," Eur. Phys. J. C **75**, 116.

Aartsen, M. G., *et al.* (IceCube Collaboration), 2015d, "Measurement of the atmospheric ν_e spectrum with IceCube," Phys. Rev. D **91**, 122004.

Aartsen, M. G., *et al.* (IceCube Collaboration), 2016a, "An all-sky search for three flavors of neutrinos from gamma-ray bursts with the IceCube neutrino observatory," Astrophys. J. **824**, 115.

Aartsen, M. G., *et al.* (IceCube Collaboration), 2016b, "Constraints on Ultrahigh-Energy Cosmic-Ray Sources from a Search for Neutrinos above 10 PeV with IceCube," Phys. Rev. Lett. **117**, 241101; **119**, 259902(E) (2017).

Aartsen, M. G., *et al.* (IceCube Collaboration), 2016c, "Observation and characterization of a cosmic muon neutrino flux from the northern hemisphere using six years of IceCube data," Astrophys. J. **833**, 3.

Aartsen, M. G., *et al.* (IceCube, Pierre Auger, and Telescope Array Collaborations), 2016d, "Search for correlations between the arrival directions of IceCube neutrino events and ultrahigh-energy cosmic rays detected by the Pierre Auger Observatory and the Telescope Array," J. Cosmol. Astropart. Phys. 01, 037.

Aartsen, M. G., *et al.* (IceCube Collaboration), 2017a, "Extending the search for muon neutrinos coincident with gamma-ray bursts in IceCube data," Astrophys. J. **843**, 112.

Aartsen, M. G., *et al.* (IceCube Collaboration), 2017b, "The contribution of Fermi-2LAC blazars to the diffuse TeV-PeV neutrino flux," Astrophys. J. **835**, 45.

Aartsen, M. G., *et al.* (IceCube Collaboration), 2017c, "The IceCube Neutrino Observatory—Contributions to ICRC 2017 Part II: Properties of the atmospheric and astrophysical neutrino flux, arXiv:1710.01191.

Aartsen, M. G., *et al.* (IceCube Collaboration), 2018a, "Neutrino emission from the direction of the blazar TXS 0506+056 prior to the IceCube-170922A alert," Science **361**, 147.

Aartsen, M. G., *et al.* (Liverpool Telescope, MAGIC, H.E.S.S., AGILE, Kiso, VLA/17B-403, INTEGRAL, Kapteyn, Subaru, HAWC, Fermi-LAT, ASAS-SN, VERITAS, Kanata, IceCube, and Swift NuSTAR Collaborations), 2018b, "Multimessenger observations of a flaring blazar coincident with high-energy neutrino IceCube-170922A," Science **361**, eaat1378.

Aartsen, M. G., *et al.* (IceCube Collaboration), 2019, "Measurement of atmospheric tau neutrino appearance with IceCube DeepCore," Phys. Rev. D **99**, 032007.

Abazajian, K., *et al.*, 2012, "Light sterile neutrinos: A white paper," arXiv:1204.5379.

Abbasi, R., *et al.* (IceCube Collaboration), 2012, "The design and performance of IceCube DeepCore," Astropart. Phys. **35**, 615.

Abbasi, R. U., *et al.* (HiRes Collaboration), 2008, "First Observation of the Greisen-Zatsepin-Kuzmin Suppression," Phys. Rev. Lett. **100**, 101101.

Abbasi, R. U., *et al.* (Telescope Array Collaboration), 2019, "Mass composition of ultrahigh-energy cosmic rays with the Telescope Array Surface Detector data," Phys. Rev. D **99**, 022002.

Abbott, B. P., *et al.* (LIGO Scientific and Virgo Collaborations), 2016, "GW151226: Observation of Gravitational Waves from a 22-Solar-Mass Binary Black Hole Coalescence," Phys. Rev. Lett. **116**, 241103; for further detections and the latest developments see the Ligo (https://www.ligo.caltech.edu/) and Virgo (https://www.virgo-gw.eu/) home pages.

Abdurashitov, J. N., *et al.* (SAGE Collaboration), 2009, "Measurement of the solar neutrino capture rate with gallium metal. III: Results for the 2002–2007 data-taking period," Phys. Rev. C **80**, 015807.

Abe, K., *et al.* (Hyper-Kamiokande Collaboration), 2018, "Hyper-Kamiokande design report," arXiv:1805.04163.

Abe, K., *et al.* (Super-Kamiokande Collaboration), 2016, "Solar neutrino measurements in Super-Kamiokande-IV," Phys. Rev. D **94**, 052010.

Abe, S., *et al.* (KamLAND Collaboration), 2011, "Measurement of the ^{8}B solar neutrino flux with the KamLAND liquid scintillator detector," Phys. Rev. C **84**, 035804.

Abe, Y., *et al.* (Double Chooz Collaboration), 2012, "Indication of Reactor $\bar{\nu}_e$ Disappearance in the Double Chooz Experiment," Phys. Rev. Lett. **108**, 131801.

Acciarri, R., *et al.* (DUNE Collaboration), 2016, "Long-Baseline Neutrino Facility (LBNF) and Deep Underground Neutrino Experiment (DUNE). Conceptual design report. Volume 4: The DUNE detectors at LBNF," arXiv:1601.02984.

Achar, C. V., *et al.*, 1965, "Detection of muons produced by cosmic ray neutrinos deep underground," Phys. Lett. **18**, 196.

Ackermann, M., *et al.*, 2019, "Astrophysics uniquely enabled by observations of high-energy cosmic neutrinos," Bull. Am. Astron. Soc. **51**, 185, https://inspirehep.net/literature/1724499.

Ackermann, M., *et al.* (Fermi-LAT Collaboration), 2012, "GeV observations of star-forming galaxies with Fermi LAT," Astrophys. J. **755**, 164.

Ackermann, M., *et al.* (Fermi-LAT Collaboration), 2016, "Resolving the Extragalactic γ-Ray Background above 50 GeV with the Fermi Large Area Telescope," Phys. Rev. Lett. **116**, 151105.

Adams, S. M., C. S. Kochanek, J. F. Beacom, M. R. Vagins, and K. Z. Stanek, 2013, "Observing the next Galactic supernova," Astrophys. J. **778**, 164.

Adams, S. M., C. S. Kochanek, J. R. Gerke, and K. Z. Stanek, 2017, "The search for failed supernovae with the Large Binocular Telescope: Constraints from 7 yr of data," Mon. Not. R. Astron. Soc. **469**, 1445.

Adamson, P., *et al.* (MINOS Collaboration), 2011, "Measurement of the Neutrino Mass Splitting and Flavor Mixing by MINOS," Phys. Rev. Lett. **106**, 181801.

Ade, P. A. R., *et al.* (Planck Collaboration), 2016, "Planck 2015 results. XIII. Cosmological parameters," Astron. Astrophys. **594**, A13.

Adrián-Martínez, S., *et al.* (KM3Net Collaboration), 2016, "Letter of intent for KM3NeT 2.0," J. Phys. G **43**, 084001.

Agashe, K., Y. Cui, L. Necib, and J. Thaler, 2014, "(In)direct detection of boosted dark matter," J. Cosmol. Astropart. Phys. 10, 062.

Aghanim, N., *et al.* (Planck Collaboration), 2020, "Planck 2018 results. VI. Cosmological parameters," Astron. Astrophys. **641**, A6.

Agostini, M., *et al.* (Borexino Collaboration), 2018, "Comprehensive measurement of pp-chain solar neutrinos," Nature (London) **562**, 505.

Agostini, M., *et al.* (Borexino Collaboration), 2019, "First simultaneous precision spectroscopy of pp, ^{7}Be, and pep solar neutrinos with Borexino Phase-II," Phys. Rev. D **100**, 082004.

Agostini, M., *et al.* (Borexino Collaboration), 2020a, Comprehensive geoneutrino analysis with Borexino," Phys. Rev. D **101**, 012009.

Agostini, M., *et al.* (Borexino Collaboration), 2020b, "First direct experimental evidence of CNO neutrinos," arXiv:2006.15115.

Aharmim, B., *et al.* (SNO Collaboration), 2010, "Low-energy-threshold analysis of the Phase I and Phase II data sets of the Sudbury Neutrino Observatory," Phys. Rev. C **81**, 055504.

Ahlers, M., and F. Halzen, 2012, "Minimal cosmogenic neutrinos," Phys. Rev. D **86**, 083010.

Ahlers, M., and F. Halzen, 2018, "Opening a new window onto the Universe with IceCube," Prog. Part. Nucl. Phys. **102**, 73.

Ahlers, M., K. Helbing, and C. Pérez de los Heros, 2018, "Probing particle physics with IceCube," Eur. Phys. J. C **78**, 924.

Ahlers, M., and K. Murase, 2014, "Probing the Galactic origin of the IceCube excess with gamma rays," Phys. Rev. D **90**, 023010.

Ahn, J. K., *et al.* (RENO Collaboration), 2012, "Observation of Reactor Electron Antineutrinos Disappearance in the RENO Experiment," Phys. Rev. Lett. **108**, 191802.

Ajello, M., *et al.*, 2012, "The luminosity function of Fermi-detected flat-spectrum radio quasars," Astrophys. J. **751**, 108.

Ajello, M., *et al.*, 2014, "The cosmic evolution of Fermi BL Lacertae objects," Astrophys. J. **780**, 73.

Aker, M., *et al.* (KATRIN Collaboration), 2019, "Improved Upper Limit on the Neutrino Mass from a Direct Kinematic Method by KATRIN," Phys. Rev. Lett. **123**, 221802.

Akhmedov, E., 2019, "Relic neutrino detection through angular correlations in inverse β-decay," J. Cosmol. Astropart. Phys. 09, 031.

Albert, A., *et al.* (ANTARES and IceCube Collaborations), 2018, "Joint constraints on Galactic diffuse neutrino emission from the ANTARES and IceCube neutrino telescopes," Astrophys. J. **868**, L20.

Alekseev, E. N., L. N. Alekseeva, I. V. Krivosheina, and V. I. Volchenko, 1988, "Detection of the neutrino signal from SN1987A in the LMC using the INR Baksan underground scintillation telescope," Phys. Lett. B **205**, 209.

Allard, D., M. Ave, N. Busca, M. A. Malkan, A. V. Olinto, E. Parizot, F. W. Stecker, and T. Yamamoto, 2006, "Cosmogenic neutrinos from the propagation of ultrahigh energy nuclei," J. Cosmol. Astropart. Phys. 09, 005.

Allison, P., *et al.*, 2012, "Design and initial performance of the Askaryan Radio Array prototype EeV neutrino detector at the South Pole," Astropart. Phys. **35**, 457.

Aloisio, R., D. Boncioli, A. di Matteo, A. F. Grillo, S. Petrera, and F. Salamida, 2015, "Cosmogenic neutrinos and ultra-high energy cosmic ray models," J. Cosmol. Astropart. Phys. 10, 006.

Alonso, J. R., *et al.*, 2014, "Advanced scintillator detector concept (ASDC): A concept paper on the physics potential of water-based liquid scintillator," arXiv:1409.5864.

Alpher, R. A., H. Bethe, and G. Gamow, 1948, "The origin of chemical elements," Phys. Rev. **73**, 803.

Alpher, R. A., and R. Herman, 1948, "Evolution of the Universe," Nature (London) **162**, 774.

Alpher, R. A., and R. Herman, 1988, "Reflections on early work on big bang cosmology," Phys. Today **41**, No. 8, 24.

Alpher, R. A., and R. C. Herman, 1950, "Theory of the origin and relative abundance distribution of the elements," Rev. Mod. Phys. **22**, 153.

Altmann, M., *et al.* (GNO Collaboration), 2005, "Complete results for five years of GNO solar neutrino observations," Phys. Lett. B **616**, 174.

Álvarez-Muñiz, J., *et al.* (GRAND Collaboration), 2020, "The Giant Radio Array for Neutrino Detection (GRAND): Science and design," Sci. China Phys. Mech. Astron. **63**, 219501.

Alves Batista, R., R. M. de Almeida, B. Lago, and K. Kotera, 2019, "Cosmogenic photon and neutrino fluxes in the Auger era," J. Cosmol. Astropart. Phys. 01, 002.

An, F., *et al.* (JUNO Collaboration), 2016, "Neutrino physics with JUNO," J. Phys. G **43**, 030401.

An, F. P., *et al.* (Daya Bay Collaboration), 2012, "Observation of Electron-Antineutrino Disappearance at Daya Bay," Phys. Rev. Lett. **108**, 171803.

Anchordoqui, L. A., 2019, "Ultra-high-energy cosmic rays," Phys. Rep. **801**, 1.

Anderson, M., *et al.* (SNO+ Collaboration), 2019, "Measurement of the ^{8}B solar neutrino flux in SNO+ with very low backgrounds," Phys. Rev. D **99**, 012012.

Ando, S., and J. F. Beacom, 2005, "Revealing the Supernova–Gamma-Ray Burst Connection with TeV Neutrinos," Phys. Rev. Lett. **95**, 061103.

Ando, S., and K. Sato, 2004, "Relic neutrino background from cosmological supernovae," New J. Phys. **6**, 170.

Ando, S., I. Tamborra, and F. Zandanel, 2015, "Tomographic Constraints on High-Energy Neutrinos of Hadronuclear Origin," Phys. Rev. Lett. **115**, 221101.

Andringa, S., *et al.* (SNO+ Collaboration), 2016, "Current status and future prospects of the SNO+ experiment," Adv. High Energy Phys. **2016**, 6194250.

Antusch, S., J. P. Baumann, and E. Fernández-Martínez, 2009, "Non-standard neutrino interactions with matter from physics beyond the Standard Model," Nucl. Phys. **B810**, 369.

Apollonio, M., *et al.* (CHOOZ Collaboration), 1999, "Limits on neutrino oscillations from the CHOOZ experiment," Phys. Lett. B **466**, 415.

Araki, T., *et al.*, 2005a, "Experimental investigation of geologically produced antineutrinos with KamLAND," Nature (London) **436**, 499.

Araki, T., *et al.* (KamLAND Collaboration), 2005b, "Measurement of Neutrino Oscillation with KamLAND: Evidence of Spectral Distortion," Phys. Rev. Lett. **94**, 081801.

Arenz, M., *et al.* (KATRIN Collaboration), 2018, "First transmission of electrons and ions through the KATRIN beamline," J. Instrum. **13**, P04020; for the latest status see the KATRIN home page, https://www.katrin.kit.edu/.

Argüelles, C. A., G. de Wasseige, A. Fedynitch, and B. J. P. Jones, 2017, "Solar atmospheric neutrinos and the sensitivity floor for solar dark matter annihilation searches," J. Cosmol. Astropart. Phys. 07, 024.

Arteaga, M., E. Bertuzzo, Y. F. Perez-Gonzalez, and R. Zukanovich Funchal, 2017, "Impact of beyond the standard model physics in the detection of the cosmic neutrino background," J. High Energy Phys. 09, 124.

Arushanova, E., and A. R. Back (SNO+ Collaboration), 2017, "Physics capabilities of the SNO+ experiment," J. Phys. Conf. Ser. **888**, 012245.

Ashtari Esfahani, A., *et al.* (Project 8 Collaboration), 2017, "Determining the neutrino mass with cyclotron radiation emission spectroscopy—Project 8," J. Phys. G **44**, 054004.

Askins, M., *et al.* (THEIA Collaboration), 2020, "THEIA: An advanced optical neutrino detector," Eur. Phys. J. C **80**, 416.

Asplund, M., N. Grevesse, A. J. Sauval, and P. Scott, 2009, "The chemical composition of the Sun," Annu. Rev. Astron. Astrophys. **47**, 481.

Atoyan, A., and C. D. Dermer, 2001, "High-Energy Neutrinos from Photomeson Processes in Blazars," Phys. Rev. Lett. **87**, 221102.

Badnell, N. R., M. A. Bautista, K. Butler, F. Delahaye, C. Mendoza, P. Palmeri, C. J. Zeippen, and M. J. Seaton, 2005, "Updated opacities from the Opacity Project," Mon. Not. R. Astron. Soc. **360**, 458.

Baerwald, P., S. Hummer, and W. Winter, 2012, "Systematics in the interpretation of aggregated neutrino flux limits and flavor ratios from gamma-ray bursts," Astropart. Phys. **35**, 508.

Bahcall, J. N., 1989, *Neutrino Astrophysics* (Cambridge University Press, Cambridge, England).

Bahcall, J. N., 1990, "Line versus continuum solar neutrinos," Phys. Rev. D **41**, 2964.

Bahcall, J. N., 1993, "Central Temperature of the Sun Can Be Measured via the ^{7}Be Solar Neutrino Line," Phys. Rev. Lett. **71**, 2369.

Bahcall, J. N., 1997, "Gallium solar neutrino experiments: Absorption cross-sections, neutrino spectra, and predicted event rates," Phys. Rev. C **56**, 3391.

Bahcall, J. N., E. Lisi, D. E. Alburger, L. De Braeckeleer, S. J. Freedman, and J. Napolitano, 1996, "Standard neutrino spectrum from ^{8}B decay," Phys. Rev. C **54**, 411.

Bahcall, J. N., and A. Ulmer, 1996, "Temperature dependence of solar neutrino fluxes," Phys. Rev. D **53**, 4202.

Bahcall, J. N., and R. K. Ulrich, 1988, "Solar models, neutrino experiments, and helioseismology," Rev. Mod. Phys. **60**, 297.

Bahcall, J. N., and E. Waxman, 2001, "High-energy astrophysical neutrinos: The upper bound is robust," Phys. Rev. D **64**, 023002.
Balantekin, A. B., and B. Kayser, 2018, "On the properties of neutrinos," Annu. Rev. Nucl. Part. Sci. **68**, 313.
Baldoncini, M., I. Callegari, G. Fiorentini, F. Mantovani, B. Ricci, V. Strati, and G. Xhixha, 2015, "Reference worldwide model for antineutrinos from reactors," Phys. Rev. D **91**, 065002.
Baracchini, E., *et al.* (PTOLEMY Collaboration), 2018, "PTOLEMY: A proposal for thermal relic detection of nassive neutrinos and directional detection of MeV dark matter," arXiv:1808.01892.
Barger, V. D., F. Halzen, D. Hooper, and C. Kao, 2002, "Indirect search for neutralino dark matter with high-energy neutrinos," Phys. Rev. D **65**, 075022.
Barinov, V., B. Cleveland, V. Gavrin, D. Gorbunov, and T. Ibragimova, 2018, "Revised neutrino-gallium cross section and prospects of BEST in resolving the gallium anomaly," Phys. Rev. D **97**, 073001.
Barwick, S. W., *et al.* (ARIANNA Collaboration), 2015, "A first search for cosmogenic neutrinos with the ARIANNA Hexagonal Radio Array," Astropart. Phys. **70**, 12.
Basu, S., and H. M. Antia, 1997, "Seismic measurement of the depth of the solar convection zone, Mon. Not. R. Astron. Soc. **287**, 189.
Basu, S., and H. M. Antia, 2004, "Constraining solar abundances using helioseismology," Astrophys. J. **606**, L85.
Battistoni, G., A. Ferrari, T. Montaruli, and P. R. Sala, 2005, "The atmospheric neutrino flux below 100 MeV: The FLUKA results," Astropart. Phys. **23**, 526.
Bays, K., *et al.* (Super-Kamiokande Collaboration), 2012, "Supernova relic neutrino search at Super-Kamiokande," Phys. Rev. D **85**, 052007.
Beacom, J. F., 2010, "The diffuse supernova neutrino background," Annu. Rev. Nucl. Part. Sci. **60**, 439.
Beacom, J. F., and N. F. Bell, 2002, "Do solar neutrinos decay?," Phys. Rev. D **65**, 113009.
Beacom, J. F., N. F. Bell, D. Hooper, S. Pakvasa, and T. J. Weiler, 2003, "Decay of High-Energy Astrophysical Neutrinos," Phys. Rev. Lett. **90**, 181301.
Beacom, J. F., R. N. Boyd, and A. Mezzacappa, 2000, "Technique for Direct eV-Scale Measurements of the Mu and Tau Neutrino Masses Using Supernova Neutrinos," Phys. Rev. Lett. **85**, 3568.
Beacom, J. F., and M. R. Vagins, 2004, "GADZOOKS! Antineutrino Spectroscopy with Large Water Cherenkov Detectors," Phys. Rev. Lett. **93**, 171101.
Beacom, J. F., *et al.* (Jinping Collaboration), 2017, "Physics prospects of the Jinping neutrino experiment," Chin. Phys. C **41**, 023002.
Bechtol, K., M. Ahlers, M. Di Mauro, M. Ajello, and J. Vandenbroucke, 2017, "Evidence against star-forming galaxies as the dominant source of IceCube neutrinos," Astrophys. J. **836**, 47.
Becker, J. K., 2008, "High-energy neutrinos in the context of multimessenger physics," Phys. Rep. **458**, 173.
Becker, J. K., P. L. Biermann, and W. Rhode, 2005, "The diffuse neutrino flux from FR-II radio galaxies and blazars: A source property based estimate," Astropart. Phys. **23**, 355.
Bellini, G., A. Ianni, L. Ludhova, F. Mantovani, and W. F. McDonough, 2013, "Geo-neutrinos," Prog. Part. Nucl. Phys. **73**, 1.
Bellini, G., *et al.* (Borexino Collaboration), 2011, "Study of solar and other unknown anti-neutrino fluxes with Borexino at LNGS," Phys. Lett. B **696**, 191.
Bellini, G., *et al.* (Borexino Collaboration), 2014, "Final results of Borexino Phase-I on low-energy solar neutrino spectroscopy," Phys. Rev. D **89**, 112007.
Berezinsky, V. S., and G. T. Zatsepin, 1969, "Cosmic rays at ultrahigh energies (neutrino?)," Phys. Lett. **28B**, 423.
Bergevin, M., *et al.*, 2019, "Applied Antineutrino Physics 2018 proceedings," arXiv:1911.06834.
Bergström, J., M. C. Gonzalez-Garcia, M. Maltoni, C. Peña-Garay, A. M. Serenelli, and N. Song, 2016, "Updated determination of the solar neutrino fluxes from solar neutrino data," J. High Energy Phys. 03, 132.
Berryman, J. M., and P. Huber, 2020, "Reevaluating reactor antineutrino anomalies with updated flux predictions," Phys. Rev. D **101**, 015008.
Bethe, H., and R. Peierls, 1934, "The 'neutrino,' " Nature (London) **133**, 532.
Bethe, H. A., 1990, "Supernova mechanisms," Rev. Mod. Phys. **62**, 801.
Bethe, H. A., and J. R. Wilson, 1985, "Revival of a stalled supernova shock by neutrino heating," Astrophys. J. **295**, 14.
Betts, S., *et al.*, 2013, "Development of a relic neutrino detection experiment at PTOLEMY: Princeton Tritium Observatory for Light, Early-Universe, Massive-Neutrino Yield," arXiv:1307.4738.
Bhattacharya, A., R. Enberg, Y. S. Jeong, C. S. Kim, M. H. Reno, I. Sarcevic, and A. Stasto, 2016, "Prompt atmospheric neutrino fluxes: Perturbative QCD models and nuclear effects," J. High Energy Phys. 11, 167.
Bhattacharya, A., M. H. Reno, and I. Sarcevic, 2014, "Reconciling neutrino flux from heavy dark matter decay and recent events at IceCube," J. High Energy Phys. 06, 110.
Biggio, C., M. Blennow, and E. Fernández-Martínez, 2009, "General bounds on non-standard neutrino interactions," J. High Energy Phys. 08, 090.
Bionta, R. M., *et al.*, 1987, "Observation of a Neutrino Burst in Coincidence with Supernova 1987A in the Large Magellanic Cloud," Phys. Rev. Lett. **58**, 1494.
Bisnovatyi-Kogan, G. S., and Z. F. Seidov, 1982, "Medium-energy neutrinos in the Universe," Astron. Zh. **59**, 213–223 [Sov. Astron. **26**, 132 (1982)], https://ui.adsabs.harvard.edu/abs/1982SvA....26..132B/abstract.
Blancard, C., P. Cossé, and G. Faussurier, 2012, "Solar mixture opacity calculations using detailed configuration and level accounting treatments," Astrophys. J. **745**, 10.
Blondin, J. M., A. Mezzacappa, and C. DeMarino, 2003, "Stability of standing accretion shocks, with an eye toward core collapse supernovae," Astrophys. J. **584**, 971.
Boehm, F., *et al.*, 2001, "Final results from the Palo Verde neutrino oscillation experiment," Phys. Rev. D **64**, 112001.
Bollig, R., H.-T. Janka, A. Lohs, G. Martínez-Pinedo, C. J. Horowitz, and T. Melson, 2017, "Muon Creation in Supernova Matter Facilitates Neutrino-Driven Explosions," Phys. Rev. Lett. **119**, 242702.
Boran, S., S. Desai, and E. O. Kahya, 2019, "Constraints on differential Shapiro delay between neutrinos and photons from IceCube-170922A," Eur. Phys. J. C **79**, 185.
Böser, S., C. Buck, C. Giunti, J. Lesgourgues, L. Ludhova, S. Mertens, A. Schukraft, and M. Wurm, 2020, "Status of light sterile neutrino searches," Prog. Part. Nucl. Phys. **111**, 103736.
Botella, F. J., C. S. Lim, and W. J. Marciano, 1987, "Radiative corrections to neutrino indices of refraction," Phys. Rev. D **35**, 896.
Boucenna, S. M., M. Chianese, G. Mangano, G. Miele, S. Morisi, O. Pisanti, and E. Vitagliano, 2015, "Decaying leptophilic dark matter at IceCube," J. Cosmol. Astropart. Phys. 12, 055.
Brinckmann, T., D. C. Hooper, M. Archidiacono, J. Lesgourgues, and T. Sprenger, 2019, "The promising future of a robust cosmological neutrino mass measurement," J. Cosmol. Astropart. Phys. 01, 059.
Bruenn, S. W., 1985, "Stellar core collapse: Numerical model and infall epoch," Astrophys. J. Suppl. Ser. **58**, 771.

Buchmüller, W., R. D. Peccei, and T. Yanagida, 2005, "Leptogenesis as the origin of matter," Annu. Rev. Nucl. Part. Sci. **55**, 311.

Burrows, A., 2013, "Colloquium: Perspectives on core-collapse supernova theory," Rev. Mod. Phys. **85**, 245.

Burrows, A., D. Radice, D. Vartanyan, H. Nagakura, M. A. Skinner, and J. Dolence, 2020, "The overarching framework of core-collapse supernova explosions as revealed by 3D FORNAX simulations," Mon. Not. R. Astron. Soc. **491**, 2715.

Bustamante, M., J. F. Beacom, and K. Murase, 2017, "Testing decay of astrophysical neutrinos with incomplete information," Phys. Rev. D **95**, 063013.

Cabibbo, N., and L. Maiani, 1982, "The vanishing of order-G mechanical effects of cosmic massive neutrinos on bulk matter," Phys. Lett. **114B**, 115.

Caminata, A., S. Davini, L. Di Noto, M. Pallavicini, G. Testera, and S. Zavatarelli, 2018, "Search for geo-neutrinos and rare nuclear processes with Borexino," Int. J. Mod. Phys. A **33**, 1843009.

Capozzi, F., S. W. Li, G. Zhu, and J. F. Beacom, 2019, "DUNE as the Next-Generation Solar Neutrino Experiment," Phys. Rev. Lett. **123**, 131803.

Capozzi, F., E. Lisi, A. Marrone, and A. Palazzo, 2018, "Current unknowns in the three neutrino framework," Prog. Part. Nucl. Phys. **102**, 48.

Cappellaro, E., R. Evans, and M. Turatto, 1999, "A new determination of supernova rates and a comparison with indicators for galactic star formation," Astron. Astrophys. **351**, 459, http://articles.adsabs.harvard.edu/abs/1999A%26A...351..459C.

Cappellaro, E., and M. Turatto, 2001, "Supernova types and rates," Astrophys. Space Sci. Libr. **264**, 199.

Cassé, M., P. Goret, and C. J. Cesarsky, 1975, "Atomic properties of the elements and cosmic ray composition at the source," in *Proceedings of the 14th International Cosmic Ray Conference (ICRC 1975), Munich, 1975*, p. 646, https://ui.adsabs.harvard.edu/abs/1975ICRC....2..646C.

Castorina, E., U. Franca, M. Lattanzi, J. Lesgourgues, G. Mangano, A. Melchiorri, and S. Pastor, 2012, "Cosmological lepton asymmetry with a nonzero mixing angle θ_{13}," Phys. Rev. D **86**, 023517.

Cerdeño, D. G., J. H. Davis, M. Fairbairn, and A. C. Vincent, 2018, "CNO neutrino grand prix: The race to solve the solar metallicity problem," J. Cosmol. Astropart. Phys. 04, 037.

Chakraborty, S., R. Hansen, I. Izaguirre, and G. Raffelt, 2016, "Collective neutrino flavor conversion: Recent developments," Nucl. Phys. **B908**, 366.

Chen, H. H., 1985, "Direct Approach to Resolve the Solar-Neutrino Problem," Phys. Rev. Lett. **55**, 1534.

Cheng, J.-P., *et al.*, 2017, "The China Jinping Underground Laboratory and its early science," Annu. Rev. Nucl. Part. Sci. **67**, 231–251.

Chianese, M., D. F. Fiorillo, G. Miele, S. Morisi, and O. Pisanti, **2019**, "Decaying dark matter at IceCube and its signature on high energy gamma experiments," J. Cosmol. Astropart. Phys. 11, 046.

Chianese, M., G. Miele, S. Morisi, and E. Vitagliano, 2016, "Low energy IceCube data and a possible dark matter related excess," Phys. Lett. B **757**, 251.

Cholis, I., D. Hooper, and T. Linden, 2016, "A predictive analytic model for the solar modulation of cosmic rays," Phys. Rev. D **93**, 043016.

Cicenas, B., and N. Solomey (HANOHANO Collaboration), 2012, "The HANOHANO detector and ongoing research and development," Phys. Procedia **37**, 1324.

Cirelli, M., N. Fornengo, T. Montaruli, I. A. Sokalski, A. Strumia, and F. Vissani, 2005, "Spectra of neutrinos from dark matter annihilations," Nucl. Phys. **B727**, 99; **B790**, 338(E) (2008).

Clayton, D. D., 1983, *Principles of Stellar Evolution and Nucleosynthesis* (Chicago University Press, Chicago).

Cleveland, B. T., T. Daily, R. Davis, Jr., J. R. Distel, K. Lande, C. K. Lee, P. S. Wildenhain, and J. Ullman, 1998, "Measurement of the solar electron neutrino flux with the Homestake chlorine detector," Astrophys. J. **496**, 505.

Cocco, A. G., A. Ereditato, G. Fiorillo, G. Mangano, and V. Pettorino, 2004, "Supernova relic neutrinos in liquid argon detectors," J. Cosmol. Astropart. Phys. 12, 002.

Cocco, A. G., G. Mangano, and M. Messina, 2007, "Probing low energy neutrino backgrounds with neutrino capture on beta decaying nuclei," J. Cosmol. Astropart. Phys. 06, 015.

Cohen, T., K. Murase, N. L. Rodd, B. R. Safdi, and Y. Soreq, 2017, "γ-Ray Constraints on Decaying Dark Matter and Implications for IceCube," Phys. Rev. Lett. **119**, 021102.

Colgan, J., D. P. Kilcrease, N. H. Magee, M. E. Sherrill, J. Abdallah, Jr., P. Hakel, C. J. Fontes, J. A. Guzik, and K. A. Mussack, 2016, "A new generation of Los Alamos opacity tables," Astrophys. J. **817**, 116.

Conlon, J. P., F. Day, N. Jennings, S. Krippendorf, and F. Muia, 2018, "Projected bounds on ALPs from Athena," Mon. Not. R. Astron. Soc. **473**, 4932.

Conrad, J. M., and M. H. Shaevitz, 2018, "Sterile neutrinos: An introduction to experiments," in *The State of the Art of Neutrino Physics: A Tutorial for Graduate Students and Young Researchers*, Advanced Series on Directions in High Energy Physics Vol. 28, edited by A. Ereditato (World Scientific, Singapore), p. 391, https://www.worldscientific.com/worldscibooks/10.1142/10600.

Cowan, C., F. Reines, F. Harrison, E. Anderson, and F. Hayes, 1953, "Large liquid scintillation detectors," Phys. Rev. **90**, 493.

Cribier, M., M. Spiro, and D. Vignaud, 1995, *La Lumière des Neutrinos* (Editions du Seuil, Paris).

Cyburt, R. H., B. D. Fields, K. A. Olive, and T.-H. Yeh, 2016, "Big bang nucleosynthesis: Present status," Rev. Mod. Phys. **88**, 015004.

Dai, Z. G., and T. Lu, 2001, "Neutrino afterglows and progenitors of gamma-ray bursts," Astrophys. J. **551**, 249.

Dartois, E., *et al.*, 2015, "Swift heavy ion modifications of astrophysical water ice," Nucl. Instrum. Methods Phys. Res., Sect. A **365**, 472.

Davidson, S., E. Nardi, and Y. Nir, 2008, "Leptogenesis," Phys. Rep. **466**, 105.

Davidson, S., C. Peña-Garay, N. Rius, and A. Santamaria, 2003, "Present and future bounds on nonstandard neutrino interactions," J. High Energy Phys. 03, 011.

Davis, Jr., R., D. S. Harmer, and K. C. Hoffman, 1968, "Search for Neutrinos from the Sun," Phys. Rev. Lett. **20**, 1205.

de Nolfo, G. A., *et al.*, 2006, "Observations of the Li, Be, and B isotopes and constraints on cosmic-ray propagation," Adv. Space Res. **38**, 1558.

de Rham, C., J. T. Deskins, A. J. Tolley, and S.-Y. Zhou, 2017, "Graviton mass bounds," Rev. Mod. Phys. **89**, 025004.

de Salas, P. F., D. V. Forero, C. A. Ternes, M. Tórtola, and J. W. F. Valle, 2018, "Status of neutrino oscillations 2018: 3σ hint for normal mass ordering and improved *CP* sensitivity," Phys. Lett. B **782**, 633.

de Salas, P. F., S. Gariazzo, J. Lesgourgues, and S. Pastor, 2017, "Calculation of the local density of relic neutrinos," J. Cosmol. Astropart. Phys. 09, 034.

de Salas, P. F., and S. Pastor, 2016, "Relic neutrino decoupling with flavour oscillations revisited," J. Cosmol. Astropart. Phys. 07, 051.

Denton, P. B., D. Marfatia, and T. J. Weiler, 2017, "The galactic contribution to IceCube's astrophysical neutrino flux," J. Cosmol. Astropart. Phys. 08, 033.

Denton, P. B., H. Minakata, and S. J. Parke, 2016, "Compact perturbative expressions for neutrino oscillations in matter," J. High Energy Phys. 06, 051.

Denton, P. B., and I. Tamborra, 2018a, "Exploring the properties of choked gamma-ray bursts with IceCube's high-energy neutrinos," Astrophys. J. **855**, 37.

Denton, P. B., and I. Tamborra, 2018b, "Invisible Neutrino Decay Could Resolve IceCube's Track and Cascade Tension," Phys. Rev. Lett. **121**, 121802.

Denton, P. B., and I. Tamborra, 2018c, "The bright and choked gamma-ray burst contribution to the IceCube and ANTARES low-energy excess," J. Cosmol. Astropart. Phys. 04,

Desai, S., and E. O. Kahya, 2018, "Galactic Shapiro delay to the Crab pulsar and limit on weak equivalence principle violation," Eur. Phys. J. C **78**, 86.

Dighe, A. S., and A. Yu. Smirnov, 2000, "Identifying the neutrino mass spectrum from the neutrino burst from a supernova," Phys. Rev. D **62**, 033007.

Dole, H., G. Lagache, J.-L. Puget, K. I. Caputi, N. Fernández-Conde, E. Le Floc'h, C. Papovich, P. G. Pérez-González, G. H. Rieke, and M. Blaylock, 2006, "The cosmic infrared background resolved by Spitzer: Contributions of mid-infrared galaxies to the far-infrared background," Astron. Astrophys. **451**, 417.

Dolgov, A. D., 2002, "Neutrinos in cosmology," Phys. Rep. **370**, 333.

Dolgov, A. D., S. H. Hansen, S. Pastor, S. T. Petcov, G. G. Raffelt, and D. V. Semikoz, 2002, "Cosmological bounds on neutrino degeneracy improved by flavor oscillations," Nucl. Phys. **B632**, 363.

Domcke, V., and M. Spinrath, 2017, "Detection prospects for the cosmic neutrino background using laser interferometers," J. Cosmol. Astropart. Phys. 06, 055.

Domogatskii, G. V., 1984, "The isotropic electron antineutrino flux—A clue to the rate of stellar gravitational collapse in the Universe," Astron. Zh. **61**, 51–52 [Sov. Astron. **28**, 30 (1984)].

Donini, A., S. Palomares-Ruiz, and J. Salvado, 2019, "Neutrino tomography of Earth," Nat. Phys. **15**, 37.

Duan, H., G. M. Fuller, and Y.-Z. Qian, 2010, "Collective neutrino oscillations," Annu. Rev. Nucl. Part. Sci. **60**, 569.

Duda, G., G. Gelmini, and S. Nussinov, 2001, "Expected signals in relic neutrino detectors," Phys. Rev. D **64**, 122001.

Dutta, B., and L. E. Strigari, 2019, "Neutrino physics with dark matter detectors," Annu. Rev. Nucl. Part. Sci. **69**, 137.

Dye, S., 2012, "Geoneutrinos and the radioactive power of the Earth," Rev. Geophys. **50**, 3007.

Dziewonski, A. M., and D. L. Anderson, 1981, "Preliminary reference Earth model," Phys. Earth Planet. Inter. **25**, 297.

Eder, G., 1966, "Terrestrial neutrinos," Nucl. Phys. **78**, 657.

Edsjö, J., J. Elevant, R. Enberg, and C. Niblaeus, 2017, "Neutrinos from cosmic ray interactions in the Sun," J. Cosmol. Astropart. Phys. 06, 033.

Eguchi, K., *et al.* (KamLAND Collaboration), 2003, "First Results from KamLAND: Evidence for Reactor Antineutrino Disappearance," Phys. Rev. Lett. **90**, 021802.

Elewyck Van, V., 2019, "The Antares and KM3NeT neutrino telescopes: Status and outlook for acoustic studies," Eur. Phys. J. Web Conf. **216**, 01004.

Ellis, J., H.-T. Janka, N. E. Mavromatos, A. S. Sakharov, and E. K. G. Sarkisyan, 2012, "Prospective constraints on neutrino masses from a core-collapse supernova," Phys. Rev. D **85**, 105028.

Ellis, J., N. E. Mavromatos, A. S. Sakharov, and E. K. Sarkisyan-Grinbaum, 2019, "Limits on neutrino Lorentz violation from multi-messenger observations of TXS 0506+056," Phys. Lett. B **789**, 352.

Enberg, R., M. H. Reno, and I. Sarcevic, 2008, "Prompt neutrino fluxes from atmospheric charm," Phys. Rev. D **78**, 043005.

Enomoto, S., 2005, "Neutrino geophysics and observation of geo-neutrinos at KamLAND," Ph.D. thesis (Tohoku University); online version and input tables at https://www.awa.tohoku.ac.jp/~sanshiro/research/.

Enomoto, S., E. Ohtani, K. Inoue, and A. Suzuki, 2007, "Neutrino geophysics with KamLAND and future prospects," Earth Planet. Sci. Lett. **258**, 147–159.

Ertl, T., H.-T. Janka, S. E. Woosley, T. Sukhbold, and M. Ugliano, 2016, "A two-parameter criterion for classifying the explodability of massive stars by the neutrino-driven mechanism," Astrophys. J. **818**, 124.

Esmaili, A., and P. D. Serpico, 2013, "Are IceCube neutrinos unveiling PeV-scale decaying dark matter?," J. Cosmol. Astropart. Phys. 11, 054.

Esteban, I., M. C. Gonzalez-Garcia, M. Maltoni, I. Martinez-Soler, and T. Schwetz, 2017, "Updated fit to three neutrino mixing: Exploring the accelerator-reactor complementarity," J. High Energy Phys. 01, 087; for the latest results see the NuFIT home page, http://www.nu-fit.org/.

Estienne, M., *et al.*, 2019, "Updated Summation Model: An Improved Agreement with the Daya Bay Antineutrino Fluxes," Phys. Rev. Lett. **123**, 022502.

Fan, J., and M. Reece, 2013, "*In wino veritas*? Indirect searches shed light on neutralino dark matter," J. High Energy Phys. 10, 124.

Fang, K., and B. D. Metzger, 2017, "High-energy neutrinos from millisecond magnetars formed from the merger of binary neutron stars," Astrophys. J. **849**, 153.

Fang, K., *et al.*, 2018, "The Giant Radio Array for Neutrino Detection (GRAND): Present and perspectives," Proc. Sci. ICRC2017, 996 [arXiv:1708.05128].

Farzan, Y., and A. Yu. Smirnov, 2008, "Coherence and oscillations of cosmic neutrinos," Nucl. Phys. **B805**, 356.

Fedynitch, A., J. Becker Tjus, and P. Desiati, 2012, "Influence of hadronic interaction models and the cosmic ray spectrum on the high energy atmospheric muon and neutrino flux," Phys. Rev. D **86**, 114024.

Feldstein, B., A. Kusenko, S. Matsumoto, and T. T. Yanagida, 2013, "Neutrinos at IceCube from heavy decaying dark matter," Phys. Rev. D **88**, 015004.

Feyereisen, M. R., I. Tamborra, and S. Ando, 2017, "One-point fluctuation analysis of the high-energy neutrino sky," J. Cosmol. Astropart. Phys. 03, 057.

Fiorentini, G., M. Lissia, and F. Mantovani, 2007, "Geo-neutrinos and Earth's interior," Phys. Rep. **453**, 117.

Fischer, T., S. C. Whitehouse, A. Mezzacappa, F.-K. Thielemann, and M. Liebendörfer, 2010, "Protoneutron star evolution and the neutrino driven wind in general relativistic neutrino radiation hydrodynamics simulations," Astron. Astrophys. **517**, A80.

Fong, C. S., H. Minakata, B. Panes, and R. Zukanovich Funchal, 2015, "Possible interpretations of IceCube high-energy neutrino events," J. High Energy Phys. 02, 189.

Fornasa, M., and M. A. Sánchez-Conde, 2015, "The nature of the diffuse gamma-ray background," Phys. Rep. **598**, 1.

Fryer, C. L., 2009, "Neutrinos from fallback onto newly formed neutron stars," Astrophys. J. **699**, 409.

Fukuda, S., *et al.* (Super-Kamiokande Collaboration), 2001, "Solar ^8B and hep Neutrino Measurements from 1258 Days of Super-Kamiokande Data," Phys. Rev. Lett. **86**, 5651.

Fukuda, Y., *et al.* (Kamiokande Collaboration), 1996, "Solar Neutrino Data Covering Solar Cycle 22," Phys. Rev. Lett. **77**, 1683.
Fukuda, Y., *et al.* (Super-Kamiokande Collaboration), 1998, "Evidence for Oscillation of Atmospheric Neutrinos," Phys. Rev. Lett. **81**, 1562.
Fukugita, M., and T. Yanagida, 1986, "Baryogenesis without grand unification," Phys. Lett. B **174**, 45.
Funcke, L., G. Raffelt, and E. Vitagliano, 2020, "Distinguishing Dirac and Majorana neutrinos by their decays via Nambu-Goldstone bosons in the gravitational-anomaly model of neutrino masses," Phys. Rev. D **101**, 015025.
Furuta, H., *et al.*, 2012, "A study of reactor neutrino monitoring at the experimental fast reactor JOYO," Nucl. Instrum. Methods Phys. Res., Sect. A **662**, 90.
Gaisser, T., and A. Karle, 2017, Eds., *Neutrino Astronomy* (World Scientific, Singapore).
Gaisser, T. K., 2019, "Atmospheric neutrinos," arXiv:1910.08851.
Gaisser, T. K., R. Engel, and E. Resconi, 2016, *Cosmic Rays and Particle Physics* (Cambridge University Press, Cambridge, England).
Gaisser, T. K., and M. Honda, 2002, "Flux of atmospheric neutrinos," Annu. Rev. Nucl. Part. Sci. **52**, 153.
Galanti, G., and M. Roncadelli, 2018, "Extragalactic photon–axion-like particle oscillations up to 1000 TeV," J. High Energy Astrophys. **20**, 1.
Gamow, G., 1946, "Expanding Universe and the origin of elements," Phys. Rev. **70**, 572.
Gando, A., *et al.* (KamLAND Collaboration), 2015, "^{7}Be solar neutrino measurement with KamLAND," Phys. Rev. C **92**, 055808.
Gando, A., *et al.* (KamLAND Collaboration), 2012, "A study of extraterrestrial antineutrino sources with the KamLAND detector," Astrophys. J. **745**, 193.
Gando, A., *et al.* (KamLAND Collaboration), 2013, "Reactor on-off antineutrino measurement with KamLAND," Phys. Rev. D **88**, 033001.
Garzelli, M., S. Moch, and G. Sigl, 2015, "Lepton fluxes from atmospheric charm revisited," J. High Energy Phys. 10, 115.
Garzelli, M. V., S. Moch, O. Zenaiev, A. Cooper-Sarkar, A. Geiser, K. Lipka, R. Placakyte, and G. Sigl (PROSA Collaboration), 2017, "Prompt neutrino fluxes in the atmosphere with PROSA parton distribution functions," J. High Energy Phys. 05, 004.
Gelmini, G., and J. Valle, 1984, "Fast invisible neutrino decays," Phys. Lett. **142B**, 181.
George, J. S., *et al.*, 2009, "Elemental composition and energy spectra of galactic cosmic rays during solar cycle 23," Astrophys. J. **698**, 1666.
Ghisellini, G., C. Righi, L. Costamante, and F. Tavecchio, 2017, "The Fermi blazar sequence," Mon. Not. R. Astron. Soc. **469**, 255.
Giunti, C., and C. W. Kim, 2007, *Fundamentals of Neutrino Physics and Astrophysics* (Oxford University Press, New York).
Giunti, C., and T. Lasserre, 2019, "eV-scale sterile neutrinos," Annu. Rev. Nucl. Part. Sci. **69**, 163.
Giunti, C., and M. Laveder, 2011, "Statistical significance of the gallium anomaly," Phys. Rev. C **83**, 065504.
Giunti, C., and A. Studenikin, 2015, "Neutrino electromagnetic interactions: A window to new physics," Rev. Mod. Phys. **87**, 531.
Glashow, S. L., 1960, "Resonant scattering of antineutrinos," Phys. Rev. **118**, 316.
Gleeson, L. J., and W. I. Axford, 1968, "Solar modulation of galactic cosmic rays," Astrophys. J. **154**, 1011.
Goldhaber, A. S., and M. M. Nieto, 2010, "Photon and graviton mass limits," Rev. Mod. Phys. **82**, 939.
Gondolo, P., G. Ingelman, and M. Thunman, 1996, "Charm production and high-energy atmospheric muon and neutrino fluxes," Astropart. Phys. **5**, 309.
Gonzalez-Garcia, M., F. Halzen, M. Maltoni, and H. K. Tanaka, 2008, "Radiography of Earth's Core and Mantle with Atmospheric Neutrinos," Phys. Rev. Lett. **100**, 061802.
Greisen, K., 1966, "End to the Cosmic-Ray Spectrum?," Phys. Rev. Lett. **16**, 748.
Grenier, I. A., J. H. Black, and A. W. Strong, 2015, "The nine lives of cosmic rays in galaxies," Annu. Rev. Astron. Astrophys. **53**, 199.
Grevesse, N., and A. J. Sauval, 1998, "Standard solar composition," Space Sci. Rev. **85**, 161.
Grevesse, N., P. Scott, M. Asplund, and A. J. Sauval, 2015, "The elemental composition of the Sun. III. The heavy elements Cu to Th," Astron. Astrophys. **573**, A27.
Gribov, V. N., and B. Pontecorvo, 1969, "Neutrino astronomy and lepton charge," Phys. Lett. **28B**, 493.
Gruppioni, C., *et al.*, 2013, "The Herschel PEP/HerMES luminosity function—I. Probing the evolution of PACS selected galaxies to $z \simeq 4$," Mon. Not. R. Astron. Soc. **432**, 23.
Guedes Lang, R., H. Martínez-Huerta, and V. de Souza, 2018, "Limits on the Lorentz invariance violation from UHECR astrophysics," Astrophys. J. **853**, 23.
Guetta, D., D. Hooper, J. Àlvarez-Muńiz, F. Halzen, and E. Reuveni, 2004, "Neutrinos from individual gamma-ray bursts in the BATSE catalog," Astropart. Phys. **20**, 429.
Haft, M., G. Raffelt, and A. Weiss, 1994, "Standard and nonstandard plasma neutrino emission revisited," Astrophys. J. **425**, 222; **438**, 1017(E) (1995).
Hagmann, C., 1999, "Cosmic neutrinos and their detection," in *Proceedings of the APS Meeting, Division of Particles and Fields, Los Angeles, 1999* (American Physical Society, College Park, MD) [arXiv:astro-ph/9905258].
Halzen, F., and S. R. Klein, 2010, "IceCube: An instrument for neutrino astronomy," Rev. Sci. Instrum. **81**, 081101.
Hampel, W., *et al.* (GALLEX Collaboration), 1999, "GALLEX solar neutrino observations: Results for GALLEX IV," Phys. Lett. B **447**, 127.
Hannestad, S., 2006, "Primordial neutrinos," Annu. Rev. Nucl. Part. Sci. **56**, 137.
Haxton, W. C., and W. Lin, 2000, "The very low-energy solar flux of electron and heavy flavor neutrinos and antineutrinos," Phys. Lett. B **486**, 263.
Haxton, W. C., R. G. H. Robertson, and A. M. Serenelli, 2013, "Solar neutrinos: Status and prospects," Annu. Rev. Astron. Astrophys. **51**, 21.
Hayen, L., J. Kostensalo, N. Severijns, and J. Suhonen, 2019, "First-forbidden transitions in the reactor anomaly," Phys. Rev. C **100**, 054323.
Heinze, J., D. Boncioli, M. Bustamante, and W. Winter, 2016, "Cosmogenic neutrinos challenge the cosmic-ray proton dip model," Astrophys. J. **825**, 122.
Higaki, T., R. Kitano, and R. Sato, 2014, "Neutrinoful Universe," J. High Energy Phys. 07, 044.
Hirata, K., *et al.* (Kamiokande-II Collaboration), 1987, "Observation of a Neutrino Burst from the Supernova SN1987A," Phys. Rev. Lett. **58**, 1490.
Hirata, K. S., *et al.* (Kamiokande-II Collaboration), 1989, "Observation of ^{8}B Solar Neutrinos in the Kamiokande-II Detector," Phys. Rev. Lett. **63**, 16.
Hofmann, A., 1997, "Mantle geochemistry: The message from oceanic volcanism," Nature (London) **385**, 219.

Honda, M., T. Kajita, K. Kasahara, and S. Midorikawa, 2004, "New calculation of the atmospheric neutrino flux in a three-dimensional scheme," Phys. Rev. D **70**, 043008.

Honda, M., T. Kajita, K. Kasahara, S. Midorikawa, and T. Sanuki, 2007, "Calculation of atmospheric neutrino flux using the interaction model calibrated with atmospheric muon data," Phys. Rev. D **75**, 043006.

Honda, M., M. Sajjad Athar, T. Kajita, K. Kasahara, and S. Midorikawa, 2015, "Atmospheric neutrino flux calculation using the NRLMSISE-00 atmospheric model," Phys. Rev. D **92**, 023004.

Hopkins, A. M., and J. F. Beacom, 2006, "On the normalisation of the cosmic star formation history," Astrophys. J. **651**, 142.

Horiuchi, S., J. F. Beacom, C. S. Kochanek, J. L. Prieto, K. Z. Stanek, and T. A. Thompson, 2011, "The cosmic core-collapse supernova rate does not match the massive-star formation rate," Astrophys. J. **738**, 154.

Horiuchi, S., K. Nakamura, T. Takiwaki, K. Kotake, and M. Tanaka, 2014, "The red supergiant and supernova rate problems: Implications for core-collapse supernova physics," Mon. Not. R. Astron. Soc. **445**, L99.

Horiuchi, S., K. Sumiyoshi, K. Nakamura, T. Fischer, A. Summa, T. Takiwaki, H.-T. Janka, and K. Kotake, 2018, "Diffuse supernova neutrino background from extensive core-collapse simulations of 8–100 $M_\odot$ progenitors," Mon. Not. R. Astron. Soc. **475**, 1363.

Horowitz, C. J., and M. A. Pérez-García, 2003, "Realistic neutrino opacities for supernova simulations with correlations and weak magnetism," Phys. Rev. C **68**, 025803.

Huang, Y., V. Chubakov, F. Mantovani, R. L. Rudnick, and W. F. McDonough, 2013, "A reference Earth model for the heat-producing elements and associated geoneutrino flux," Geochem. Geophys. Geosyst. **14**, 2003.

Huber, P., 2011, "Determination of antineutrino spectra from nuclear reactors," Phys. Rev. C **84**, 024617; **85**, 029901(E) (2012).

Hüdepohl, L., B. Müller, H.-T. Janka, A. Marek, and G. G. Raffelt, 2010, "Neutrino Signal of Electron-Capture Supernovae from Core Collapse to Cooling," Phys. Rev. Lett. **104**, 251101; **105**, 249901(E) (2010).

Hummer, S., P. Baerwald, and W. Winter, 2012, "Neutrino Emission from Gamma-Ray Burst Fireballs, Revised," Phys. Rev. Lett. **108**, 231101.

Iglesias, C. A., and F. J. Rogers, 1996, "Updated OPAL opacities," Astrophys. J. **464**, 943.

In, S., and M. Jeong (IceCube Collaboration), 2018, "Solar atmospheric neutrino search with IceCube," Proc. Sci. ICRC2017, 965.

Indumathi, D. (INO Collaboration), 2015, "India-based Neutrino Observatory (INO): Physics reach and status report," AIP Conf. Proc. **1666**, 100003.

Ingelman, G., and M. Thunman, 1996, "High-energy neutrino production by cosmic ray interactions in the Sun," Phys. Rev. D **54**, 4385.

Ioannisian, A., and S. Pokorski, 2018, "Three neutrino oscillations in matter," Phys. Lett. B **782**, 641.

Iocco, F., G. Mangano, G. Miele, O. Pisanti, and P. D. Serpico, 2009, "Primordial nucleosynthesis: From precision cosmology to fundamental physics," Phys. Rep. **472**, 1.

Itoh, N., H. Hayashi, A. Nishikawa, and Y. Kohyama, 1996, "Neutrino energy loss in stellar interiors. VII. Pair, photo-, plasma, bremsstrahlung, and recombination neutrino processes," Astrophys. J. **102**, 411.

Ivanchik, A. V., and V. Yu. Yurchenko, 2018, "Relic neutrinos: Antineutrinos of primordial nucleosynthesis," Phys. Rev. D **98**, 081301(R).

Izaguirre, I., G. Raffelt, and I. Tamborra, 2017, "Fast Pairwise Conversion of Supernova Neutrinos: A Dispersion-Relation Approach," Phys. Rev. Lett. **118**, 021101.

Janka, H.-T., 2012, "Explosion mechanisms of core-collapse supernovae," Annu. Rev. Nucl. Part. Sci. **62**, 407.

Janka, H.-T., 2017, "Neutrino-driven explosions," in *Handbook of Supernovae*, edited by A. Alsabti and P. Murdin (Springer, New York), p. 1095, https://doi.org/10.1007/978-3-319-21846-5_109.

Janka, H.-T., T. Melson, and A. Summa, 2016, "Physics of core-collapse supernovae in three dimensions: A sneak preview," Annu. Rev. Nucl. Part. Sci. **66**, 341.

Jennings, Z. G., B. F. Williams, J. W. Murphy, J. J. Dalcanton, K. M. Gilbert, A. E. Dolphin, D. R. Weisz, and M. Fouesneau, 2014, "The supernova progenitor mass distributions of M31 and M33: Further evidence for an upper mass limit," Astrophys. J. **795**, 170.

Kachelrieß, M., R. Tomàs, R. Buras, H.-T. Janka, A. Marek, and M. Rampp, 2005, "Exploiting the neutronization burst of a galactic supernova," Phys. Rev. D **71**, 063003.

Kaether, F., W. Hampel, G. Heusser, J. Kiko, and T. Kirsten, 2010, "Reanalysis of the GALLEX solar neutrino flux and source experiments," Phys. Lett. B **685**, 47.

Kamionkowski, M., 1991, "Energetic neutrinos from heavy neutralino annihilation in the Sun," Phys. Rev. D **44**, 3021.

Keil, M. T., G. G. Raffelt, and H.-T. Janka, 2003, "Monte Carlo study of supernova neutrino spectra formation," Astrophys. J. **590**, 971.

Khatri, R., and R. A. Sunyaev, 2011, "Time of primordial ^{7}Be conversion into ^{7}Li, energy release and doublet of narrow cosmological neutrino lines," Astron. Lett. **37**, 367.

Kimura, S. S., K. Murase, P. Mészáros, and K. Kiuchi, 2017, "High-energy neutrino emission from short gamma-ray bursts: Prospects for coincident detection with gravitational waves," Astrophys. J. **848**, L4.

Kippenhahn, R., A. Weigert, and A. Weiss, 2012, *Stellar Structure and Evolution* (Springer, Berlin).

Kitaura, F., H.-T. Janka, and W. Hillebrandt, 2006, "Explosions of O-Ne-Mg cores, the Crab supernova, and subluminous type II-P supernovae," Astron. Astrophys. **450**, 345.

Kochanek, C. S., 2014, "Failed supernovae explain the compact remnant mass function," Astrophys. J. **785**, 28.

Kochanek, C. S., 2015, "Constraints on core collapse from the black hole mass function," Mon. Not. R. Astron. Soc. **446**, 1213.

Kopp, J., J. Liu, and X.-P. Wang, 2015, "Boosted dark matter in IceCube and at the Galactic Center," J. High Energy Phys. 04, 105.

Koshiba, M., 1992, "Observational neutrino astrophysics," Phys. Rep. **220**, 229.

Kostelecky, V. A., J. T. Pantaleone, and S. Samuel, 1993, "Neutrino oscillation in the early Universe," Phys. Lett. B **315**, 46.

Kotera, K., D. Allard, and A. Olinto, 2010, "Cosmogenic Neutrinos: Parameter space and detectabilty from PeV to ZeV," J. Cosmol. Astropart. Phys. 10, 013.

Kowalski, M., 2015, "Status of high-energy neutrino astronomy," J. Phys. Conf. Ser. **632**, 012039.

Krauss, L. M., S. L. Glashow, and D. N. Schramm, 1984, "Antineutrino astronomy and geophysics," Nature (London) **310**, 191.

Krauss, L. M., and S. Tremaine, 1988, "Test of the Weak Equivalence Principle for Neutrinos and Photons," Phys. Rev. Lett. **60**, 176.

Krief, M., A. Feigel, and D. Gazit, 2016, "Solar opacity calculations using the super-transition-array method," Astrophys. J. **821**, 45.

Labarga, L. (Super-Kamiokande Collaboration), 2018, "The SuperK-gadolinium project," Proc. Sci. EPS-HEP2017, 118.

Lacki, B. C., T. A. Thompson, E. Quataert, A. Loeb, and E. Waxman, 2011, "On the GeV and TeV detections of the starburst galaxies M82 and NGC 253," Astrophys. J. **734**, 107.

Laha, R., 2019, "Constraints on neutrino speed, weak equivalence principle violation, Lorentz invariance violation, and dual lensing from the first high-energy astrophysical neutrino source TXS 0506 +056," Phys. Rev. D **100**, 103002.

Laske, G., G. Masters, Z. Ma, and M. E. Pasyanos, 2012, "CRUST1.0: An updated global model of Earth's crust," Geophysical Research Abstracts EGU General Assembly Conference Abstracts, Vol. **14**, Report No. EGU2012, https://meetingorganizer.copernicus.org/EGU2012 /EGU2012-3743-1.pdf.

Learned, J. G., and S. Pakvasa, 1995, "Detecting ν_τ oscillations at PeV energies," Astropart. Phys. **3**, 267.

Lesgourgues, J., G. Mangano, G. Miele, and S. Pastor, 2013, *Neutrino Cosmology* (Cambridge University Press, Cambridge, England).

Lesgourgues, J., and L. Verde, 2018, "Neutrinos in cosmology," https://pdg.lbl.gov/2018/reviews/rpp2018-rev-neutrinos-in-cosmology.pdf.

Lewis, R. R., 1980, "Coherent detector for low-energy neutrinos," Phys. Rev. D **21**, 663.

Li, Y.-F., 2017, "Prospectives on direct detection of the cosmic neutrino background," J. Phys. Conf. Ser. **888**, 012146.

Liang, Y.-F., C. Zhang, Z.-Q. Xia, L. Feng, Q. Yuan, and Y.-Z. Fan, 2019, "Constraints on axion-like particle properties with very high energy gamma-ray observations of Galactic sources," J. Cosmol. Astropart. Phys. 06, 042.

Liberati, S., 2013, "Tests of Lorentz invariance: A 2013 update, Classical Quantum Gravity **30**, 133001.

Liberati, S., and L. Maccione, 2009, "Lorentz violation: Motivation and new constraints, Annu. Rev. Nucl. Part. Sci. **59**, 245.

Liebendörfer, M., A. Mezzacappa, O. E. B. Messer, G. Martinez-Pinedo, W. R. Hix, and F.-K. Thielemann, 2003, "The neutrino signal in stellar core collapse and postbounce evolution," Nucl. Phys. **A719**, C144–C152.

Lisanti, M., B. R. Safdi, and C. G. Tully, 2014, "Measuring anisotropies in the cosmic neutrino background," Phys. Rev. D **90**, 073006.

Lodders, K., 2003, "Solar system abundances and condensation temperatures of the elements," Astrophys. J. **591**, 1220.

Loeb, A., and E. Waxman, 2006, "The cumulative background of high energy neutrinos from starburst galaxies," J. Cosmol. Astropart. Phys. 05, 003.

Long, A. J., C. Lunardini, and E. Sabancilar, 2014, "Detecting non-relativistic cosmic neutrinos by capture on tritium: Phenomenology and physics potential," J. Cosmol. Astropart. Phys. 08, 038.

Longo, M. J., 1987, "Tests of relativity from SN1987A," Phys. Rev. D **36**, 3276.

Longo, M. J., 1988, "New Precision Tests of the Einstein Equivalence Principle from SN1987A," Phys. Rev. Lett. **60**, 173.

Loredo, T. J., and D. Q. Lamb, 1989, "Neutrinos from SN 1987A: Implications for cooling of the nascent neutron star and the mass of the electron antineutrino," Ann. N.Y. Acad. Sci. **571**, 601.

Loredo, T. J., and D. Q. Lamb, 2002, "Bayesian analysis of neutrinos observed from supernova SN 1987A," Phys. Rev. D **65**, 063002.

Lozza, V. (SNO+ Collaboration), 2019, "The SNO+ experiment," in *Proceedings of the 5th International Solar Neutrino Conference, Dresden, Germany, 2018* (World Scientific, Singapore), p. 313, https://doi.org/10.1142/9789811204296_0019.

Lu, J.-S., J. Cao, Y.-F. Li, and S. Zhou, 2015, "Constraining absolute neutrino masses via detection of galactic supernova neutrinos at JUNO," J. Cosmol. Astropart. Phys. 05, 044.

Ludhova, L., and S. Zavatarelli, 2013, "Studying the Earth with geoneutrinos," Adv. High Energy Phys. **2013**, 425693.

Lunardini, C., 2009, "Diffuse Neutrino Flux from Failed Supernovae," Phys. Rev. Lett. **102**, 231101.

Lunardini, C., 2016, "Diffuse supernova neutrinos at underground laboratories," Astropart. Phys. **79**, 49.

Lunardini, C., and Y. F. Perez-Gonzalez, **2020**, "Dirac and Majorana neutrino signatures of primordial black holes," J. Cosmol. Astropart. Phys. 08, 014.

Lunardini, C., and A. Yu. Smirnov, 2004, "Neutrinos from SN1987A: Flavor conversion and interpretation of results," Astropart. Phys. **21**, 703.

Maccione, L., 2013, "Low Energy Cosmic Ray Positron Fraction Explained by Charge-Sign Dependent Solar Modulation," Phys. Rev. Lett. **110**, 081101.

Madau, P., and M. Dickinson, 2014, "Cosmic star-formation history," Annu. Rev. Astron. Astrophys. **52**, 415.

Malaney, R. A., B. S. Meyer, and M. N. Butler, 1990, "Solar antineutrinos," Astrophys. J. **352**, 767.

Mantovani, F., L. Carmignani, G. Fiorentini, and M. Lissia, 2004, "Antineutrinos from the Earth: A reference model and its uncertainties," Phys. Rev. D **69**, 013001.

Marx, G., 1969, "Geophysics by neutrinos," Czech. J. Phys. B **19**, 1471–1479.

Marx, G., and N. Menyhárd, 1960, About the perspectives of neutrino astronomy, Mitt. Sternwarte Budapest **48**, 1.

Mathews, G. J., J. Hidaka, T. Kajino, and J. Suzuki, 2014, "Supernova relic neutrinos and the supernova rate problem: Analysis of uncertainties and detectability of ONeMg and failed supernovae," Astrophys. J. **790**, 115.

McDonough, W. F., and S.-s. Sun, 1995, "The composition of the Earth," Chem. Geol. **120**, 223.

Mention, G., M. Fechner, T. Lasserre, T. Mueller, D. Lhuillier, M. Cribier, and A. Letourneau, 2011, "The reactor antineutrino anomaly," Phys. Rev. D **83**, 073006.

Meroni, E., and S. Zavatarelli, 2016, "Borexino and geo-neutrinos: Unlocking the Earth's secrets," Nucl. Phys. News **26**, 21.

Mertsch, P., M. Rameez, and I. Tamborra, 2017, "Detection prospects for high energy neutrino sources from the anisotropic matter distribution in the local Universe," J. Cosmol. Astropart. Phys. 03, 011.

Mészáros, P., 2006, "Gamma-ray bursts, Rep. Prog. Phys. **69**, 2259.

Mészáros, P., 2013, "Gamma ray bursts," Astropart. Phys. **43**, 134.

Mészáros, P., 2017, "Gamma ray bursts as neutrino sources, in *Neutrino Astronomy*, edited by T. Gaisser and A. Karle (World Scientific, Singapore), pp. 1–14, https://doi.org/10.1142/9789814759410_0001.

Meyer, J.-P., L. O'C. Drury, and D. C. Ellison, 1997, "Galactic cosmic rays from supernova remnants. I. A cosmic ray composition controlled by volatility and mass-to-charge ratio," Astrophys. J. **487**, 182.

Meyer, M., M. Giannotti, A. Mirizzi, J. Conrad, and M. Sánchez-Conde, 2017, "Fermi Large Area Telescope as a Galactic Supernovae Axionscope," Phys. Rev. Lett. **118**, 011103.

Meyer, M., D. Horns, and M. Raue, 2013, "First lower limits on the photon-axion-like particle coupling from very high energy gamma-ray observations," Phys. Rev. D **87**, 035027.

Mirizzi, A., S. Pozzorini, G. G. Raffelt, and P. D. Serpico, 2009, "Flavour-dependent radiative correction to neutrino-neutrino refraction," J. High Energy Phys. 10, 020.

Mirizzi, A., I. Tamborra, H.-T. Janka, N. Saviano, K. Scholberg, R. Bollig, L. Hüdepohl, and S. Chakraborty, 2016, "Supernova neutrinos: Production, oscillations and detection," Riv. Nuovo Cimento Soc. Ital. Fis. **39**, 1.

Moharana, R., and S. Razzaque, 2015, "Angular correlation of cosmic neutrinos with ultrahigh-energy cosmic rays and implications for their sources," J. Cosmol. Astropart. Phys. 08, 014.

Møller, K., P. B. Denton, and I. Tamborra, 2019, "Cosmogenic neutrinos through the GRAND lens unveil the nature of cosmic accelerators," J. Cosmol. Astropart. Phys. 05, 047.

Møller, K., A. M. Suliga, I. Tamborra, and P. B. Denton, 2018, "Measuring the supernova unknowns at the next-generation neutrino telescopes through the diffuse neutrino background," J. Cosmol. Astropart. Phys. 05, 066.

Mondet, G., C. Blancard, P. Cossé, and G. Faussurier, 2015, "Opacity calculations for solar mixtures," Astrophys. J. Suppl. Ser. **220**, 2.

Mueller, T. A., *et al.*, 2011, "Improved predictions of reactor antineutrino spectra," Phys. Rev. C **83**, 054615.

Murase, K., 2017, "Active galactic nuclei as high-energy neutrino sources, in *Neutrino Astronomy*, edited by T. Gaisser and A. Karle (World Scientific, Singapore), pp. 15–31, https://doi.org/10.1142/9789814759410_0002.

Murase, K., M. Ahlers, and B. C. Lacki, 2013, "Testing the hadronuclear origin of PeV neutrinos observed with IceCube," Phys. Rev. D **88**, 121301.

Murase, K., J. F. Beacom, and H. Takami, 2012, "Gamma-ray and neutrino backgrounds as probes of the high-energy universe: Hints of cascades, general constraints, and implications for TeV searches," J. Cosmol. Astropart. Phys. 08, 030.

Murase, K., D. Guetta, and M. Ahlers, 2016, "Hidden Cosmic-Ray Accelerators as an Origin of TeV-PeV Cosmic Neutrinos," Phys. Rev. Lett. **116**, 071101.

Murase, K., Y. Inoue, and C. D. Dermer, 2014, "Diffuse neutrino intensity from the inner jets of active galactic nuclei: Impacts of external photon fields and the blazar sequence," Phys. Rev. D **90**, 023007.

Murase, K., and K. Ioka, 2013, "TeV-PeV Neutrinos from Low-Power Gamma-Ray Burst Jets inside Stars," Phys. Rev. Lett. **111**, 121102.

Murase, K., K. Ioka, S. Nagataki, and T. Nakamura, 2006, "High-energy neutrinos and cosmic rays from low-luminosity gamma-ray bursts?," Astrophys. J. **651**, L5.

Murase, K., K. Ioka, S. Nagataki, and T. Nakamura, 2008, "High-energy cosmic-ray nuclei from high- and low-luminosity gamma-ray bursts and implications for multi-messenger astronomy," Phys. Rev. D **78**, 023005.

Murase, K., R. Laha, S. Ando, and M. Ahlers, 2015, "Testing the Dark Matter Scenario for PeV Neutrinos Observed in IceCube," Phys. Rev. Lett. **115**, 071301.

Murase, K., and E. Waxman, 2016, "Constraining high-energy cosmic neutrino sources: Implications and prospects," Phys. Rev. D **94**, 103006.

Nakazato, K., E. Mochida, Y. Niino, and H. Suzuki, 2015, "Spectrum of the supernova relic neutrino background and metallicity evolution of galaxies," Astrophys. J. **804**, 75.

Nakazato, K., K. Sumiyoshi, H. Suzuki, T. Totani, H. Umeda, and S. Yamada, 2013, "Supernova neutrino light curves and spectra for various progenitor stars: From core collapse to proto-neutron star cooling," Astrophys. J. Suppl. Ser. **205**, 2.

Nakazato, K., K. Sumiyoshi, H. Suzuki, and S. Yamada, 2008, "Oscillation and future detection of failed supernova neutrinos from black-hole-forming collapse," Phys. Rev. D **78**, 083014; **79**, 069901(E) (2009).

Nakazato, K., and H. Suzuki, 2019, "Cooling timescale for proto-neutron stars and properties of nuclear matter: Effective mass and symmetry energy at high densities," Astrophys. J. **878**, 25.

Nakazato, K., and H. Suzuki, 2020, "A new approach to mass and radius of neutron stars with supernova neutrinos," Astrophys. J. **891**, 156.

Nardi, E., and J. I. Zuluaga, 2004, "Exploring the sub-eV neutrino mass range with supernova neutrinos," Phys. Rev. D **69**, 103002.

Ng, K. C. Y., J. F. Beacom, A. H. G. Peter, and C. Rott, 2017, "Solar atmospheric neutrinos: A new neutrino floor for dark matter searches," Phys. Rev. D **96**, 103006.

Nicolaidis, A., 1988, "Neutrinos for geophysics," Phys. Lett. B **200**, 553.

Nicolaidis, A., M. Jannane, and A. Tarantola, 1991, "Neutrino tomography of the Earth," J. Geophys. Res. **96**, 21811.

Nötzold, D., and G. Raffelt, 1988, "Neutrino dispersion at finite temperature and density," Nucl. Phys. **B307**, 924.

O'Connor, E., and C. D. Ott, 2011, "Black hole formation in failing core-collapse supernovae," Astrophys. J. **730**, 70.

Oertel, M., M. Hempel, T. Klähn, and S. Typel, 2017, "Equations of state for supernovae and compact stars," Rev. Mod. Phys. **89**, 015007.

Ohlsson, T., 2013, "Status of non-standard neutrino interactions," Rep. Prog. Phys. **76**, 044201.

Oldengott, I. M., and D. J. Schwarz, 2017, "Improved constraints on lepton asymmetry from the cosmic microwave background," Europhys. Lett. **119**, 29001.

Olinto, A. V., *et al.*, 2018, "POEMMA: Probe of Extreme Multi-Messenger Astrophysics," Proc. Sci. ICRC2017, 542 [arXiv:1708.07599].

Olive, K. A., *et al.* (Particle Data Group), 2014, "Review of particle physics," Chin. Phys. C **38**, 090001.

Opher, R., 1974, "Coherent scattering of cosmic neutrinos," Astron. Astrophys. **37**, 135, http://adsabs.harvard.edu/abs/1974A%26A....37..135O.

Orebi Gann, G. D. (THEIA Interest Group), 2015, "Physics potential of an advanced scintillation detector: Introducing THEIA," arXiv:1504.08284.

Padovani, P., M. Petropoulou, P. Giommi, and E. Resconi, 2015, "A simplified view of blazars: The neutrino background," Mon. Not. R. Astron. Soc. **452**, 1877.

Padovani, P., *et al.*, 2017, "Active galactic nuclei: What's in a name?," Astron. Astrophys. Rev. **25**, 2.

Pagliaroli, G., A. Palladino, F. Villante, and F. Vissani, 2015, "Testing nonradiative neutrino decay scenarios with IceCube data," Phys. Rev. D **92**, 113008.

Pagliaroli, G., F. Vissani, M. L. Costantini, and A. Ianni, 2009, "Improved analysis of SN1987A antineutrino events," Astropart. Phys. **31**, 163.

Pakvasa, S., A. Joshipura, and S. Mohanty, 2013, "Explanation for the Low Flux of High-Energy Astrophysical Muon Neutrinos," Phys. Rev. Lett. **110**, 171802.

Pakvasa, S., W. A. Simmons, and T. J. Weiler, 1989, "Test of equivalence principle for neutrinos and antineutrinos," Phys. Rev. D **39**, 1761.

Palladino, A., X. Rodrigues, S. Gao, and W. Winter, 2019, "Interpretation of the diffuse astrophysical neutrino flux in terms of the blazar sequence," Astrophys. J. **871**, 41.

Palme, H., and H. S. C. O'Neill, 2003, "Cosmochemical estimates of mantle composition," in *Treatise on Geochemistry*, Vol. 2, edited by R. W. Carlson (Elsevier, New York), p. 568, https://doi.org/10.1016/B0-08-043751-6/02177-0.

Pasquali, L., and M. Reno, 1999, "Tau-neutrino fluxes from atmospheric charm," Phys. Rev. D **59**, 093003.

Pastor, S., T. Pinto, and G. G. Raffelt, 2009, "Relic Density of Neutrinos with Primordial Asymmetries," Phys. Rev. Lett. **102**, 241302.

Pasyanos, M. E., T. G. Masters, G. Laske, and Z. Ma, 2014, "LITHO1.0: An updated crust and lithospheric model of the Earth," J. Geophys. Res. Solid Earth **119**, 2153.

Petropoulou, M., S. Dimitrakoudis, P. Padovani, A. Mastichiadis, and E. Resconi, 2015, "Photohadronic origin of γ-ray BL Lac emission: Implications for IceCube neutrinos," Mon. Not. R. Astron. Soc. **448**, 2412.

Piran, T., 1999, "Gamma-ray bursts and the fireball model," Phys. Rep. **314**, 575.

Priya, A., and C. Lunardini, 2017, "Diffuse neutrinos from luminous and dark supernovae: Prospects for upcoming detectors at the $\mathcal{O}(10)$ kt scale," J. Cosmol. Astropart. Phys. 11, 031.

Protheroe, R. J., 1997, "High-energy neutrinos from blazars," Astron. Soc. Pac. Conf. Ser. **121**, 585, http://adsabs.harvard.edu/abs/1997ASPC..121..585P.

Qian, X., and J.-C. Peng, 2019, "Physics with reactor neutrinos," Rep. Prog. Phys. **82**, 036201.

Raffelt, G., 1990, "New Bound on Neutrino Dipole Moments from Globular-Cluster Stars," Phys. Rev. Lett. **64**, 2856.

Raffelt, G., and L. Stodolsky, 1988, "Mixing of the photon with low-mass particles," Phys. Rev. D **37**, 1237.

Raffelt, G. G., 1996, *Stars as Laboratories for Fundamental Physics* (Chicago University Press, Chicago).

Raffelt, G. G., 2001, "Muon-neutrino and tau-neutrino spectra formation in supernovae," Astrophys. J. **561**, 890.

Razzaque, S., P. Mészáros, and E. Waxman, 2004, "TeV Neutrinos from Core Collapse Supernovae and Hypernovae," Phys. Rev. Lett. **93**, 181101; **94**, 109903(E) (2005).

Reines, F., M. F. Crouch, T. L. Jenkins, W. R. Kropp, H. S. Gurr, G. R. Smith, J. P. F. Sellschop, and B. Meyer, 1965, "Evidence for High-Energy Cosmic-Ray Neutrino Interactions," Phys. Rev. Lett. **15**, 429.

Renshaw, A., *et al.* (Super-Kamiokande Collaboration), 2014, "First Indication of Terrestrial Matter Effects on Solar Neutrino Oscillation," Phys. Rev. Lett. **112**, 091805.

Ressell, M. T., and M. S. Turner, 1990, "The grand unified photon spectrum: A coherent view of the diffuse extragalactic background radiation, Comments Astrophys. **14**, 323, https://ui.adsabs.harvard.edu/abs/1990ComAp..14..323R.

Richard, E., *et al.* (Super-Kamiokande Collaboration), 2016, "Measurements of the atmospheric neutrino flux by Super-Kamiokande: Energy spectra, geomagnetic effects, and solar modulation," Phys. Rev. D **94**, 052001.

Ringwald, A., 2009, "Prospects for the direct detection of the cosmic neutrino background," Nucl. Phys. **A827**, 501C.

Ringwald, A., and Y. Y. Y. Wong, 2004, "Gravitational clustering of relic neutrinos and implications for their detection," J. Cosmol. Astropart. Phys. 12, 005.

Ritz, S., and D. Seckel, 1988, "Detailed neutrino spectra from cold dark matter annihilations in the Sun," Nucl. Phys. **B304**, 877.

Robertson, B. E., R. S. Ellis, S. R. Furlanetto, and J. S. Dunlop, 2015, "Cosmic reionization and early star-forming galaxies: A joint analysis of new constraints from Planck and the Hubble Space Telescope," Astrophys. J. **802**, L19.

Rott, C., K. Kohri, and S. C. Park, 2015, "Superheavy dark matter and IceCube neutrino signals: Bounds on decaying dark matter," Phys. Rev. D **92**, 023529.

Salpeter, E. E., 1955, "The luminosity function and stellar evolution," Astrophys. J. **121**, 161.

Sawyer, R. F., 2016, "Neutrino Cloud Instabilities Just above the Neutrino Sphere of a Supernova," Phys. Rev. Lett. **116**, 081101.

Schechter, J., and J. Valle, 1982, "Neutrino decay and spontaneous violation of lepton number," Phys. Rev. D **25**, 774.

Schilbach, T. S. H., O. L. Caballero, and G. C. McLaughlin, 2019, "Black hole accretion disk diffuse neutrino background," Phys. Rev. D **100**, 043008.

Scholberg, K., 2012, "Supernova neutrino detection," Annu. Rev. Nucl. Part. Sci. **62**, 81.

Scholberg, K., 2018, "Supernova signatures of neutrino mass ordering," J. Phys. G **45**, 014002.

Scott, P., M. Asplund, N. Grevesse, M. Bergemann, and A. J. Sauval, 2015, "The elemental composition of the Sun II. The iron group elements Sc to Ni," Astron. Astrophys. **573**, A26.

Scott, P., N. Grevesse, M. Asplund, A. J. Sauval, K. Lind, Y. Takeda, R. Collet, R. Trampedach, and W. Hayek, 2015, "The elemental composition of the Sun. I. The intermediate mass elements Na to Ca," Astron. Astrophys. **573**, A25.

Seckel, D., T. Stanev, and T. K. Gaisser, 1991, "Signatures of cosmic-ray interactions on the solar surface," Astrophys. J. **382**, 652.

Senno, N., P. Mészáros, K. Murase, P. Baerwald, and M. J. Rees, 2015, "Extragalactic star-forming galaxies with hypernovae and supernovae as high-energy neutrino and gamma-ray sources: The case of the 10 TeV neutrino data," Astrophys. J. **806**, 24.

Senno, N., K. Murase, and P. Mészáros, 2016, "Choked jets and low-luminosity gamma-ray bursts as hidden neutrino sources," Phys. Rev. D **93**, 083003.

Serenelli, A., 2016, "Alive and well: A short review about standard solar models," Eur. Phys. J. A **52**, 78.

Shikhin, A. A., V. N. Gavrin, V. V. Gorbachev, T. V. Ibragimova, A. V. Kalikhov, and V. E. Yants, 2017, "Registration of ^{71}Ge rare decays in radiochemical gallium experiments SAGE and BEST," J. Phys. Conf. Ser. **798**, 012201.

Shimizu, I., 2017, "KamLAND: geo-neutrino measurement in Japan," Ann. Geophys. **60**, S0113.

Shoemaker, I. M., and K. Murase, 2018, "Constraints from the time lag between gravitational waves and gamma rays: Implications of GW170817 and GRB 170817A," Phys. Rev. D **97**, 083013.

Silk, J., K. A. Olive, and M. Srednicki, 1985, "The Photino, the Sun and High-Energy Neutrinos," Phys. Rev. Lett. **55**, 257.

Silvestri, A., and S. W. Barwick, 2010, "Constraints on extragalactic point source flux from diffuse neutrino limits," Phys. Rev. D **81**, 023001.

Smartt, S. J., J. J. Eldridge, R. M. Crockett, and J. R. Maund, 2009, "The death of massive stars—I. Observational constraints on the progenitors of type II-P supernovae," Mon. Not. R. Astron. Soc. **395**, 1409.

Smirnov, O., 2019, "Experimental aspects of geoneutrino detection: Status and perspectives," Prog. Part. Nucl. Phys. **109**, 103712.

Spiering, C., 2012, "Towards high-energy neutrino astronomy. A historical review, Eur. Phys. J. H **37**, 515.

Šrámek, O., B. Roskovec, S. Wipperfurth, Y. Xi, and W. McDonough, 2016, "Revealing the Earth's mantle from the tallest mountains using the Jinping Neutrino Experiment, Sci. Rep. **6**, 33034.

Srednicki, M., K. A. Olive, and J. Silk, 1987, "High-energy neutrinos from the Sun and cold dark matter," Nucl. Phys. **B279**, 804.

Stanev, T., 2004, *High Energy Cosmic Rays* (Springer, New York).

Steigman, G., 2007, "Primordial nucleosynthesis in the precision cosmology era," Annu. Rev. Nucl. Part. Sci. **57**, 463.

Stodolsky, L., 1975, "Speculations on Detection of the 'Neutrino Sea,' " Phys. Rev. Lett. **34**, 110.

Stodolsky, L., 1988, "The speed of light and the speed of neutrinos," Phys. Lett. B **201**, 353.

Stonehill, L. C., J. A. Formaggio, and R. G. H. Robertson, 2004, "Solar neutrinos from CNO electron capture," Phys. Rev. C **69**, 015801.

Strauss, R., M. Potgieter, I. Büsching, and A. Kopp, 2012, "Modelling heliospheric current sheet drift in stochastic cosmic ray transport models," Astrophys. Space Sci. **339**, 223–236.

Strolger, L.-G., T. Dahlen, S. A. Rodney, O. Graur, A. G. Riess, C. McCully, S. Ravindranath, B. Mobasher, and A. K. Shahady, 2015, "The rate of core collapse supernovae to redshift 2.5 from the CANDELS and CLASH supernova surveys," Astrophys. J. **813**, 93.

Sudoh, T., T. Totani, and N. Kawanaka, 2018, "High-energy gamma-ray and neutrino production in star-forming galaxies across cosmic time: Difficulties in explaining the IceCube data," Publ. Astron. Soc. Jpn. **70**, 49.

Sukhbold, T., T. Ertl, S. E. Woosley, J. M. Brown, and H.-T. Janka, 2016, "Core-collapse supernovae from 9 to 120 solar masses based on neutrino-powered explosions," Astrophys. J. **821**, 38.

Sumiyoshi, K., S. Yamada, H. Suzuki, and S. Chiba, 2006, "Neutrino Signals from the Formation of Black Hole: A Probe of Equation of State of Dense Matter," Phys. Rev. Lett. **97**, 091101.

Summa, A., H.-T. Janka, T. Melson, and A. Marek, 2018, "Rotation-supported neutrino-driven supernova explosions in three dimensions and the critical luminosity condition," Astrophys. J. **852**, 28.

Tamborra, I., and S. Ando, 2015, "Diffuse emission of high-energy neutrinos from gamma-ray burst fireballs," J. Cosmol. Astropart. Phys. 09, 036.

Tamborra, I., S. Ando, and K. Murase, 2014, "Star-forming galaxies as the origin of diffuse high-energy backgrounds: Gamma-ray and neutrino connections, and implications for starburst history," J. Cosmol. Astropart. Phys. 09, 043.

Tamborra, I., F. Hanke, H.-T. Janka, B. Müller, G. G. Raffelt, and A. Marek, 2014, "Self-sustained asymmetry of lepton-number emission: A new phenomenon during the supernova shock-accretion phase in three dimensions," Astrophys. J. **792**, 96.

Tamborra, I., F. Hanke, B. Müller, H.-T. Janka, and G. Raffelt, 2013, "Neutrino Signature of Supernova Hydrodynamical Instabilities in Three Dimensions," Phys. Rev. Lett. **111**, 121104.

Tamborra, I., B. Müller, L. Hüdepohl, H.-T. Janka, and G. Raffelt, 2012, "High-resolution supernova neutrino spectra represented by a simple fit," Phys. Rev. D **86**, 125031.

Tanabashi, M., *et al.* (Particle Data Group), 2018, "Review of particle physics," Phys. Rev. D **98**, 030001.

Thompson, T. A., E. Quataert, E. Waxman, and A. Loeb, 2006, "Assessing the starburst contribution to the gamma-ray and neutrino backgrounds," arXiv:astro-ph/0608699.

Totani, T., K. Sato, H. E. Dalhed, and J. R. Wilson, 1998, "Future detection of supernova neutrino burst and explosion mechanism," Astrophys. J. **496**, 216.

Usman, S. M., G. R. Jocher, S. T. Dye, W. F. McDonough, and J. G. Learned, 2015, "AGM2015: Antineutrino Global Map 2015," Sci. Rep. **5**, 13945; **5**, 15308(E) (2015). For a map with a corrected legend see https://neutrinos.fnal.gov/sources/geoneutrinos/.

Vartanyan, D., A. Burrows, D. Radice, A. M. Skinner, and J. Dolence, 2019, "A successful 3D core-collapse supernova explosion model," Mon. Not. R. Astron. Soc. **482**, 351.

Villante, F. L., 2015, "ecCNO solar neutrinos: A challenge for gigantic ultra-pure liquid scintillator detectors," Phys. Lett. B **742**, 279.

Vinyoles, N., A. M. Serenelli, F. L. Villante, S. Basu, J. Bergström, M. C. Gonzalez-Garcia, M. Maltoni, C. Peña-Garay, and N. Song, 2017, "A new generation of standard solar models," Astrophys. J. **835**, 202.

Vitagliano, E., J. Redondo, and G. Raffelt, 2017, "Solar neutrino flux at keV energies," J. Cosmol. Astropart. Phys. 12, 010.

Vogel, P., 2015, "How difficult it would be to detect cosmic neutrino background?," AIP Conf. Proc. **1666**, 140003.

Vogel, P., and J. F. Beacom, 1999, "Angular distribution of neutron inverse beta decay, $\bar{\nu}_e + p \to e^+ + n$," Phys. Rev. D **60**, 053003.

Vogel, P., and J. Engel, 1989, "Neutrino electromagnetic form factors," Phys. Rev. D **39**, 3378.

Volkova, L., 1980, "Energy spectra and angular distributions of atmospheric neutrinos," Yad. Fiz. **31**, 1510 [Sov. J. Nucl. Phys. **31**, 784 (1980)], https://inis.iaea.org/search/search.aspx?orig_q=RN:12583471.

Volkova, L. V., and G. T. Zatsepin, 1999, "Uncertainties in prompt atmospheric neutrino flux calculations," Phys. Lett. B **462**, 211.

Walk, L., I. Tamborra, H.-T. Janka, and A. Summa, 2020, "Neutrino emission characteristics of black hole formation in three-dimensional simulations of stellar collapse," Phys. Rev. D **101**, 123013.

Wang, J. Z., *et al.*, 2002, "Measurement of cosmic-ray hydrogen and helium and their isotopic composition with the BESS experiment," Astrophys. J. **564**, 244.

Wang, Z.-Y., R.-Y. Liu, and X.-Y. Wang, 2016, "Testing the Equivalence Principle and Lorentz Invariance with PeV Neutrinos from Blazar Flares," Phys. Rev. Lett. **116**, 151101.

Watanabe, H. (KamLAND Collaboration), 2016, in *Proceedings of the International Workshop: Neutrino Research and Thermal Evolution of the Earth, Tohoku University, Sendai, Japan, 2016*, https://www.tfc.tohoku.ac.jp/wp-content/uploads/2016/10/04_HirokoWatanabe_TFC2016.pdf.

Waxman, E., 2003, "Gamma-ray bursts: The underlying model," Lect. Notes Phys. **598**, 393.

Waxman, E., 2017, in *Neutrino Astronomy*, edited by T. Gaisser and A. Karle (World Scientific, Singapore), pp. 33–45, https://doi.org/10.1142/9789814759410_0003.

Waxman, E., and J. N. Bahcall, 1997, "High-Energy Neutrinos from Cosmological Gamma-Ray Burst Fireballs," Phys. Rev. Lett. **78**, 2292.

Waxman, E., and J. N. Bahcall, 1998, "High-energy neutrinos from astrophysical sources: An upper bound," Phys. Rev. D **59**, 023002.

Wei, J.-J., X.-L. Fan, B.-B. Zhang, X.-F. Wu, H. Gao, P. Mészáros, B. Zhang, Z.-G. Dai, S.-N. Zhang, and Z.-H. Zhu, 2017, "Multi-messenger tests of the weak equivalence principle from GW170817 and its electromagnetic counterparts," J. Cosmol. Astropart. Phys. 11, 035.

Wei, J.-J., and X.-F. Wu, 2018, "Robust limits on photon mass from statistical samples of extragalactic radio pulsars," J. Cosmol. Astropart. Phys. 07, 045.

Weiler, T. J., 1982, "Resonant Absorption of Cosmic-Ray Neutrinos by the Relic-Neutrino Background," Phys. Rev. Lett. **49**, 234.

Weinberg, S., 1962, "Universal neutrino degeneracy," Phys. Rev. **128**, 1457.

Winter, W. T., S. J. Freedman, K. E. Rehm, and J. P. Schiffer, 2006, "The ^{8}B neutrino spectrum," Phys. Rev. C **73**, 025503.

Wong, T.-W., C. L. Fryer, C. I. Ellinger, G. Rockefeller, and V. Kalogera, 2014, "The fallback mechanisms in core-collapse supernovae," arXiv:1401.3032.

Wurm, M., 2017, "Solar neutrino spectroscopy," Phys. Rep. **685**, 1.

Yoshimura, M., N. Sasao, and M. Tanaka, 2015, "Experimental method of detecting relic neutrino by atomic de-excitation," Phys. Rev. D **91**, 063516.

Yüksel, H., M. D. Kistler, J. F. Beacom, and A. M. Hopkins, 2008, "Revealing the high-redshift star formation rate with gamma-ray bursts," Astrophys. J. **683**, L5.

Yurchenko, V. Yu., and A. V. Ivanchik, 2019, "Non-equilibrium antineutrinos of primordial nucleosynthesis," arXiv: 1911.03473.

Zatsepin, G. T., and V. A. Kuz'min, 1966, "Upper limit of the spectrum of cosmic rays, JETP Lett. **4**, 78, https://ui.adsabs.harvard.edu/abs/1966JETPL...4...78Z.

Zhang, H., *et al.* (Super-Kamiokande Collaboration), 2015, "Supernova relic neutrino search with neutron tagging at Super-Kamiokande-IV," Astropart. Phys. **60**, 41.

See Supplemental Material at http://link.aps.org/supplemental/10.1103/RevModPhys.92.045006 for ancillary files, including tables and a *Mathematica* notebook to reproduce Fig. 1.